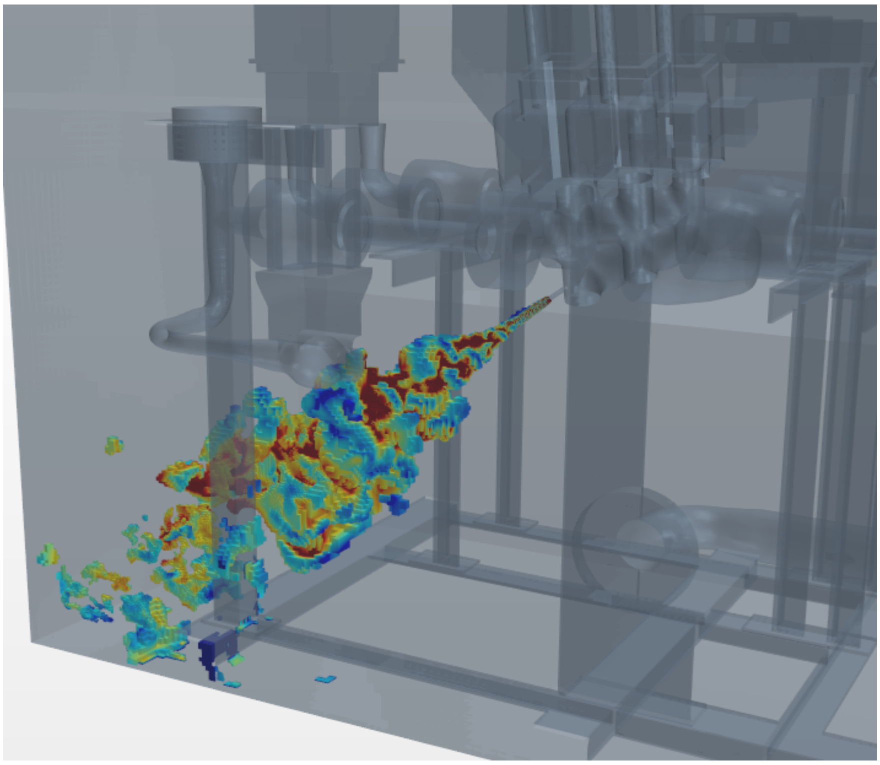

Numerical modelling of accidental gas release in a gas turbine enclosure

Evaluation of notional nozzle models and dispersion modelling using RANS, URANS and LES methods

Master's thesis

MARTIN FORSELL

Department of Mechanics and Maritime Sciences
CHALMERS UNIVERSITY OF TECHNOLOGY
Gothenburg, Sweden 2019

MASTER'S THESIS FOR MECHANICS AND MARITIME SCIENCES
2019:101

Numerical modelling of accidental gas release in a gas turbine enclosure

Evaluation of notional nozzle models and dispersion modelling using RANS, URANS and LES methods

MARTIN FORSELL

CHALMERS
UNIVERSITY OF TECHNOLOGY

Department of Mechanics and Maritime Sciences
Division of Fluid Dynamics
CHALMERS UNIVERSITY OF TECHNOLOGY
Gothenburg, Sweden 2019

Supervisors: Lars Davidson, Chalmers University of Technology, Department of Mechanics and Maritime Sciences, Division of Fluid Dynamics
Fredrik Carlsson, FS Dynamics
Stewart Whitworth, FS Dynamics
Examiner: Lars Davidson, Chalmers University of Technology, Department of Mechanics and Maritime Sciences, Division of Fluid Dynamics

Master's thesis 2019:101
Department of Mechanics and Maritime Sciences
Division of Fluid Dynamics
Chalmers University of Technology
SE-412 96 Gothenburg
Telephone +46 31 772 1000

Cover: The explosive gas cloud as a result from a leak, simulated with use of a notional nozzle model and LES. The colours show velocity magnitude from low (blue) to high(red).

Typeset in LaTeX
Gothenburg, Sweden 2019

Numerical modelling of accidental gas release in a gas turbine enclosure
Evaluation of notional nozzle models and dispersion modelling using RANS, URANS and LES methods
MARTIN FORSELL
Department of Mechanics and Maritime Sciences
Chalmers University of Technology

Abstract

In the event of an accidental gas leak in an industrial facility it is important that gas is not collected in a cloud of sufficiently large size and concentration that an explosion could occur. When evaluating the effect of an accidental gas release, the leak and the dispersion of potentially explosive gases must be modelled in a manner that is accurate and conservative.

The work presented in this report can be divided into two main parts. The first part concerns the modelling of the leak itself and what shape of the leak hole is appropriate to use. Jets exiting from circular, rectangular and elliptic orifices of different aspect ratios have been evaluated. Ways to model the hypersonic nearfield of the leak using notional nozzle submodels have been compared to a simulation of an equivalent hypersonic jet. Methane is used for modelling the leaked gas as it is the main constituent of natural gas.

The second part concerns ways to model the turbulent mixing of the leaked gas with ambient air. Two turbulence modelling approaches have been evaluated: URANS and LES. Steady RANS was found to not be a suitable approach for simulating the flow in the gas turbine enclosure even with no leak implemented.

Results indicate that the circular shape is the preferable choice regarding leak hole shape.The notional nozzle model called the Adiabatic expansion approach appears to be both conservative and highly accurate.

Simulations of the gas leak in a gas turbine enclosure using LES in combination with the Adiabatic expansion approach produces a considerably smaller explosive gas cloud volume compared to when URANS is used with the same notional nozzle model. This effect was not seen however when comparing URANS and LES when the Sonic jet approach was used as a notional nozzle. This could be due to the lower velocity of the jet produced with the Sonic jet approach which in turn might cause less turbulent mixing.

Keywords: URANS, LES, mixing, leak, notional nozzle, accidental gas release, fictional nozzle, submodel, methane jet

Acknowledgements

This project was completed during the time period March to October 2019 at the consulting company FS Dynamics. The participant in this thesis is a student of Master of Science in Engineering programs, from the master program Applied Mechanics at Chalmers University of Technology.

I will start by expressing my fullest gratitude towards supervisors Fredrik Carlsson, Lars Davidson and Stewart Whitworth where Lars Davidson also was the examiner of this thesis. I would also like to thank Ola Dahlin, manager at FS Dynamics, for allowing me to take on this project. I am grateful to all of them for their guidance and the constructive opinions and remarks I have received during the course of the project. Last but not least I would also like to thank the rest of the people at FS Dynamics for making me feel welcome during my stay there.

Contents

List of Figures

List of Tables

Abbrevations

- AR: Aspect ratio
- CFD: Computational fluid dynamics
- CFL: Courant-Friedrichs-Lewy condition
- GT: Gas turbine
- HSL: Health and safety laboratory
- LEL: Lower explosive limit
- LES: Large eddy simulation
- FVM: Finite volume method
- RANS: Reynolds-averaged Navier-Stokes
- URANS: Unsteady Reynolds-averaged Navier-Stokes
- SGS: sub grid stresses
- SST: Shear Stress Transport
- WALE: wall-adapting local-eddy viscosity

Nomenclature

Greek letters

χ	Void fraction	$[-]$
Δ	Grid filter width	$[m]$
δ	Boundary layer thickness	$[m]$
δ_{ij}	Kronckers delta	$[-]$
η	Pressure ratio	$[-]$
γ	Heat capacity ratio	$[-]$
κ	Von Karman constant	$[-]$
μ	Dynamic viscosity	$[kg/ms]$
μ_{SGS}	Subgrid scale viscosity	$[m^2/s]$
μ_t	Turbulent viscosity	$[kg/ms]$
ν	Kinematic viscosity	$[m^2/s]$
ν_t	Turbulent eddy viscosity	$[kg/ms]$
ω	Specific dissipation rate	$[1/s]$
ρ	Density	$[kg/m^3]$
σ	Stress	$[Pa]$
σ_k	$k-\varepsilon$ model coefficient	$[-]$
σ_t	Turbulent Schmidt number	$[-]$
σ_ω	$k-\omega$ model coefficient	$[-]$

σ_ε	$k-\varepsilon$ model coefficient	$[-]$
τ	Compressibility	$[1/Pa]$
τ_{ij}	Reynolds stresses	$[m^2/s^2]$
ξ	Shape factor	$[-]$

Index notations

0	Stagnation property
∞	Farfield property
amb	Ambient property
e	Exit property
eq	Equivalent property
i	Phase

Roman letters

$\mathbf{I}$	Identity tensor	$[-]$
$\mathbf{q}$	Heat flux	$[W/m^2]$
$\mathbf{v}$	Velocity	$[m/s]$
$\dot{m}$	Mass flow	$[kg/s]$
a	Speed of sound	$[m/s]$
A_J	Area of vena contracta	$[m^2]$
A_O	Orifice area	$[m^2]$
A_t	Throat area	$[m^2]$
C	Discharge coefficient	$[-]$
c	Characteristic wave speed of a system	$[m/s]$
C_μ	$k-\varepsilon$ coefficient	$[-]$
$C_{\varepsilon 1}$	$k-\varepsilon$ coefficient	$[-]$
$C_{\varepsilon 2}$	$k-\varepsilon$ coefficient	$[-]$

C_c	Coefficient of contraction	$[-]$
C_f	Coefficient of friction	$[-]$
C_w	WALE model coefficient	$[-]$
Co	Courant number	$[-]$
D_h	Hydraulic diameter	$[m]$
E	Energy per unit mass	$[J/kg]$
F_1	Blending function	$[-]$
f_2	ε-equation damping function	$[-]$
f_b	Resultant body forces	$[N]$
f_μ	$k-\varepsilon$ damping function	$[-]$
G	LES filter function	$[-]$
h	Convection coefficient	$[W/(m^2K)]$
j_m	Mass flux	$[kg/m^2]$
l	Characteristics diagonal equivalent	$[m]$
S_E	Energy source per unit volume	$[J/m^3]$
S_k	Source term in k-equation	$[kg/s^3m]$
S_ε	Source term in ε-equation	$[kg/s^4m]$
S_{Y_i}	Mass fraction source per unit volume	$[1/m^3]$
T	Turbulent time scale	$[s]$
t	Time	$[s]$
Y_i	Mass fraction of a species	$[-]$
$\mathbf{T_{RANS}}$	RANS stress tensor	$[m^2/s^2]$
$\mathbf{T_{SGS}}$	Sub grid stress tensor	$[m^2/s^2]$
$\mathbf{T}$	Viscous stress tensor	$[m^2/s^2]$
C_e	Nozzle exit perimeter	$[m]$

C_{lip}	Nozzle lip perimeter	$[m]$
C_{nc}	Noncircular nozzle lip perimeter	$[m]$
g	Gravitational constant	$[m/s^2]$
J_i	Laminar diffusion	$[m^2/s]$
k_{RES}	Resolved turbulent kinetic energy	$[m^2/s^2]$
k_{SGS}	Modelled turbulent kinetic energy	$[m^2/s^2]$
k	Turbulent kinetic energy	$[m^2/s^2]$
L_c	Jet core length	$[m]$
M	Mach number	$[-]$
P_k	k-equation production term	$[kg/s^3m]$
P_ε	ε-equation production term	$[kg/s^4m]$
p	Pressure	$[Pa]$
S_{ij}	Mean strain rate tensor	$[1/s]$
S_w	WALE deformation parameter	$[-]$
u_τ	Friction velocity	$[m/s]$
v_g	Relative velocity	$[m/s]$

1
Introduction

1.1 Background

Combustible gas leakages have long been a concern in the oil and gas industry and is suspected to be the cause of disastrous accidents. One example is the Piper Alpha oil rig disaster in 1988. An investigation showed that the probable cause for the disaster was a gas leak from a blind flange and that the resulting gas cloud shortly thereafter exploded which led to collapse of the rig [1]. In addition to the loss of 167 human lives, it also caused financial losses in the order of £2 million.

Gas leaks are in general hard to predict and model. There are many factors to consider including leak location, orientation and which shape of the orifice is most appropriate to use. It is therefore of interest to know the impact of different modelling approaches of the leak.

Zaman[2] experimentally investigated the characteristics of both subsonic and supersonic jets of different orifice shapes. It was found that spreading of the jet in supersonic cases was to some degree higher for the asymmetric shapes compared to the circular shape. Orifice aspect ratio seemed to have a small effect on jet behaviour. It was only for orifices of an aspect ratio above 16 and higher an effect was started to become noticeable, giving the jet higher mass flow rate and spread. The increase of spread was in large part due to the jet entraining more air and thus it also increased its mass flow as air surrounding the jet became part of the jet.

It was also found was that the spreading of the jet decreased with increased Mach number and that the jet tended to become round downstream of the jet even for asymmetrically shaped orifices.

In a work by Shishehgaran et. al [3], the effect of an underexpanded hydrogen jet escaping from a circular versus an elliptical orifice was investigated and while the aspect ratio was limited up to only AR = 6, it was found that area size of the exit orifice impacts the dispersion and development of the hydrogen jet more than the effect of the orifice shape. The authors of the paper concluded that for the risk of auto-ignition, the circular shaped hole was the most conservative geometry.

Makarov and Molkov [4] investigated the difference in jet characteristics between a round jet, and plane nozzles with AR 5 and 12.8. It was found that the jets from the plane nozzles had higher velocity decay as well as a higher concentration decay rate due to more mixing with air compared to an equivalent axisymmetric jet.

The large pressure ratio existing in the fuel system in a gas turbine (GT) enclosure makes it prohibitively costly to resolve the entire leak. This is due to the leak usually being hypersonic and consisting of a complex shock pattern in the near-field of the jet. To get around this issue, a submodel for part of the leak is commonly used. This submodel is known as a notional nozzle, fictional nozzle or equivalent nozzle and several variants of these models exist.

To the knowledge of the author of this paper, no investigation has been done concerning what leak shape and submodel is appropriate to use with respect to the size of the resulting explosive gas cloud. The appropriate choice should result in a gas cloud that is both conservative and close in accuracy regarding size to if the equivalent leak is simulated without a submodel.

The ability to accurately predict the dispersion and mixing of the leaked gas away from the leak hole is also important. If the monitoring system is overly sensitive, unnecessary downtime and financial losses may be the result. On the other hand, if the monitoring system is not sensitive enough, risks exist for both workers and equipment.

Reynolds Averaged Navier-Stokes (RANS) methods for modelling the turbulence are thought to cause considerable under-predicting of the mixing of the gas leak with the ambient ventilation air. For this reason, it is of interest to investigate the performance when using Large Eddy Simulation (LES). This method resolves large-scale turbulence and could potentially predict the mixing more accurately.

1.2 Aim

Part of the aim of this thesis is to verify and develop existing gas leakage boundary conditions.

Additionally, the aim is to predict the size and distribution of the gas cloud due to leakage as it mixes with the ambient air for a simplified geometry of a GT-enclosure.

These aims will be reached with help of numerical simulations using the software STAR-CCM+.

In all fluid simulations, there exists approximations. These can range from discretization errors to modelling errors when attempting to capture turbulence effects. When evaluating the risk for explosion, the chosen method needs to be accurate to minimize unwarranted downtime but still conservative enough to compensate for possible approximations and simplifications. The leak considered should represent a worst case scenario and should thus be placed in a location that represents this.

Results based on the RANS model will be compared to the results from a LES for a leak implemented in a GT-enclosure.

1.3 Limitations

The explosion itself will not be simulated, nor any type of combustion/fire simulation.

No experimental work will be done.

Aeroacustic effects are not considered.

In accordance with studies conducted by the Health & Safety Laboratory (HSL)[5], leak hole size considered will not be larger than 25 mm^2 or smaller than 0.25 mm^2.

The effect of radiation will be neglected.

2

Theory

2.1 Governing equations

The governing equations for a compressible Newtonian fluid can be written as follows[6], starting with continuity:

$$\frac{\partial \rho}{\partial t} + \nabla \cdot (\rho \mathbf{v}) = 0 \tag{2.1}$$

where ρ is density and $\mathbf{v}$ is velocity.

For momentum:

$$\frac{\partial (\rho \mathbf{v})}{\partial t} + \nabla(\rho \mathbf{v} \otimes \mathbf{v}) = -\nabla \cdot (p\mathbf{I}) + \nabla \cdot \mathbf{T} + \mathbf{f}_b \tag{2.2}$$

where $\otimes$ denotes outer product, $\mathbf{f}_b$ is resultant body forces, $\mathbf{I}$ is the identity tensor, p is pressure and $\mathbf{T}$ is the viscous stress tensor.

The energy equation can be written as:

$$\frac{\partial (\rho E)}{\partial t} + \nabla \cdot \Big(\rho E \mathbf{v}\Big) = \mathbf{f}_b \cdot \mathbf{v} + \nabla \cdot (\mathbf{v} \cdot \sigma) - \nabla \mathbf{q} + S_E \tag{2.3}$$

where E is total energy per unit mass, $\mathbf{q}$ is the heat flux, and S_E is an energy source per unit volume. A transport equation for each mass fraction of a species Y_i can be written as:

$$\frac{\partial}{\partial t}\left(\int_V \rho Y_i\right) d\tilde{V} + \oint_A \rho Y_i(\mathbf{v} - v_g) \cdot d\tilde{\mathbf{a}} = \oint_A \left[J_i + \frac{\mu_t}{\sigma_t}\Delta Y_i\right] \cdot d\tilde{\mathbf{a}} + \int_V S_{Y_i} dV \tag{2.4}$$

where $\frac{\mu_t}{\sigma_t}$ represents turbulent diffusion, σ_t is the turbulent Schmidt number, v_g relative velocity, S_{Y_i} denotes a source quantity, μ_t is the turbulent viscosity and J_i laminar diffusion. Furthermore $d\tilde{V} = a_i \chi dV$ with a_i is volume fraction of phase i, χ the void fraction and $d\tilde{\mathbf{a}} = a_i \chi d\mathbf{a}$.

2.2 Reynolds-averaged Navier-Stokes

When using the RANS approach to simulate fluid flow, the instantaneous quantities (e.g. velocity $\mathbf{v}$) are decomposed into a mean and fluctuating component as $\mathbf{v} = \overline{\mathbf{v}} + \mathbf{v'}$.

Inserting this in the governing equations for instantaneous quantities and then time-averaging, the result is the Reynolds-averaged equations.

The mean transport equations for continuity and momentum respectively can be written as

$$\frac{\partial \rho}{\partial t} + \nabla \cdot (\rho \overline{\mathbf{v}}) = 0 \tag{2.5}$$

and

$$\frac{\partial}{\partial t}\Big(\rho \overline{\mathbf{v}}\Big) + \nabla \cdot (\rho \overline{\mathbf{v}} \otimes \overline{\mathbf{v}}) = -\nabla \cdot \overline{p}\mathbf{I} + \nabla \cdot (\mathbf{T} + \mathbf{T}_{RANS}) + \mathbf{f}_b \tag{2.6}$$

where $\overline{\mathbf{v}}$ and $\overline{p}$ are the time-averaged velocity and pressure respectively. The new stress tensor $\mathbf{T_{RANS}}$ has the following definition

$$\mathbf{T_{RANS}} = -\rho \begin{pmatrix} \overline{u'u'} & \overline{u'v'} & \overline{u'w'} \\ \overline{u'v'} & \overline{v'v'} & \overline{v'w'} \\ \overline{u'w'} & \overline{v'w'} & \overline{w'w'} \end{pmatrix} + \frac{2}{3}\rho k \mathbf{I} \tag{2.7}$$

where k is the turbulent kinetic energy. The mean products of fluctuating velocities in $\mathbf{T_{RANS}}$ are unknown and thus this term needs to be modelled.

2.3 Large eddy simulation

An alternative to RANS for simulating turbulence is LES.

In RANS simulations, all scales of turbulence are modelled and this is known to give poor results in some situations. This is in large part because the behaviour for small scale and large scale eddies is different. Small scale eddies are nearly isotropic while large scale eddies have anisotropic behaviour and this is hard to capture with a single turbulence model [7].

LES attempts to solve the issue of varying eddy size behaviour by only modelling the small supposedly isotropic eddies and to in contrast to RANS, resolve the larger eddies. Spatial averaging is used to separate the larger and smaller eddies.

Using LES, one first selects a filtering function and a cutoff width for which the purpose is to resolve all eddies greater than the cutoff width. The cut off width should ideally be located in the inertial subrange [8]. The interaction between the larger and smaller eddies give rise to sub-grid-scale (SGS) stresses. To capture this effect between the small unresolved eddies and the larger resolved eddies, a SGS model can be used.

In LES, a filtering operation is defined using a filtering function $G(x, x', \Delta)$, where Δ is the filter cut-off width.

A flow variable $\phi(x,t)$ is decomposed into a filtered/resolved part $\widetilde{\phi}(x,t)$, and a unresolved (smaller than cutoff width) $\phi'(x,t)$ in the following way:

$$\phi(x,t) = \widetilde{\phi}(x,t) + \phi'(x,t). \tag{2.8}$$

The filtering operation is defined as

$$\widetilde{\phi}(x,t) \equiv \int_{-\infty}^{\infty}\int_{-\infty}^{\infty}\int_{-\infty}^{\infty} G(x,x',\Delta)\phi(x',t)dx_1'dx_2'dx_3' \tag{2.9}$$

where $\widetilde{\phi}(x,t)$ = filtered function and $\phi(x,t)$ = original (unfiltered) function.

The filter function commonly used is:

$$G(x,x',\Delta) = \begin{cases} 1/\Delta^3 \text{ if } |x-x'| \leq \Delta/2 \\ 0 \text{ if } |x-x'| > \Delta/2 \end{cases} \tag{2.10}$$

A common choice for Δ is $\Delta = \sqrt[3]{\Delta x \Delta y \Delta z}$

Inserting the decomposed variables, the filtered equations for mass and momentum becomes [6]:

$$\frac{\partial \rho}{\partial t} + \nabla \cdot (\rho \widetilde{\mathbf{v}}) = 0 \tag{2.11}$$

and

$$\frac{\partial}{\partial t}\Big(\rho\widetilde{\mathbf{v}}\Big) + \nabla \cdot (\rho \widetilde{\mathbf{v}} \otimes \widetilde{\mathbf{v}}) = -\nabla \widetilde{p}\mathbf{I} + \nabla \cdot (\mathbf{T} + \mathbf{T_{SGS}}) + \mathbf{f_b} \tag{2.12}$$

where:

- $\widetilde{\mathbf{v}}$ and $\widetilde{p}$ are filtered velocity and pressure respectively.
- $\mathbf{T_{SGS}}$ represents the SGS stresses.

The stresses in LES can be divided into three groups:

- Leonard stresses: These are due to the fact that a second filtering operation changes the filtered variable, that is $\widetilde{\widetilde{\phi}} \neq \widetilde{\phi}$.
- Cross-stresses: These are from interaction between resolved (large-scale) and modelled (small-scale) flow.

- LES Reynolds stresses: From SGS stresses which must be modelled just as Reynolds stresses must be modelled with a turbulence model in RANS-based simulations.

2.4 Turbulence modelling

The unknown stress tensors in equation (2.7) for RANS and (2.12) for LES cause the need for turbulence modelling so that the equations can be closed. One way to model $\mathbf{T_{RANS}}$ and $\mathbf{T_{SGS}}$ is by use of a eddy-viscosity model, which uses the concept of a turbulent viscosity. One commonly used model is the Boussinesq approximation.

For RANS:

$$\mathbf{T_{RANS}} = 2\mu_t\mathbf{S} - \frac{2}{3}(\mu_t\nabla\cdot\overline{\mathbf{v}})\mathbf{I} \tag{2.13}$$

where $\mathbf{S}$ is the mean strain rate tensor. One advantage with this model is that only mean quantities are needed. Different models exist to derive μ_t, for example Realizible $k-\varepsilon$ and k-$\omega - SST$.

For LES $\mathbf{T_{SGS}}$ in equation (2.12) can similarly be modelled as

$$\mathbf{T_{SGS}} = 2\mu_{SGS}\mathbf{S} - \frac{2}{3}(\mu_{SGS}\nabla\cdot\tilde{\mathbf{v}})\mathbf{I} \tag{2.14}$$

where μ_{SGS} can be described by a sub grid scale model.

2.4.1 Realizeble $k-\varepsilon$

The $k-\varepsilon$ model aims to solve transport equations for turbulent kinetic energy, k, and the turbulent dissipation rate, ε, in order to calculate μ_t.

The turbulent viscosity μ_t is calculated as

$$\mu_t = \rho C_\mu f_\mu kT \tag{2.15}$$

where C_μ is a model coefficient, f_μ is a damping function and T is the turbulent time scale.

The transport equation for k is

$$\frac{\partial\rho k}{\partial t} + \nabla\cdot(\rho k\overline{\mathbf{v}}) = \left[\left(\mu + \frac{\mu_t}{\sigma_k}\right)\nabla k\right] + P_k - \rho(\varepsilon - \varepsilon_0) + S_k \tag{2.16}$$

and the transport equation for ε is

$$\frac{\partial\rho\varepsilon}{\partial t} + \nabla\cdot(\rho\varepsilon\overline{\mathbf{v}}) = \left[\left(\mu + \frac{\mu_t}{\sigma_\varepsilon}\right)\nabla\varepsilon\right] + \frac{1}{T_e}C_{\varepsilon 1}P_\varepsilon - C_{\varepsilon 2}f_2\rho\left(\frac{\varepsilon}{T_e} - \frac{\varepsilon_0}{T_0}\right) + S_\varepsilon \tag{2.17}$$

where:

- μ is dynamic viscosity.
- σ_k, σ_ε, $C_{\varepsilon 1}$, and $C_{\varepsilon 2}$ are model coefficients.
- P_k and P_ε are production terms.
- f_2 is a damping function.
- S_k and S_ε are source terms.
- ε_0 is a ambient turbulence value.
- T_0 is a a specific time scale.

The Realizeble $k - \varepsilon$ model is a modified version of the standard $k - \varepsilon$ where constraints on the normal stresses have been implemented to make the it more physically consistent, this model is "substantially better than the Standard K-Epsilon model for many applications, and can generally be relied upon to give answers that are at least as accurate." [6].

2.4.2 $k - \omega$-SST

The model was first proposed by F.R. Menter in 1994 [6]. This approach effectively combines two turbulence models, using the $k - \varepsilon$ model in the far-field with a $k - \omega$ model near the wall. This is done by using a blending function F_1 that takes the value of one in the near-wall region and zero in the outer region.

The turbulent viscosity μ_t is calculated as

$$\mu_t = \rho k T \tag{2.18}$$

where ρ is density and T is a turbulent time scale.

Two transportation equations are used, for turbulent kinetic energy k and the rate of dissipation of the eddies ω respectively.

These can be written as [8]

$$\frac{\partial k}{\partial t} + \frac{\partial \overline{u}_j k}{\partial x_j} = \frac{\partial}{\partial x_j}\left[\left(\nu + \frac{\nu_t}{\sigma_k}\right)\frac{\partial k}{\partial x_j}\right] + P^k - \beta * k\omega \tag{2.19}$$

and

$$\frac{\partial \omega}{\partial t} + \frac{\partial \overline{u}_j \omega}{\partial x_j} = \frac{\partial}{\partial x_j}\left[\left(\nu + \frac{\nu_t}{\sigma_\omega}\right)\frac{\partial \omega}{\partial x_j}\right] + \alpha\frac{P^k}{\nu_t} - \beta\omega^2 + 2(1 - F_1)\sigma_{\omega^2}\frac{1}{\omega}\frac{\partial k}{\partial x_i}\frac{\partial \omega}{\partial x_i} \tag{2.20}$$

where:

- $\overline{\mathbf{v}}$ is the mean velocity.
- μ is dynamic viscosity.
- F_1 is a blending function
- σ_k, σ_ω, $C_{\varepsilon 1}$, and $C_{\varepsilon 2}$ are model coefficients.
- P_k and P_ω are production terms.
- f_{β^*} is a free-shear modification factor.
- f_β is the vortex-stretching modification factor.
- S_k and S_ω are source terms.
- k_0 and ω_0 are the ambient turbulence values that counteract turbulence decay.

2.4.3 WALE

To model the SGS stresses, there exists a selection of models and this section will discuss the one used in this work, namely WALE. The WALE model has been shown to be less sensitive to the choice of model coefficient, C_w , compared to other commonly used SGS models as well as being computationally less expensive and more thoroughly validated [6]. It also does not require near-wall damping since it automatically gives accurate scaling at walls [22].

In WALE, the SGS viscosity is modeled as

$$\mu_{SGS} = \rho \Delta^2 S_w \tag{2.21}$$

where S_w is a deformation parameter.

Length scale Δ is determined using cell volume V as

$$\Delta = \begin{cases} C_w V^{1/3} \text{if length scale limit is not applied} \\ min(\kappa d, C_w V^{1/3}) \text{if length scale limit is applied} \end{cases} \tag{2.22}$$

where C_w is the model coefficient and κ is the Von Karman constant.

Deformation parameter S_w is defined as

$$S_w = \frac{\mathbf{S_d} : \mathbf{S_d}^{3/2}}{\mathbf{S_d} : \mathbf{S_d}^{5/4} + \mathbf{S} : \mathbf{S}^{5/2}} \tag{2.23}$$

$\mathbf{S_d}$ is defined as

$$\mathbf{S_d} = \frac{1}{2}[\nabla \mathbf{v} \cdot \nabla \mathbf{v} + (\nabla \mathbf{v} \cdot \nabla \mathbf{v})^T] - \frac{1}{3} tr(\nabla \mathbf{v} \cdot \nabla \mathbf{v})\mathbf{I} \tag{2.24}$$

where $\mathbf{I}$ is the identity tensor.

2.5 Time dependency

Some problems present situations where the mean flow is unsteady. This could be due to phenomenons such as vortex shedding. Turbulent flow is inherently unsteady so methods where all or part of the turbulence is resolved needs to be time dependent. In the case of LES, large scale turbulence is resolved.

One way to choose time step is to use a restriction on the Courant number, Co, defined for the one dimensional case as [23]

$$Co = \frac{c\Delta t}{\Delta x} \tag{2.25}$$

where c is the characteristic wave speed of the system, Δt is the time step and Δx is the cell grid length in the numerical model.

This balances the transport of diffusive and convective transport through cells. For an explicit solver, it is a strict condition that $Co < 1$ so that the time step is less than the time it takes for flow properties to be transported from cell to cell.

The time step can be chosen from [9]

$$\Delta t < Co \times min\left(\frac{\rho(\Delta x)^2}{\Gamma}, \frac{\Delta x}{U}\right) \tag{2.26}$$

where Δx is cell length, U is velocity in x-direction, ρ is density and Γ is a transport coefficient, e.g. diffusivity, heat conductivity or viscosity. Furthermore, $Co = 1$ for an explicit solver while Co can be higher for a fully implicit solver. Implicit solvers are unconditionally stable with regard to time step size, this makes them suitable for industrial problems such as the one considered in this thesis. For obtaining accurate results Co should still be kept as low as is feasible.

The Euler implicit scheme is used as a first order scheme in STAR-CCM+ [6] for transient simulations. Using the solution at current time level $n + 1$ and from the previous level n

$$\frac{d}{dt}(\rho\phi v) = \frac{(\rho\phi v)^{n+1} - (\rho\phi v)^n}{\Delta t} \tag{2.27}$$

For second order schemes the Backward Differentiation Formula can be used. The most basic form (BDF2) uses solution the from the current time level but also the two previous time levels.

$$\frac{d}{dt}(\rho\phi v) = \left(\frac{3}{2}(\rho\phi v)^{n+1} - 2(\rho\phi v)^n + \frac{1}{2}(\rho\phi v)^{n-1}\right)\frac{1}{\Delta t} \tag{2.28}$$

It can be further modified to use more time levels.

2.6 Heat transfer

There exists three main modes, or physical processes, through which heat can be transferred [10]. These are conduction, i.e. when heat is transferred across a medium, convection when heat is transferred with a moving fluid and radiation which is when heat is transferred in the form of electromagnetic waves. As a radiation model is not implemented in this work, this section covers conduction and convection.

2.6.1 Conduction

Conduction can be seen as a diffusion of energy where more energetic molecules, having a higher temperature, interact with less energetic molecules, having a lower temperature. A mathematical model for this process is Fourier's law:

$$q = -k\nabla T \tag{2.29}$$

Here k is the heat conduction coefficient.

2.6.2 Convection

For thermal energy transfer between a surface and a moving fluid, Fouriers law is used for the surface heat flux q_s

$$q_s = -k_f \frac{\partial T}{\partial y}\bigg|_{y=0} \tag{2.30}$$

where k_f is the heat conduction coefficient of the fluid. Newton's law for cooling is

$$q_s = h(T_s - T_\infty) \tag{2.31}$$

where h is the convection coefficient. Combining eq. (2.30) and eq. (2.31) yields

$$h = \frac{-k_f \frac{\partial T}{\partial y}\big|_{y=0}}{T_s - T_\infty} \tag{2.32}$$

2.7 Compressible flow

All fluids are to some extent compressible but the magnitude of compressibility varies greatly between different types of fluids. Liquids for example have a very low compressibility. Compressibility, denoted τ can be defined as [11]

$$\tau = \frac{1}{\rho}\frac{d\rho}{dp}. \tag{2.33}$$

The Mach number M is a dimensionless number that can have different values for each position in a flow field. It is defined as the fluid velocity V divided by the speed of sound a:

$$M = \frac{V}{a} \tag{2.34}$$

A flow is generally considered compressible if $M > 0.3$. An explanation of the speed of sound is how fast a sound wave will propagate in a gas.

The general expression for a is

$$a = \sqrt{\frac{\gamma p}{\rho}} \tag{2.35}$$

where $\gamma = c_p/c_v$.

For a perfect gas, a can be written as

$$a = \sqrt{\gamma RT}. \tag{2.36}$$

2.8 Orifice flow

Orifice flow is similar to flow through a converging-diverging nozzle but with more losses since part of the flow will separate directly after the orifice exit and the minimum area of the jet (also known as the vena contracta) and of the orifice (the throat) is not necessarily the same [12]. As shown in Figure 2.1 the vena contracta can exist downstream of the orifice exit.

The flow becomes choked as the vena contracta moves towards and comes in contact with the orifice edge upstream when the pressure difference is large enough.

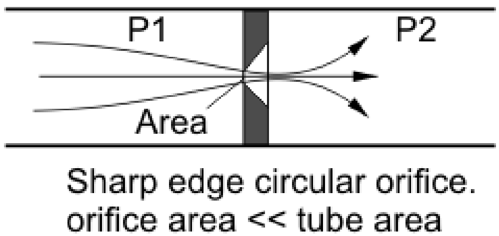

Figure 2.1: *Hydraulic orifice. (2015, January 20). Wikimedia Commons, the free media repository.*

A coefficient of contraction, C_c, is used which is defined as the ratio between the areas of the stream at the vena contracta A_J to the area of the orifice A_O:

$$C_c = \frac{A_J}{A_O} \tag{2.37}$$

A discharge coefficient C is used to compensate for pressure and friction losses through the orifice.

One definition [14] of the discharge coefficient is the product of a friction coefficient, C_f, and the contraction coefficient as

$$C = C_f \times C_c \tag{2.38}$$

though in many cases contraction plays the major part and friction is negligible. If the flow through the orifice is choked, the massflow can be calculated as [13]

$$\dot{m} = CA_t \left[\gamma \left(\frac{2}{\gamma + 1} \right)^{\frac{\gamma+1}{\gamma-1}} \right]^{1/2} \sqrt{(P_0 \rho_0)} \tag{2.39}$$

where A_t is the throat area, P_0 the total pressure and ρ_0 the total density.

A derivation of (2.39) is given in the appendix.

2.9 Jet characteristics

In general free, under-expanded compressible jets are characterized by three regions [15]:

- Nearfield region: This region can be divided into two parts: the core part and the mixing layer. Most relevant parameter for this region is the pressure ratio but jet exit Mach number and jet divergence angle also has an influence. The high pressure ratio for the leak jet studied in this work will cause the jet to be classified as extremely under-expanded. An extremely under-expanded jet has the structure of a single barrel cell ending in a curved Mach disk. The core part is dominated by compressible effects. Isentropic expansion and re-compression through shocks occur. Flow is close to steady.

  The mixing layer is the layers between the jet and surrounding fluid. It is largely turbulent with vortex forming downstream of the flow.

  A sketch of the structure of an extremely underexpanded jet in the nearfield zone is seen in Figure 2.2.

- Transition region: variables vary less to the surrounding fluid, this permits more mixing and pressure is gets equalized between the jet and surrounding fluid.

- Farfield region: flow tends to become similar to that of an axisymmetric jet. To get to this region it has been found that major axis width decrease and minor axis increase until they switch. The jet gets perfectly expanded. It behaves as a classical jet, i.e. ideally expended, and how it got to this state does not matter, meaning a perfect description of the nearfield behaviour is not necessary. The jet has taken on a Gaussian profile.

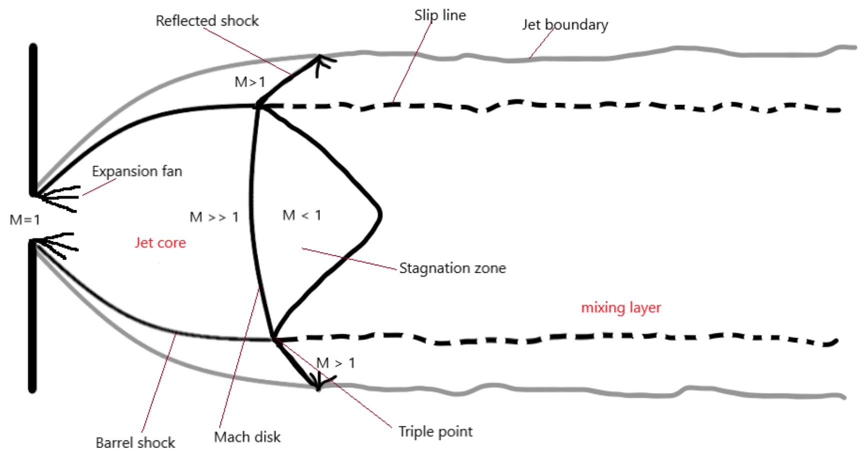

Figure 2.2: *Sketch of the nearfield of an extremely underexpanded jet.*

2.9.1 Jet core length

An empirical equation to calculate the supersonic core length of a jet that takes into consideration orifice shape and is valid for circular, rectangular and elliptic shapes was created by Mohanta[16]. This equation has been shown to give results similar to both experimental and numerical data.

$$L_c = \sqrt{\frac{P_{oi}}{P_a}}(D_h - d/2) \times 2l\frac{C_{nc}}{C_{lip}}\frac{1}{\xi} \tag{2.40}$$

- $\frac{P_{oi}}{P_a}$ is the pressure ratio of nozzle inlet pressure to ambient pressure.
- C_{lip} is the nozzle lip perimeter.
- C_e is the nozzle exit perimeter.
- C_{nc}Noncircular nozzle exit perimeter.
- d is the characteristics diagonal.
- D_h is the hydraulic diameter.
- ξ is a shape factor, $\xi = \frac{C_e}{C_{nc}}$.

- l is the characteristics diagonal equivalent.

Equation (2.40) could be useful when choosing where to place a boundary condition for the leakage in cases where a notional nozzle is used.

3

Gas leak modelling

Before modelling the gas leak in the GT-enclosure, it is important to know that the gas leak is modelled in a way that is conservative and approximates a real leak to a satisfying degree. One important factor is that the size of the explosive gas cloud is conservative and similar to that of a real jet.

A fuel-air mixture must be above the Lower Explosive Limit (LEL) for there to be a possibility for ignition[17]. The % LEL can be defined as:

$$\%\text{LEL} = \frac{\text{Gas Concentration (in \% vol)}}{\text{Lower Explosive Limit (in \% vol)}} \times 100 \tag{3.1}$$

and the Lower Explosive Limit is 5.0% vol for Methane which is the gas used to model the leak. Another measurement is the equivalent gas volume which is a quantity that takes into account how much air one unit of fuel needs to have a stoichiometric air-to-fuel ratio.

$$CH_4 + 2(O_2 + 3.76N_2) \rightarrow CO_2 + 2H_2O + 7.52N_2 \tag{3.2}$$

One unit methane requires 2(1+3.76)=9.52 units of air.

3.1 Influence of orifice shape

One potentially important parameter for the modelling the leak is the shape of the hole. To better understand the influence of shape of the leak hole concerning size of the explosive gas cloud, jets exiting from orifices of different shapes are simulated. The chosen shapes are circular, elliptic and rectangular. For the elliptic and rectangular orifices three different aspect ratios were studied: 5, 10 and 15. All shapes were of equal area. To avoid simulating the supersonic part of the flow, the submodel called the Sonic jet approach was used. The jet was simulated with a co-flow meant to model ventilation air. This is how a worst case scenario should be modelled according to HSL [18].

The cylindrical mesh shown in Figure 3.2 was used. The number of cells were increased until no noticeable change in explosive gas cloud volume and no unrealistically large changes in gradients of quantities such as velocity and temperature could be seen from cell to cell. Since the Sonic jet model is constructed to produce a jet of $M = 1$, the centerline Mach number was monitored, see Figure 3.1. The number of cells in the final mesh used was around 3 million. The mesh was constructed by implementing refinement zones so the smallest cell size was by the jet inlet and gradually increased. The mesh study was done for the round jet and then a similar mesh was used for the simulations of jets from asymmetric orifices.

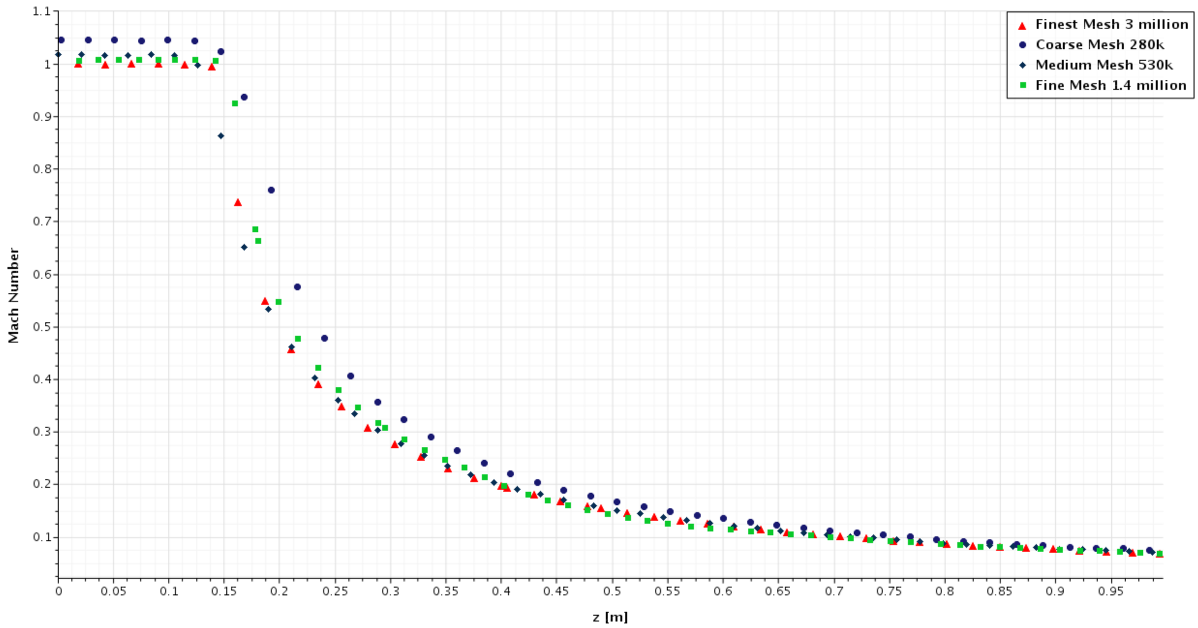

Figure 3.1: *Centerline Mach number for meshes of different size. The target was to ensure no significant changes in results between mesh refinement and that a jet of $M \approx 1$ was produced when using the notional nozzle model called the "Sonic jet approach" to simulate a jet exiting from a circular orifice.*

The simulations were done in STAR-CCM+ using the segregated solver and Realizable $k - \varepsilon$ as turbulence model. Results were achieved using second order schemes.

Gas leak properties	
Property	Value
Gas type	Non-reacting ideal gas (Methane)
Total temperature T	422 K
Stagnation pressure P	5.65 MPa
Discharge coefficient C	1
Gas constant R	518.28 J/kgK
Mass flow rate $\dot{m}$	0.0292 kg/s
Leak hole area	3 mm^2
Density (at T and P)	25.83 kg/m^3
Heat capacity ratio γ	1.32

Table 3.1: *Gas leak conditions. The leaked gas is modelled as methane.*

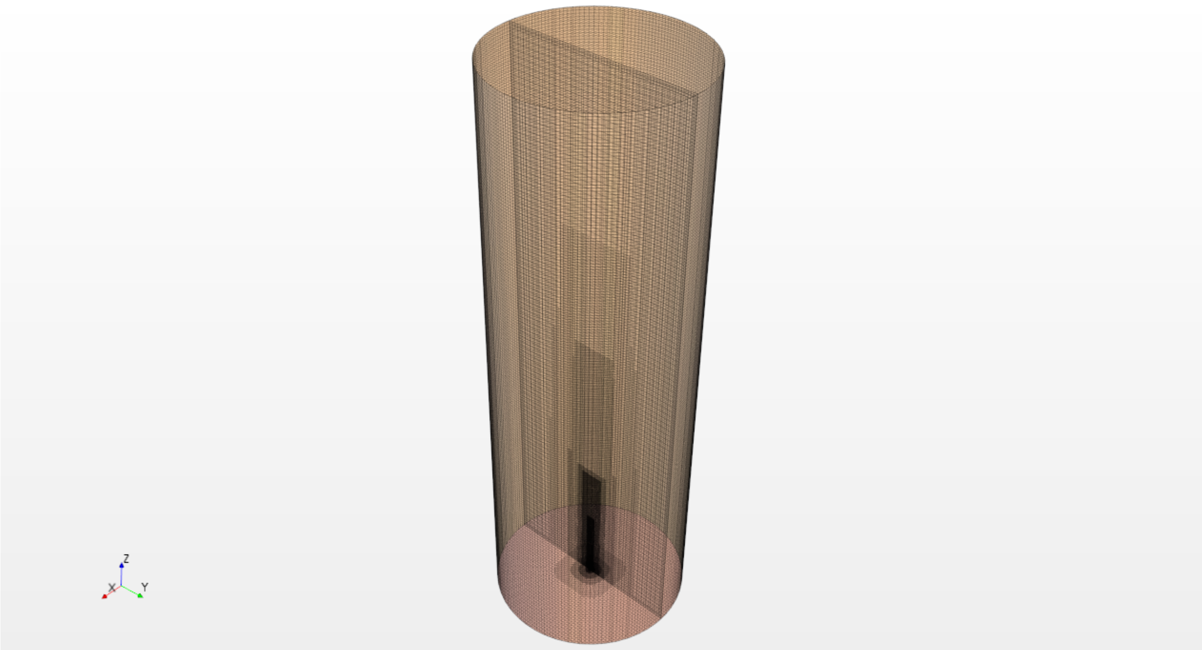

Figure 3.2: *Mesh used for jet simulations when simulating the gas leak using different shapes of the inlet.*

Resulting gas cloud volumes with higher than 100% LEL and equivalent gas volume for different orifice shapes are found in Table 3.2. It is seen that the 100 % LEL cloud volume does not change significantly with shape but is slightly larger for the circular orifice. The resulting explosive gas cloud can be seen in Figure 3.4 for the rectangular orifice with AR=15. All other shapes took on a similar shape some distance downstream from the inlet, starting to resemble a round jet.

Figure 3.3 show the radial profile for axial velocity at different distances from the jet exiting from a circular orifice. The same result for the other shapes tested is found in appendix, section A.2. It is seen that a Gaussian profile starts to form some distance downstream for all the cases and that the axi-symmetric shape.

Figure 3.5 shows the axial mass fraction evolution for the shapes tested, it appears that the circular shape has a lower rate of leaked gas mass fraction decay while asymmetric shapes, especially with higher AR seems to correlate with a more rapid drop in leaked gas mass fraction as the jet travels axially. Figure 3.6 shows the axial centerline velocity for the shapes tested, it appears that the circular has lower axial velocity decay while shapes with higher AR seems to correlate with a more rapid drop in axial velocity as the jet travels.

The conclusion drawn from the discussion above is that the circular orifice appears to be the most conservative choice concerning shape.

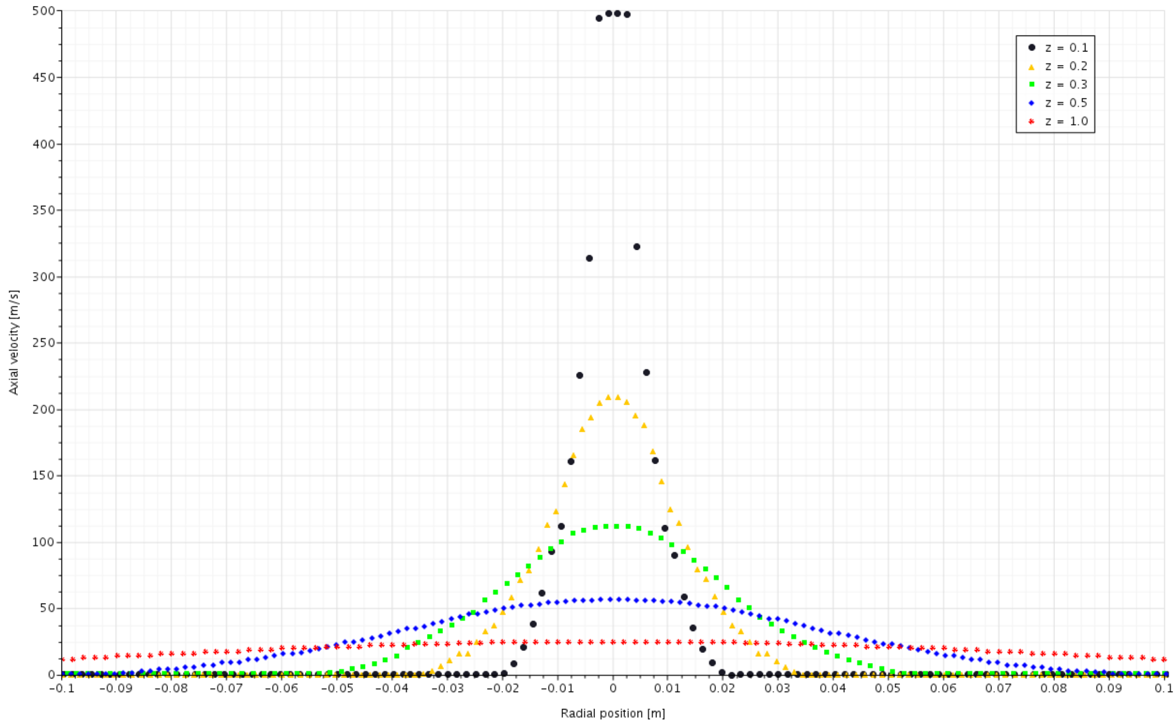

Figure 3.3: *How the axial velocity varies radially for a jet exiting from a circular orifice at different stations situated vertically above the jet exit. Simulated using the Sonic jet model.*

Results from differently shaped orifices with equal area using sonic jet approach		
	100% LEL Cloud Volume $[m^3]$	Equivalent Gas Volume $[m^3]$
Circular	0.0046	0.00352
Elliptic AR 5	0.0044	0.00333
Elliptic AR 10	0.0043	0.00324
Elliptic AR 15	0.0044	0.00333
Rectangular AR 5	0.0045	0.00343
Rectangular AR 10	0.0045	0.00343
Rectangular AR 15	0.0045	0.00333

Table 3.2: *Resulting gas cloud size for different orifice shapes.*

3.2 Influence of notional nozzle

There are several jet submodels, or notional nozzles, available. These are used to avoid having to simulate the near-field of the real jet where the flow can reach a high Mach number together with complex shock structures which are expensive to resolve. It is especially prohibitive if the jet is to be implemented in a large geometry with complex flow, as can be the case in a GT-enclosure.

To be able to evaluate the different notional nozzle models with respect to size of the resulting explosive gas cloud, the real leak jet is also simulated.

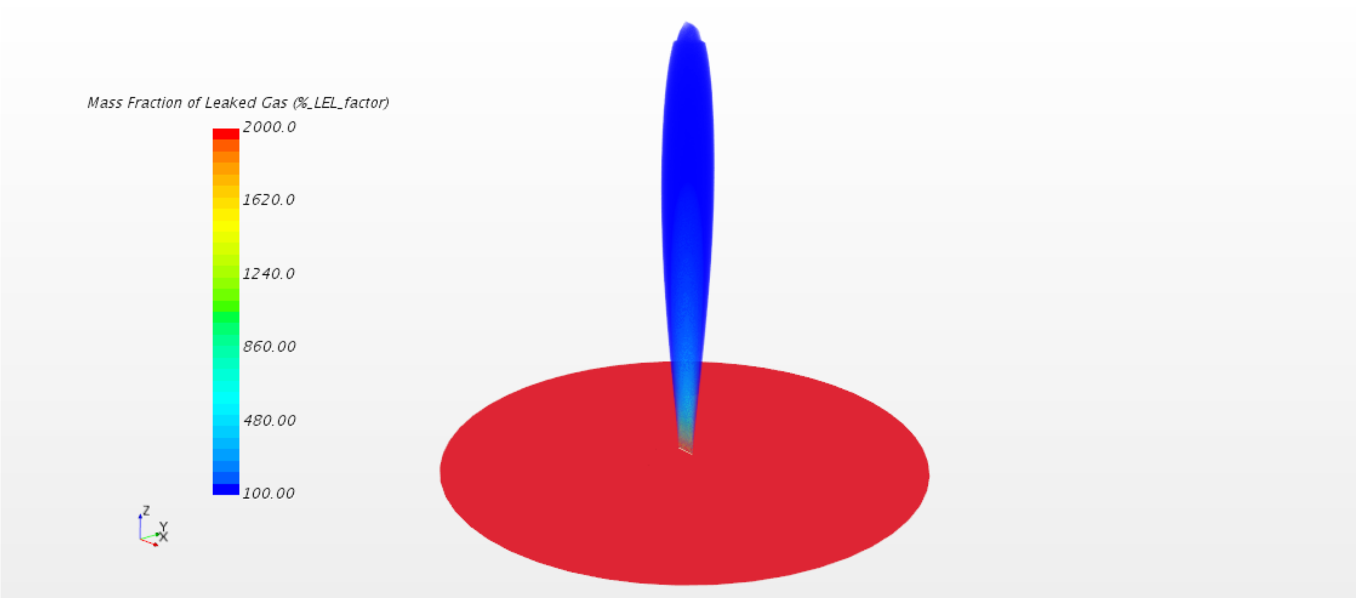

Figure 3.4: *Mass fraction over the lower explosive limit for a jet exiting from a rectangular orifice with AR=15 and the notional nozzle model the "Sonic jet approach".*

The real leak jet without use of a submodel was simulated using a coupled implicit solver as the coupled solver is known to better handle highly compressible flows. Simulations were done with a steady quasi-timestepping approach. To make convergence easier to reach, the simulations were first done on a coarse mesh which was gradually refined and the CFL number was ramped from a low to a high value to faster reach a steady solution. The third order MUSCL time scheme was used to obtain the final solution.

The near-field of the jet is seen in Figure 3.7. It appears to exhibit a barrel shock ending with a curved Mach disk. This behaviour is coherent with what should be expected from an extremely under-expanded jet as discussed in section 2.9.

Figure 3.8 shows the radial variation of axial velocity for the real jet at some stations vertically above the jet exit. Comparing with Figure A.1a it is seen that the jet has a similar evolution compared to that of a sonic jet without shocks. This supports the notion that the submodel concept is an accurate way to approximate a hypersonic jet.

The models discussed in this section assume a choked flow for the real jet, such that jet exit conditions are sonic. It should be emphasised that they are based on a hypothetical situations but made to resemble the physical flow. In a review of under-expanded jets [15], it was found that many notional nozzle models give slightly different results but most still compare reasonably well with experimental tests.

Based on results discussed in section 3.1, a circular orifice is used as the shape from

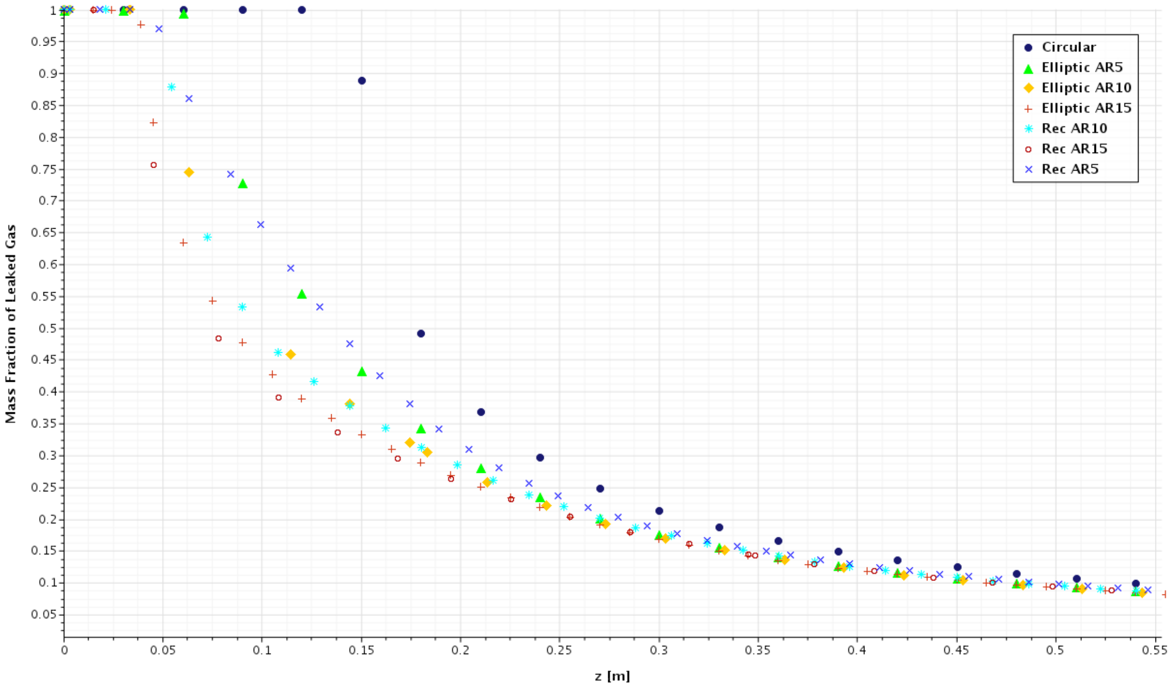

(a)

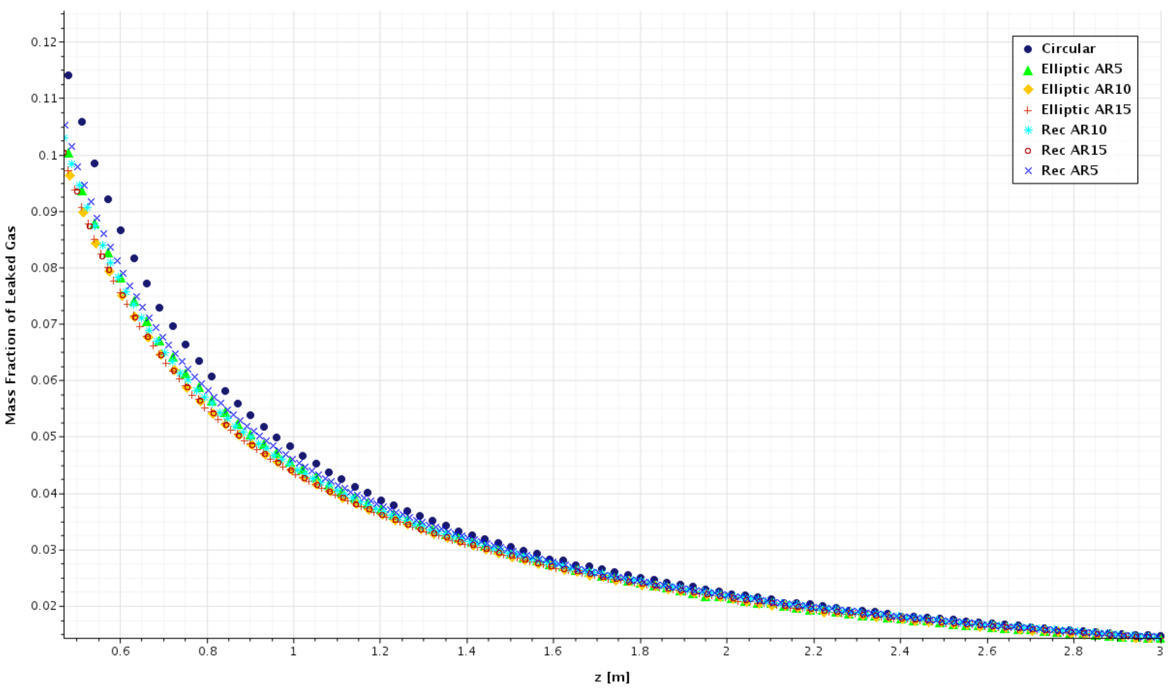

(b)

Figure 3.5: *Plots showing the evolution of centerline leaked gas mass fraction for jets exiting from different orifice shapes: a) near the jet exit, and b) further downstream.*

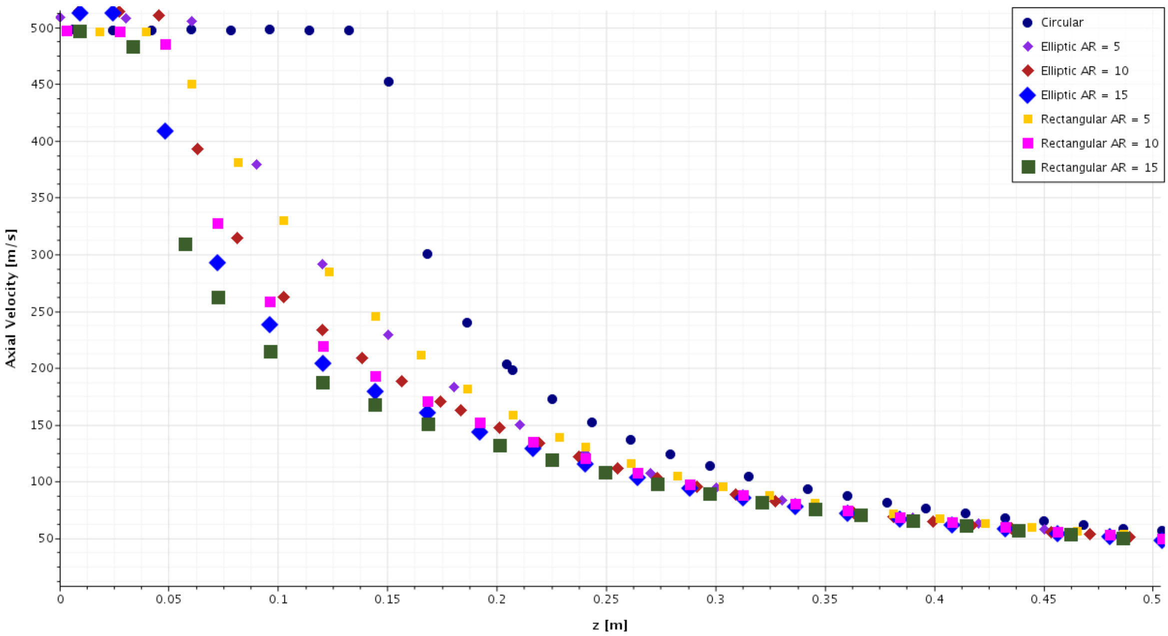

Figure 3.6: *Evolution of centerline axial velocity for a jet exiting from different orifice shapes of equal area.*

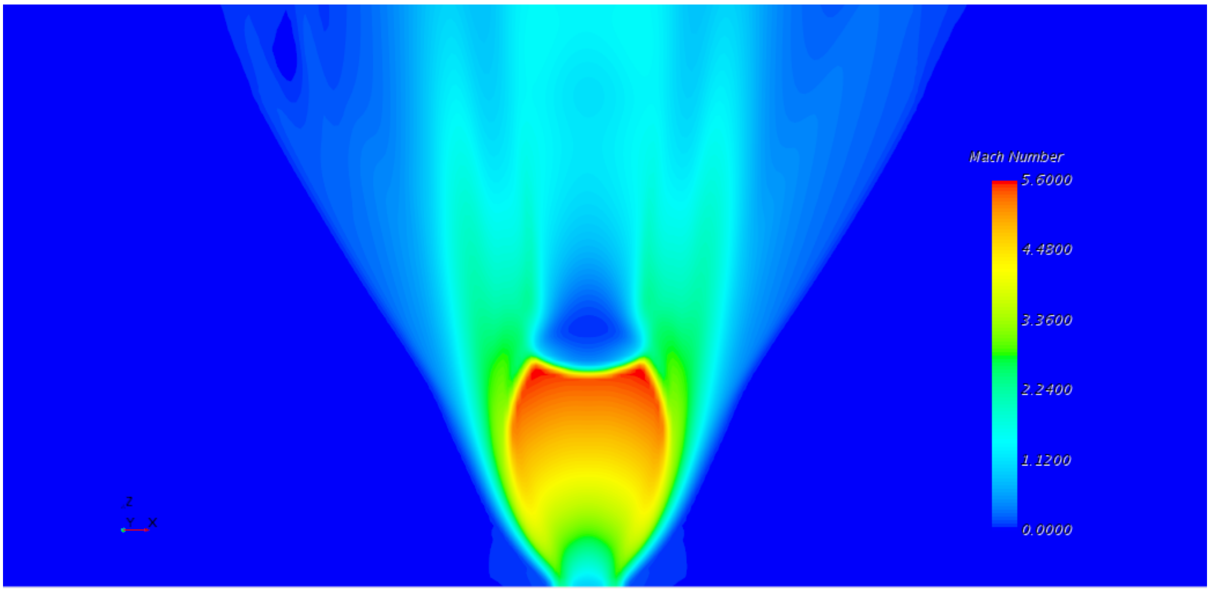

Figure 3.7: *Mach number distribution of from simulation of a jet without use of a notional nozzle model. A barrel shock concluding with a Mach disk is seen.*

which the jet exits.

Simulations of the equivalent jet using sub-models were simulated using a segregated solver except for the Adiabatic expansion approach for which a coupled solver was used since it produced a jet with $M \approx 2$.

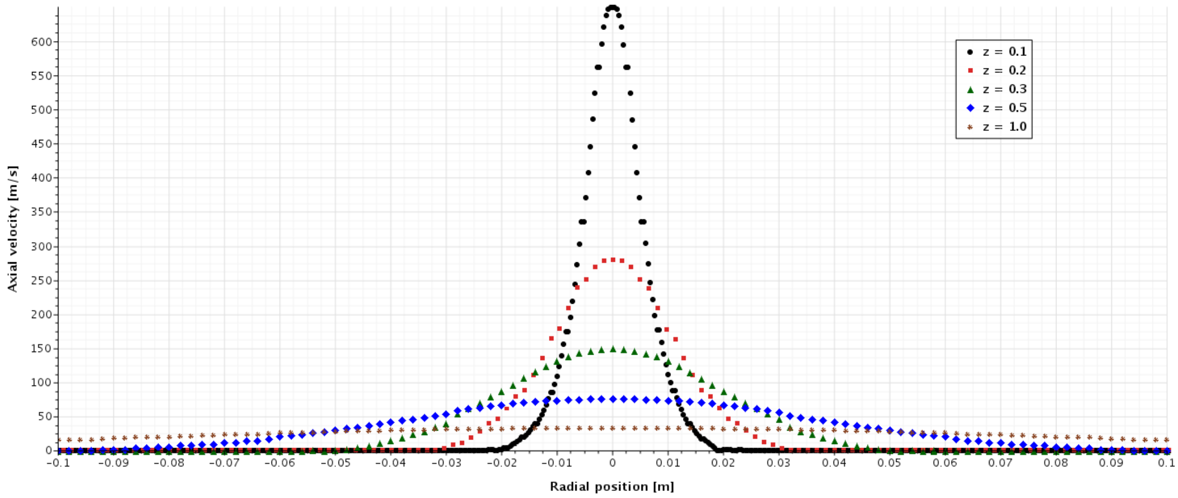

Figure 3.8: *How the axial velocity varies radially at different stations situated vertically above the jet exit. Simulation of the real jet without use of a notional nozzle model.*

3.2.1 Mach Disk Approach

The Mach disk approach, reviewed in [15], places the notional nozzle at the position of the Mach disk and attempts to calculate its diameter to use for the equivalent jet inlet diameter. The flow is assumed as perfect gas and to expand isentropically up to the Mach disk. The Mach disk is considered as a normal shock wave and the Mach number before the Mach disk is calculated from

$$\eta_0 = \frac{\left(1 + \frac{\gamma-1}{2}M^2\right)^{\gamma/(\gamma-1)}}{\frac{2\gamma}{\gamma+1}\left(M^2 - 1\right) + 1} \tag{3.3}$$

The equivalent diameter is found using

$$\frac{D_{eq}}{D_e} = \frac{1}{M}\left(\frac{1 + \frac{\gamma-1}{2}M^2}{\frac{\gamma+1}{2}}\right)^{\gamma+1/4(\gamma-1)} \tag{3.4}$$

where the index notation e is for exit conditions, 0 for stagnant conditions and eq for equivalent conditions. Furthermore η is the pressure ratio, D is diameter and γ the heat capacity ratio.

3.2.2 Improved pseudo-diameter approach

In this approach both mass and momentum is conserved.

The equivalent pressure is assumed equal to the ambient and the equivalent temperature is equal to the total temperature.

$$p_{eq} = p_{amb} \tag{3.5}$$

$$T_{eq} = T_0 \tag{3.6}$$

Assuming perfect gas and a pressure ratio far from the critical one ($\eta_0 >> \eta^*$) the equivalent diameter is calculated using [15]

$$\frac{D_{eq}}{D_e} = \sqrt{\frac{\gamma}{\gamma+1}\left(\frac{2}{\gamma+1}\right)^{1/(\gamma-1)}\eta_0} \tag{3.7}$$

3.2.3 Adiabatic expansion approach

The Adiabatic expansion approach includes mass, momentum and energy conservation [15]. Body forces, entrainment of ambient fluid and viscous forces are assumed negligible. A quasi-steady expansion up to the ambient pressure is assumed.

Mathematically this model is described with

$$p_{eq} = p_{amb} \tag{3.8}$$

with the equivalent diameter is calculated from

$$\frac{D_{eq}}{D_e} = \sqrt{\frac{\rho_e V_e}{\rho_{eq} V_{eq}}} \tag{3.9}$$

if perfect gas is assumed

$$\frac{\rho_{eq}}{\rho_e} = \frac{1}{\eta_e}\frac{T_e}{T_{eq}} \tag{3.10}$$

where isentropic relations can be used to find the pressure p_e in $\eta_e = \frac{p_e}{p_\infty}$ if p_0 is known:

$$\frac{p_0}{p_e} = \left(1 + \frac{\gamma-1}{2}M^2\right)^{\gamma/(\gamma-1)}. \tag{3.11}$$

Furthermore, the ratio between exit- and equivalent temperature can be calculated from

$$\frac{T_{eq}}{T_e} = 1 + \frac{\gamma-1}{2}M_e^2\left(1 - \left(\frac{V_{eq}}{V_e}\right)^2\right) \tag{3.12}$$

and the ratio between exit- and equivalent velocity from

$$\frac{V_{eq}}{V_e} = 1 + \frac{1}{\gamma M_e^2}\frac{\eta_e - 1}{\eta_e} \tag{3.13}$$

3.2.4 Sonic Jet Approach

The model, reviewed in [15], relies on mass conservation, assumes no entrainment on air, temperature is assumed same as on the exit plane and pressure equal to ambient pressure. Uniform velocity and mass fraction is assumed at the point where sonic conditions are returned to.

In mathematical notion this becomes

$$p_{eq} = p_{amb} \tag{3.14}$$

$$T_{eq} = T_e \tag{3.15}$$

$$V_{eq} = a_{eq} \tag{3.16}$$

The equivalent diameter is found as

$$\frac{D_{eq}}{D_e} = \sqrt{\frac{\rho_e V_e}{\rho_{eq} a_{eq}}} \tag{3.17}$$

If perfect gas can be assumed the above equation can also be written as

$$\frac{D_{eq}}{D_e} = \sqrt{\left(\frac{2}{\gamma+1}\right)^{\gamma/(\gamma-1)} \frac{p_0}{p_\infty}} \tag{3.18}$$

The perfect gas assumption is a reasonable assumption and the small error induced by using it should be on the conservative side, if anything slightly overestimating the mass release [19]. The assumption of the ideal gas model as an acceptable choice for the pressure ratio in this case is validated by the conclusions drawn in [20].

3.2.4.1 Sonic Jet Approach adjustment

The Sonic Jet Approach model is attractive to use since its low Mach number makes it affordable to use, but from results presented in Table 3.3, this model appears overly conservative and would need to be modified to produce a gas cloud of realistic size. In light of this, an adjustment to the Sonic jet model is proposed that takes air entrainment and mass flux variation in account. With these modifications implemented, the resulting size of the explosive gas cloud is more similar to results from the real jet simulation.

It should be noted that this adjustment is empirical and based on the result from the simulation of the real jet simulation. Further validation with other pressure ratios, gas types, co-flow velocities etc could be needed.

This adjustment utilizes the fact that quantities in a developed round jet take on a Gaussian profile and hence MATLAB's Gaussian curvefitting tool was used to produce equations (3.2.4.1), (3.22) and (3.23).

Total mass flow in the jet is:

$$\dot{m}_{tot} = \dot{m}_{leak} + \dot{m}_{air} \tag{3.19}$$

where it was found that at the return to sonic conditions

$$\dot{m}_{air} \approx 4.14\dot{m}_{leak} \tag{3.20}$$

and the new jet radius

$$r_{eq,adj} \approx 4.22 r_{eq} \tag{3.21}$$

the leaked gas mass fraction distribution using a Gaussian profile is

$\mathrm{c}_{leak} = 0.07154 * exp(-(\frac{r-0.01233}{0.006289})^2) + 0.007125 * exp(-(\frac{r-0.004146}{0.0001524})^2) +$

$0.4485 * exp((\frac{r+7.507e-06}{0.008851})^2) + 0.01496 * exp(-(\frac{r-0.01922}{0.003908})^2)$

and for air

$$c_{air} = 0.9894 * exp\left(-\left(\frac{r-0.02376}{0.03003}\right)^2\right) \tag{3.22}$$

furthermore the adjusted mass flux is

$$j_m = 333.1 * exp\left(-\left(\frac{r+0.0005934}{0.01092}\right)^2\right) + 35.86 * exp\left(-\left(\frac{r-0.0144}{0.006778}\right)^2\right) \tag{3.23}$$

3.2.5 Evaluation of sub-models

Figure 3.9 shows the evolution of the centerline mass fraction of the leaked gas. Close to the inlet it is difficult to say which notional nozzle best predicts the real jet but further away it becomes clear that the Mach disk, Sonic jet and Improved pseudo-diameter submodels over predict the centerline mass fraction while the Adiabatic expansion and Adjusted sonic jet submodels are close to the results from the real jet.

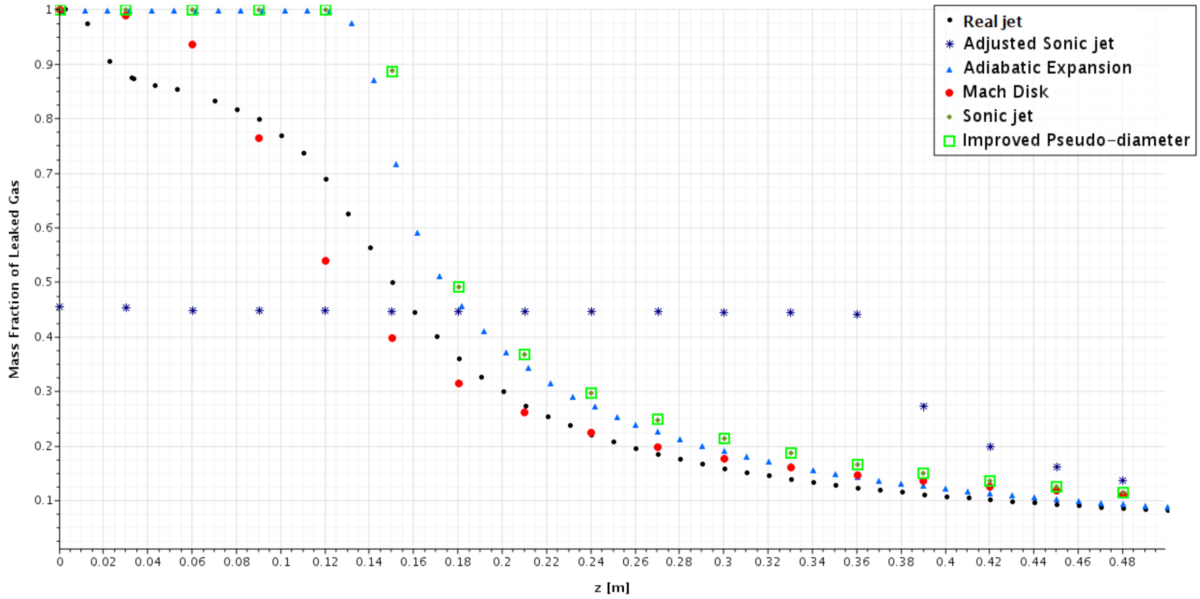

(a)

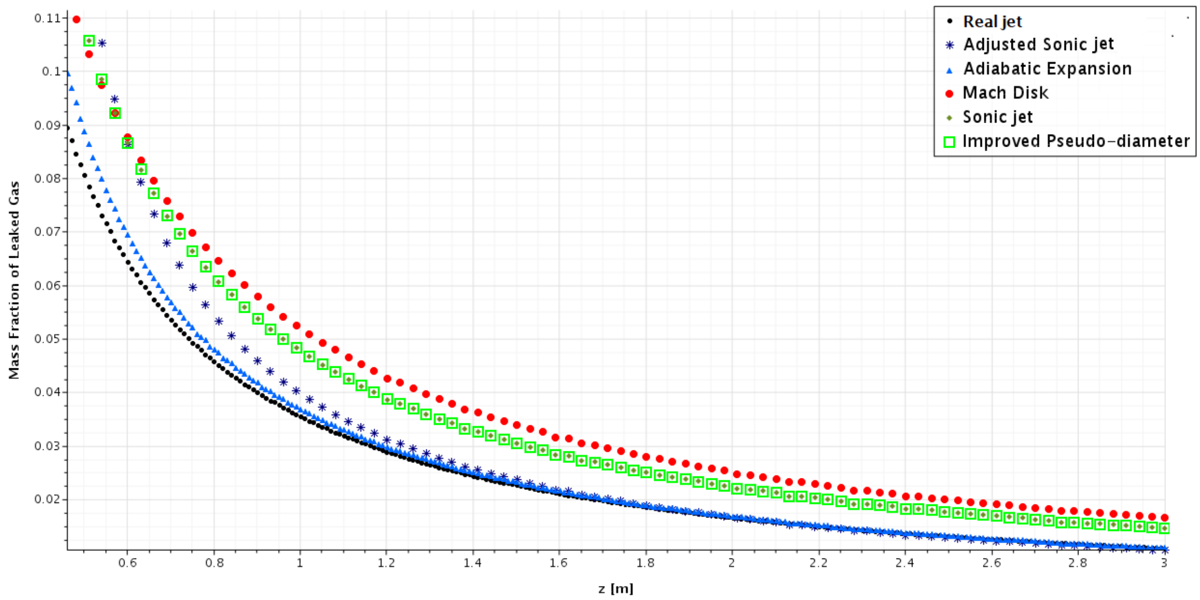

(b)

Figure 3.9: *The evolution of centerline leaked gas mass fraction for simulation of a jet with and without notional nozzle models: a) near the jet exit, and b) further downstream.*

Figure 3.10 shows the evolution of the centerline Mach number for the submodels discussed and the equivalent jet without submodel. As in Figure 3.9, the result is similar with no submodel comparing to the real jet close to the jet exit but further downstream especially the Adiabatic expansion submodel shows good comparison to the simulation of the real jet. That the notional nozzle models doesn't compare well close to the jet exit is to be expected since they don't aim to simulate this part of the real jet.

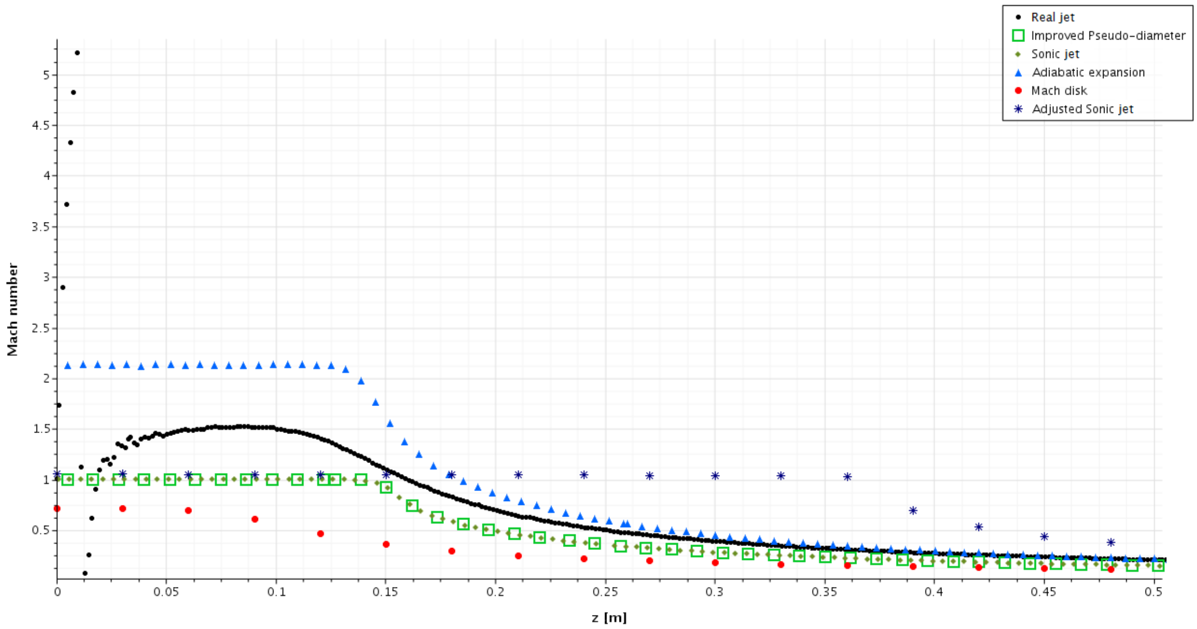

(a)

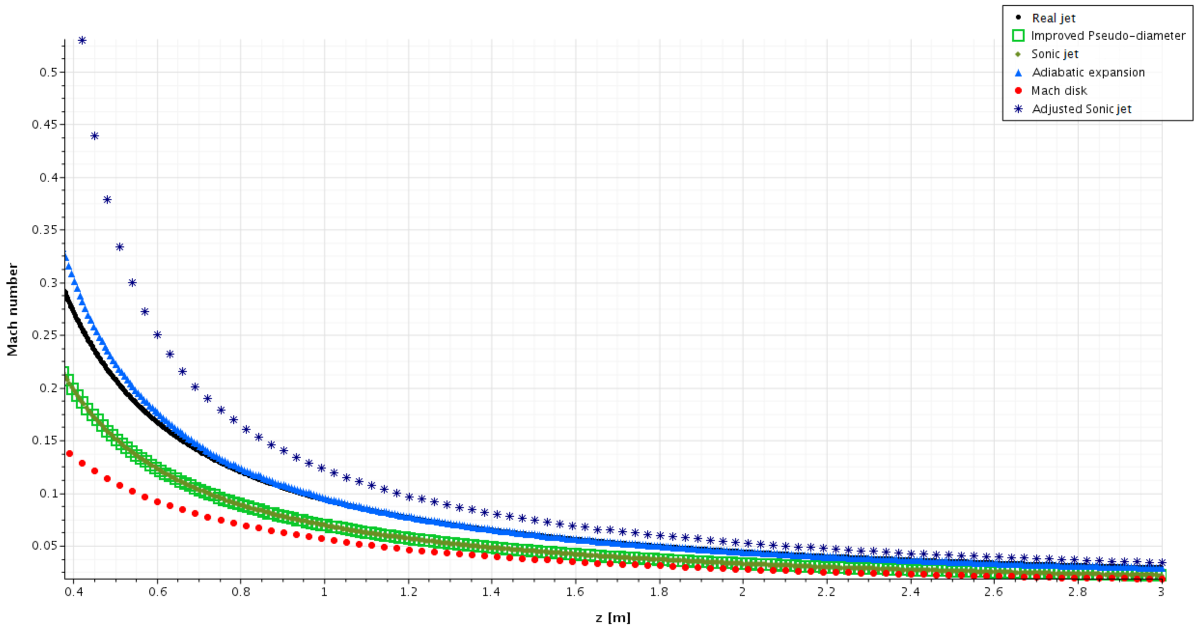

(b)

Figure 3.10: *The evolution of centerline Mach number for simulation of a jet with and without notional nozzle models: a) near the jet exit, and b) further downstream.*

Table 3.3 presents the results from modeling a round jet with and without submodels. The condition of the gas leak is found in Table 3.1.

Results from simulations with real jet and equivalent jets using notional nozzle models.						
Not. nozzle	Im. pseudo-dia.	Sonic	Ad.Sonic	Mach disk	Ad exp.	"Real" jet
Inlet area [cm^2]	0.7284	1.1036	1.9600	1.5844	0.4273	0.036
100% LEL Vol.[m^3]	0.0046	0.0046	0.0019	0.0071	0.0020	0.0019
Eq. Gas Volume [m^3]	0.00352	0.00352	0.00159	0.00533	0.00152	0.00143

Table 3.3: *Comparison of resulting explosive gas cloud for modeling a supersonic leak jet with and without submodels.*

From the information presented in Table 3.3, the conclusion can be drawn that all submodels produce equivalent jets that are conservative with respect to size of the 100 % LEL cloud volume and equivalent gas volume compared with results from the real jet. The Adiabatic expansion approach appears to most closely represent the real jet while the other submodels overpredict the size of the explosive gas cloud. The Sonic jet approach does predict a jet at sonic speed with $M \approx 1$, so does the Improved pseudo-diameter approach while a lower Mach number is seen for the Mach disk approach with $M \approx 0.7$ and a higher Mach number for the Adiabatic expansion approach with $M \approx 2$.

The large difference in predicted explosive gas cloud size needs to be investigated and a logical first step is to evaluate if the assumptions made when using the submodels are valid.

The submodels all neglect entrainment of air upstream of the placement of the equivalent jet. This simplification could be the major source of difference in results as in reality there could have been considerable mixing of air before jet returns to for example $M = 1$ (as for the Sonic jet approach). Figure 3.11 shows the radial distribution of the leaked gas at $M = 1$ for the real jet and the equivalent jet modelled using the Sonic jet approach. It appears that the assumption of no entrainment of air upstream of when the jet returns to $M = 1$ does not produce a realistic jet cross section and could be the reason for the overprediction in results. To evaluate the effect of this assumption, the radial mass fraction- and mass flux distribution at $M \approx 1$ of the real jet was used to set the boundary condition at the inlet in a simulation using the Sonic jet approach. Note that this also changes the mass flow and inlet area at the inlet because of the added air. The result was a jet with an explosive gas cloud size much more similar to the result from the real jet. The 100 % LEL cloud volume decreased from 0.0046 m^3 to 0.0019 m^3 when changing from the Sonic jet approach to the Adjusted sonic jet.

In conclusion, the assumption of no prior entrainment of air appears to overpredict the size of the explosive gas cloud when using the Sonic jet approach. The same conclusion can be drawn to hold for the Improved pseudo-diameter.

The Mach disk model could suffer from the fact that the Mach disk seen when simulating the real jet is curved and a normal shock might be a bad representation

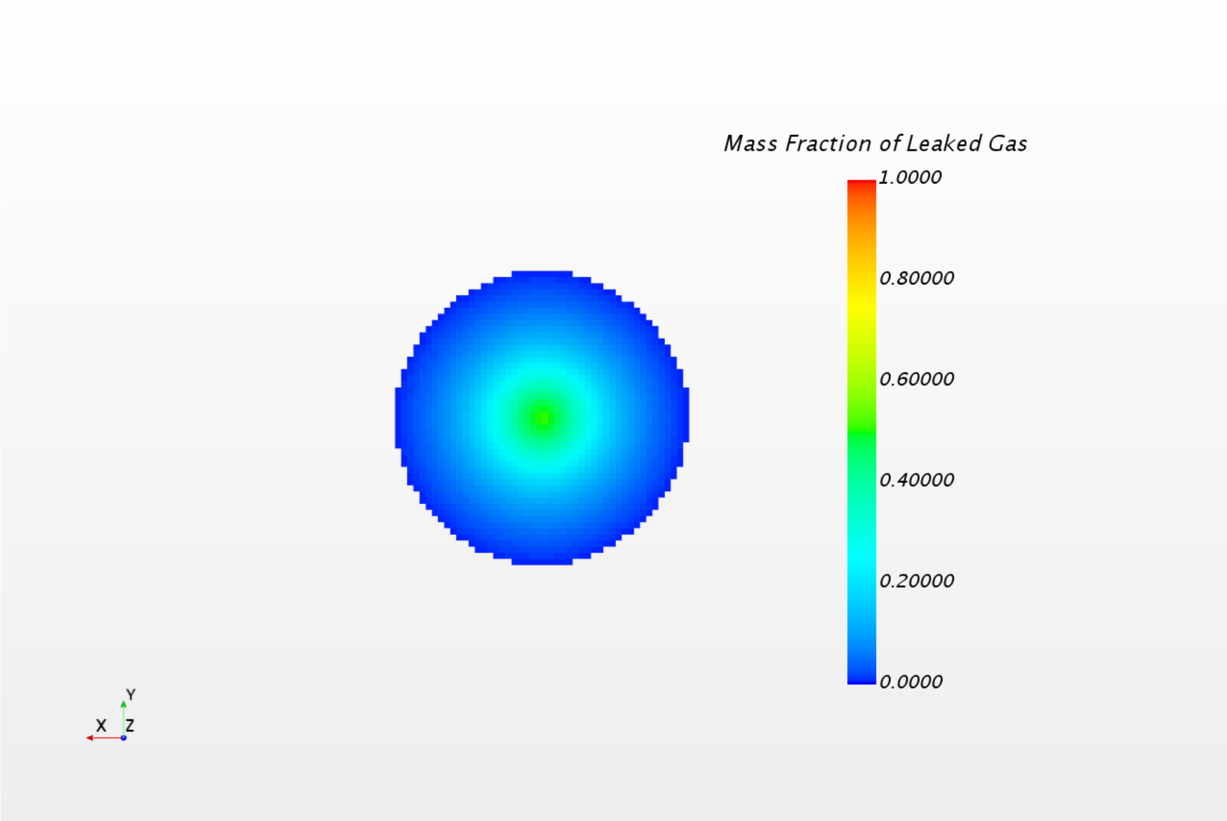

(a)

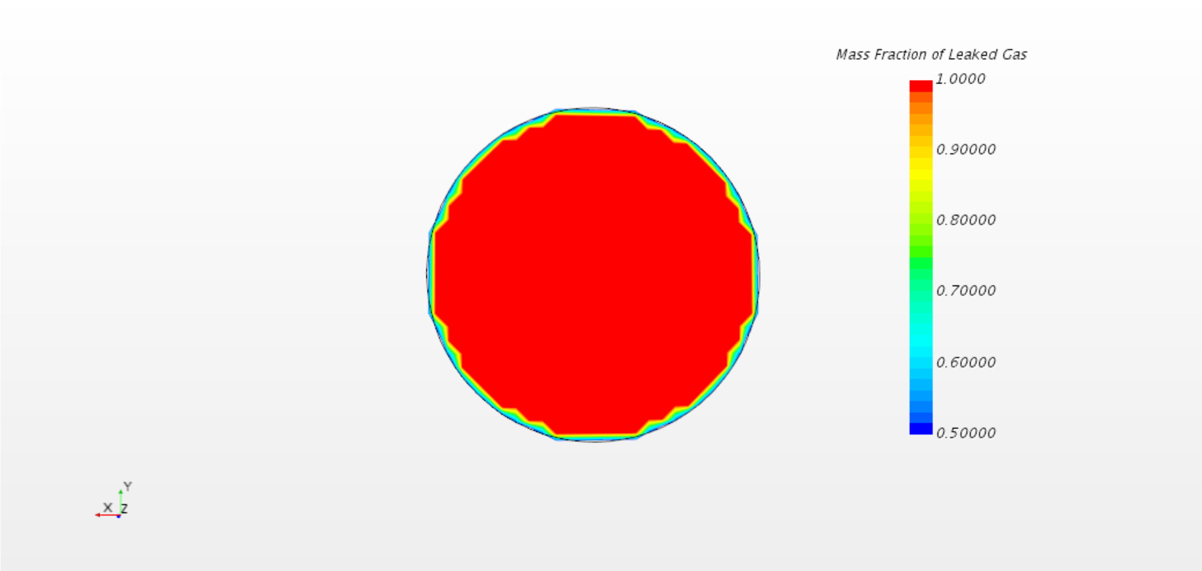

(b)

Figure 3.11: *The radial mass fraction distribution of the leaked gas at $M \approx 1$ for the simulation of a) the real jet and b) the equivalent jet simulated using the Sonic Jet Approach.*

of it and even more so from not being able to account for supersonic flow that flows around the Mach disk, maybe being able to expand without shocks at all or only inhibiting weaker shocks. That the Mach disk approach could be a bad representation of the real flow after a Mach disk can be seen in Figure 3.12.

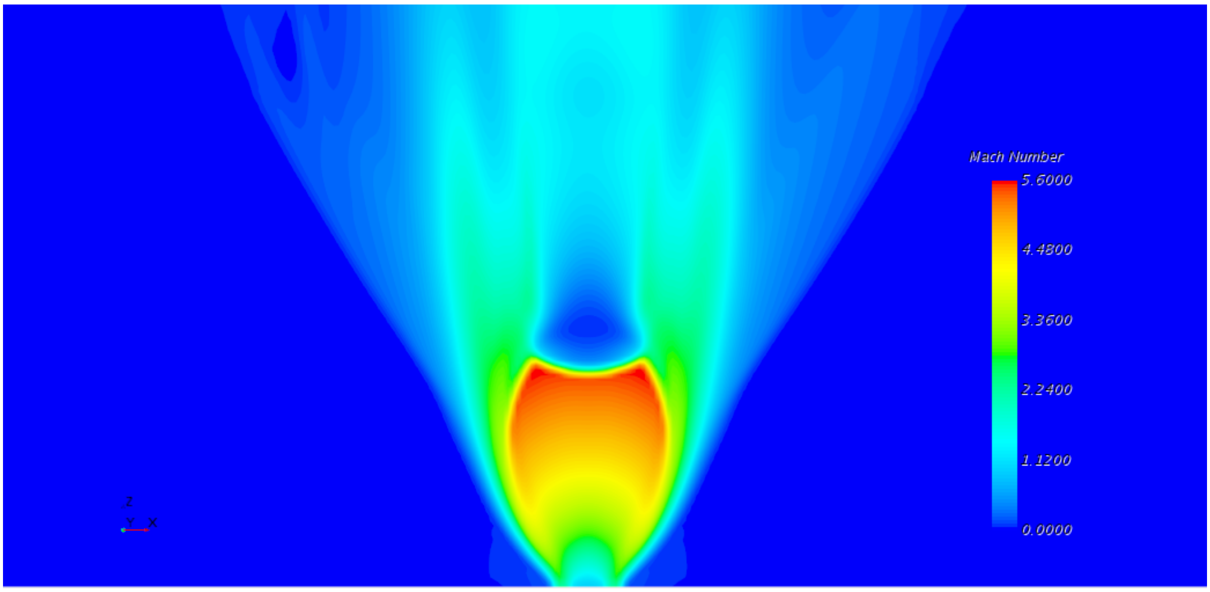

(a)

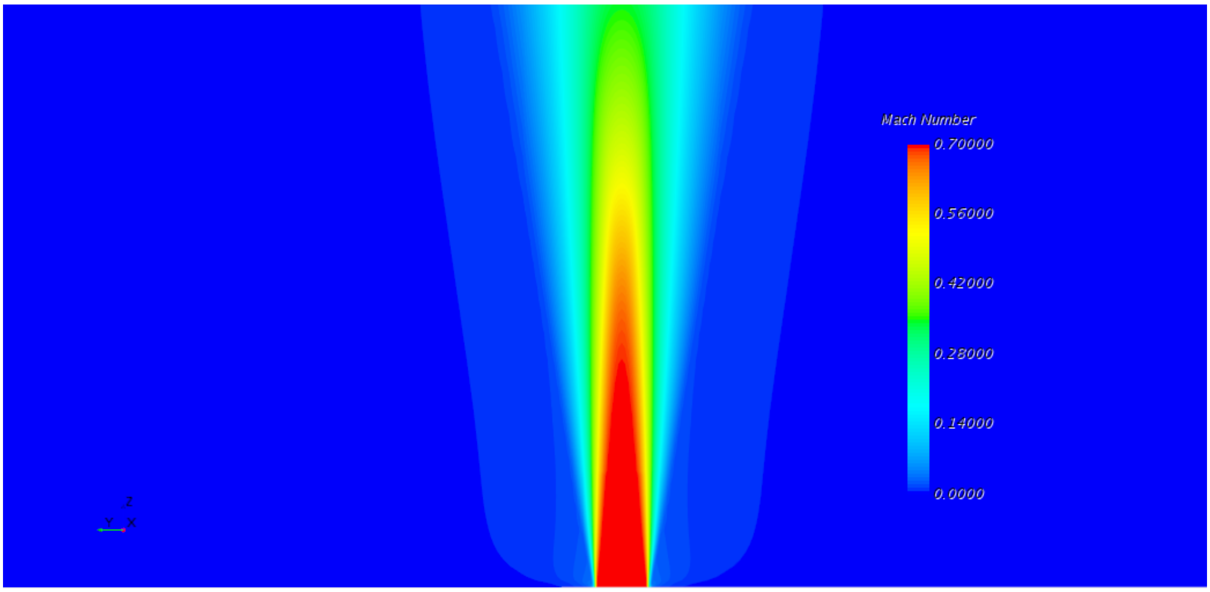

(b)

Figure 3.12: *The Mach number distribution for the nearfield of a) the real jet, and b) the equivalent jet simulated using the Mach disk approach. The flow of the real jet has flow that does not pass through the Mach disk and get slowed to subsonic speed while using the Mach disk approach results in an entirely subsonic jet.*

For the Adiabatic expansion approach, the assumption of no air entrainment appears to be more valid as the resulting 100 % LEL clould is very similar to the results from the real jet. The same with respect to similarity with the real jet can be said for the axial evolution of mass fraction and Mach number which is seen is Figure 3.9 and Figure 3.10 respectively. This may be because the equivalent jet is more similar to the real jet before any considerable mixing of air has taken place. Referring to the discussion in section 2.9 , this equivalent jet should represent the real jet somewhere in the transition region since the pressure of the jet is assumed to have equalized with the ambient pressure. The small difference in results with the real jet results could potentially be due to neglect of the ambient air entrainment taking place in the mixing layer of the near-field region. Since it is on the conservative side, predicting a slightly larger explosive gas cloud size, it is not seen as problematic. A potential downside of this model is that for this case, the resulting equivalent jet is still supersonic with $M \approx 2$ as seen in Figure 3.10. This is however still much lower than the real jet, as seen in Figure 3.7, and the flow does not exhibit shocks.

4

GT-enclosure analysis

This chapter concerns analysis when the whole GT-enclosure is considered. It aims to evaluate the main differences in results when using RANS versus LES methods for modelling the turbulent mixing between the leaked gas and ventilation air. The difference in size of the explosive gas volume is the focus.

4.1 Meshing method

A simplified geometry of a gas turbine enclosure was used. The geometry is shown in Figure 4.1, Figure 4.2 and Figure 4.3. Figure 4.2 also points out the locations for ventilation air inlet and outlet, as well as the region where the leak is placed.

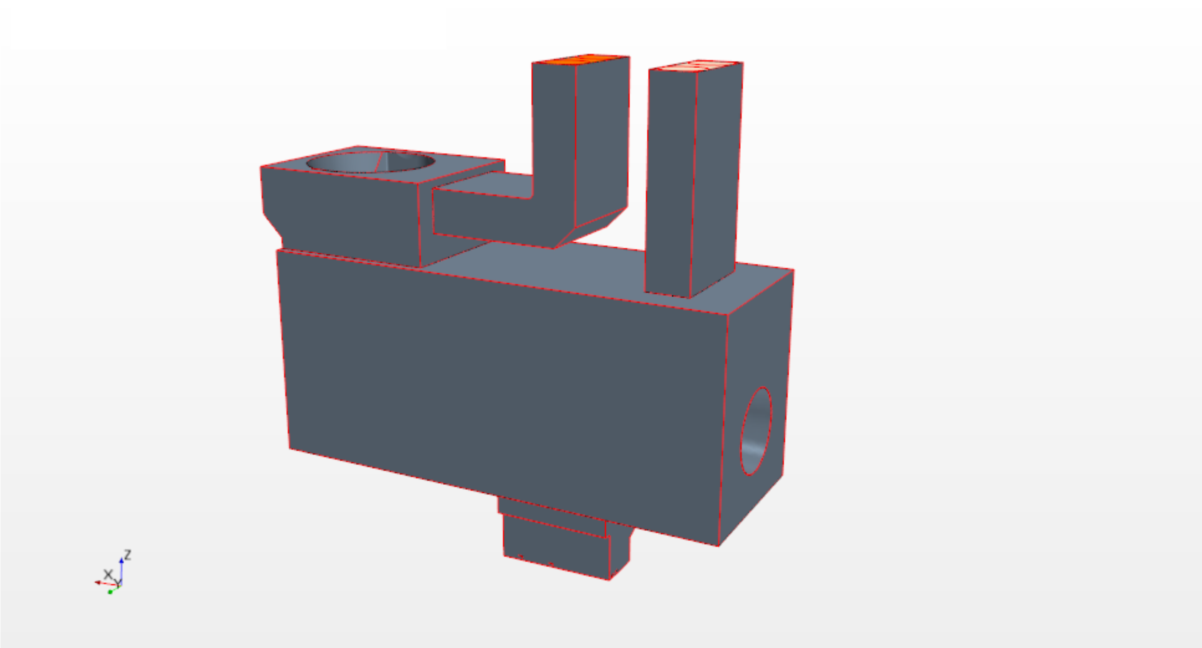

Figure 4.1: *Simplified geometry with outer walls shown.*

To build the mesh the trimmed cell mesher and the prism layer mesher available in STAR-CCM+ were used. The trimmed mesher constructs hexahedral cells which

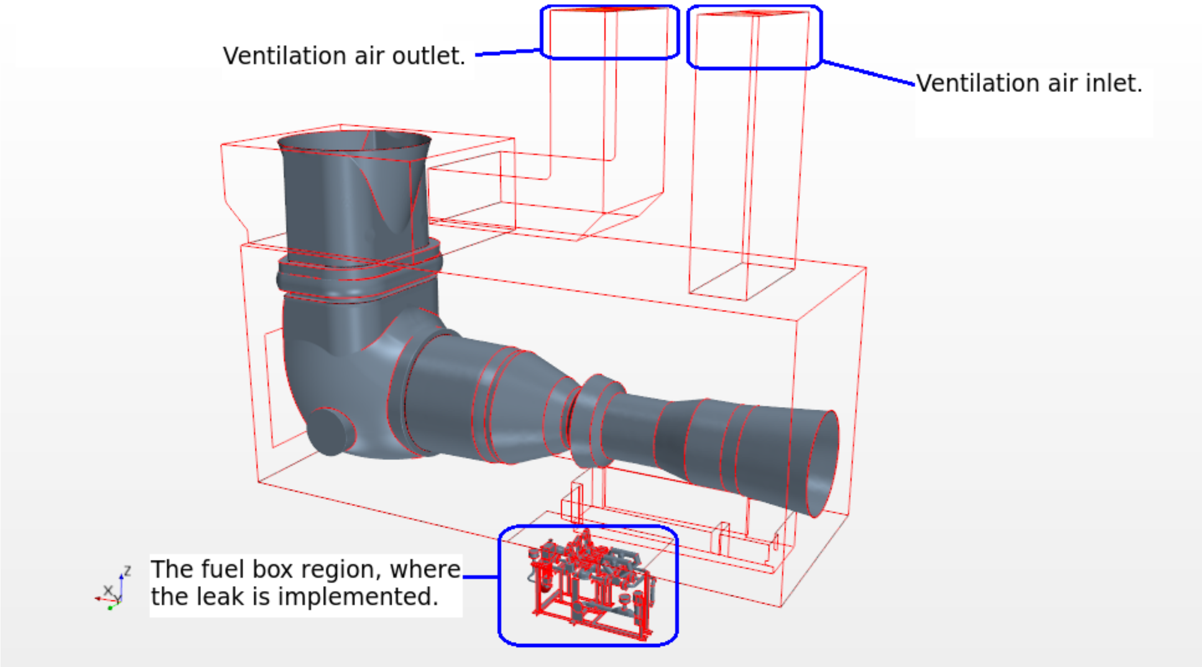

Figure 4.2: *Simplified geometry with gas turbine and fuel box system shown. Inlet and outlet for the ventilation air is pointed out. The region for where the leak is placed is also marked out.*

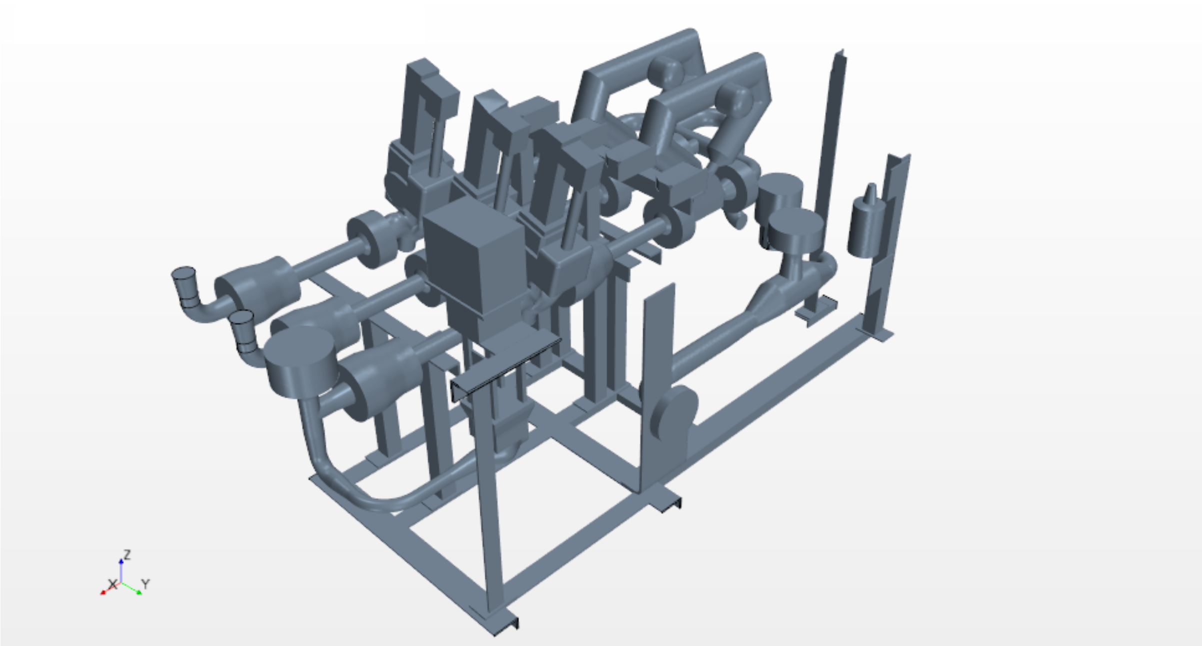

Figure 4.3: *Geometry of the simplified fuel box system.*

are trimmed (polyhedral) cells near surfaces. The choice of the trimmed mesher can be justified by citing the STAR-CCM+ user guide: "The trimmed cell mesher provides a robust and efficient method of producing a high-quality grid for both simple and complex mesh generation problems." [6]. The prism layer mesher is used to better capture boundary layer effects near surfaces.

Meshes of equal size were used for both the RANS and LES simulations as this was a request of the proposers of the thesis. Cell spacing was 10 cm in the outer region everywhere except for in the fuel box region where spacing of around 2.5 cm was used and even finer where the leak was implemented since large gradients were expected there. Part of the mesh is shown in Figure 4.4 and a zoomed in cut of the mesh near the turbine is shown in Figure 4.5.

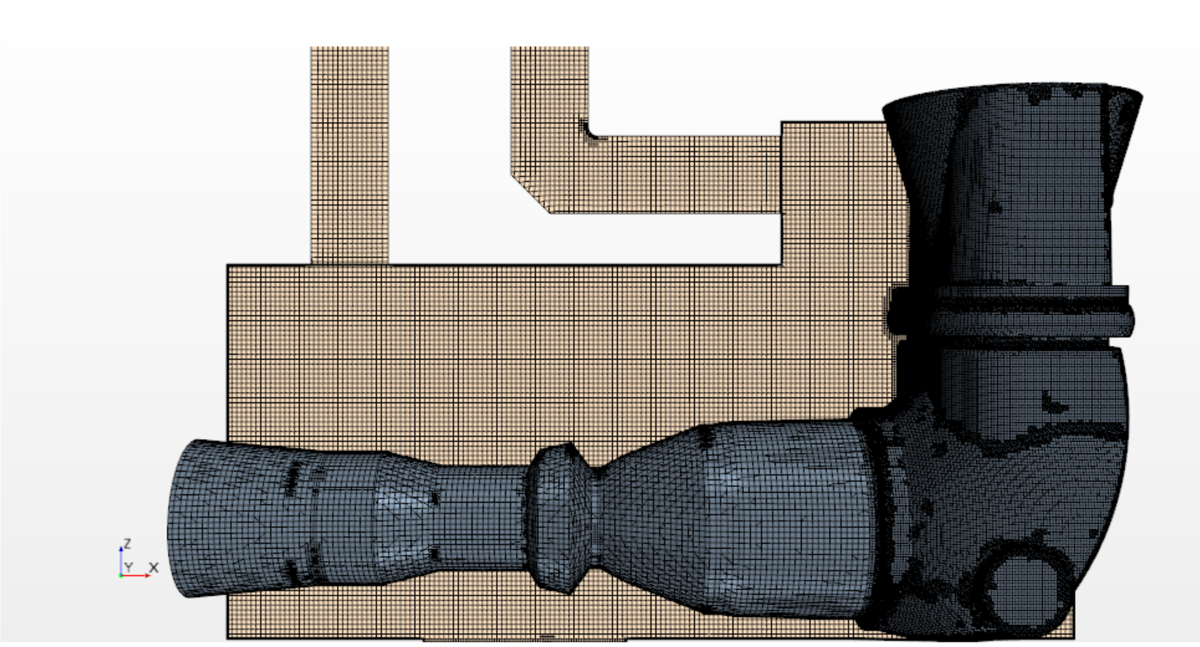

Figure 4.4: *Cutout of the mesh.*

To ensure that boundary layer effects were well captured, the "All y+ Wall Treatment" was used. For this approach, the y^+ values close to surfaces should correspond to the inner region, meaning to not be above 500. The y^+ values are shown in Figure 4.6 and Figure 4.7.

4.2 Simulation strategy

For the simulations, the strategy was to start with a simple model (eg constant density, no buoyancy and no leak), then gradually add more complexity. This made troubleshooting easier and the result from using a simple model could be used as initial condition in a more complex simulation to facilitate convergence. For the same reason certain boundary conditions were implemented using a ramp function.

The specification of boundary conditions are shown in Table 4.1. A temperature profile shown in Figure 4.8 made to approximate a realistic case was used.

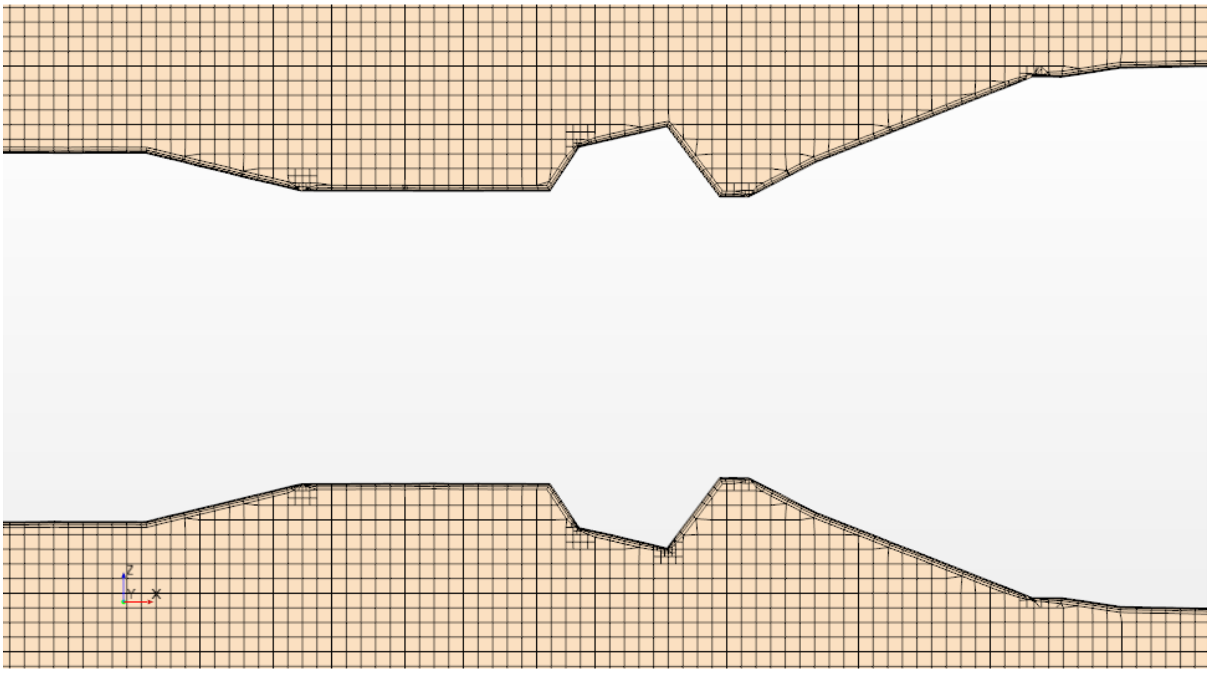

Figure 4.5: *Zoomed-in view of the mesh near the turbine.*

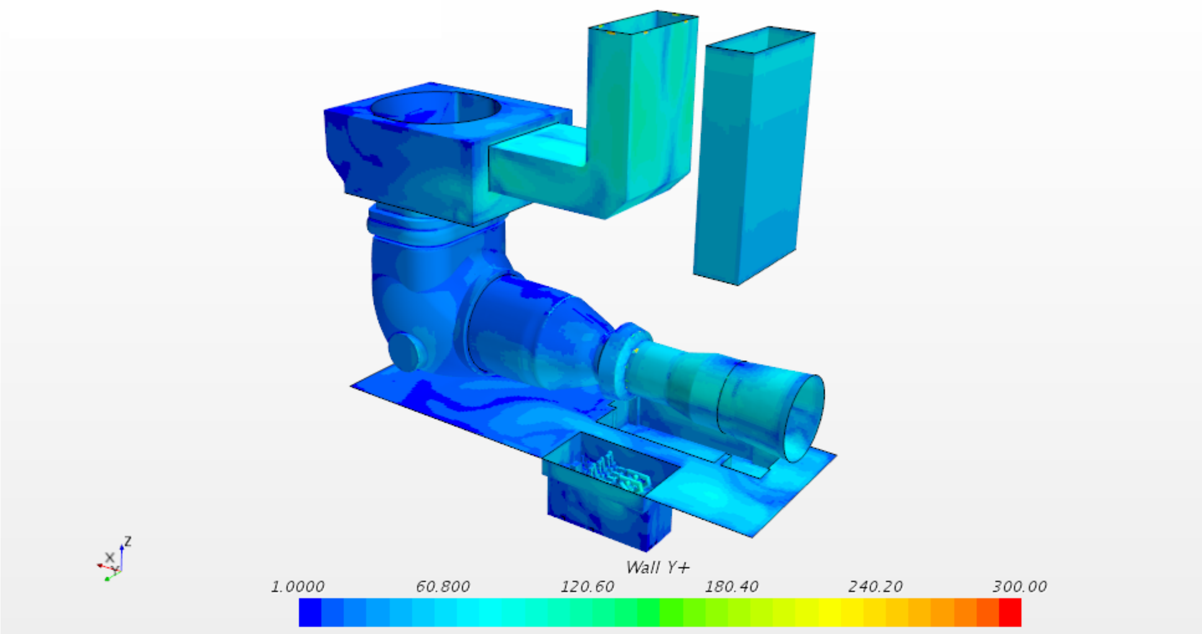

Figure 4.6: *y^+ values in the entire domain.*

When doing RANS simulations, it became apparent that the case studied is ill-suited for a steady RANS-model since a convergent solution could not be reached and the resulting flow field changed significantly with more iterations. Realizing this, unsteady RANS (URANS) was chosen instead to be compared with LES. The unsteadiness is thought to in part be a cause of vortex shedding around the turbine.

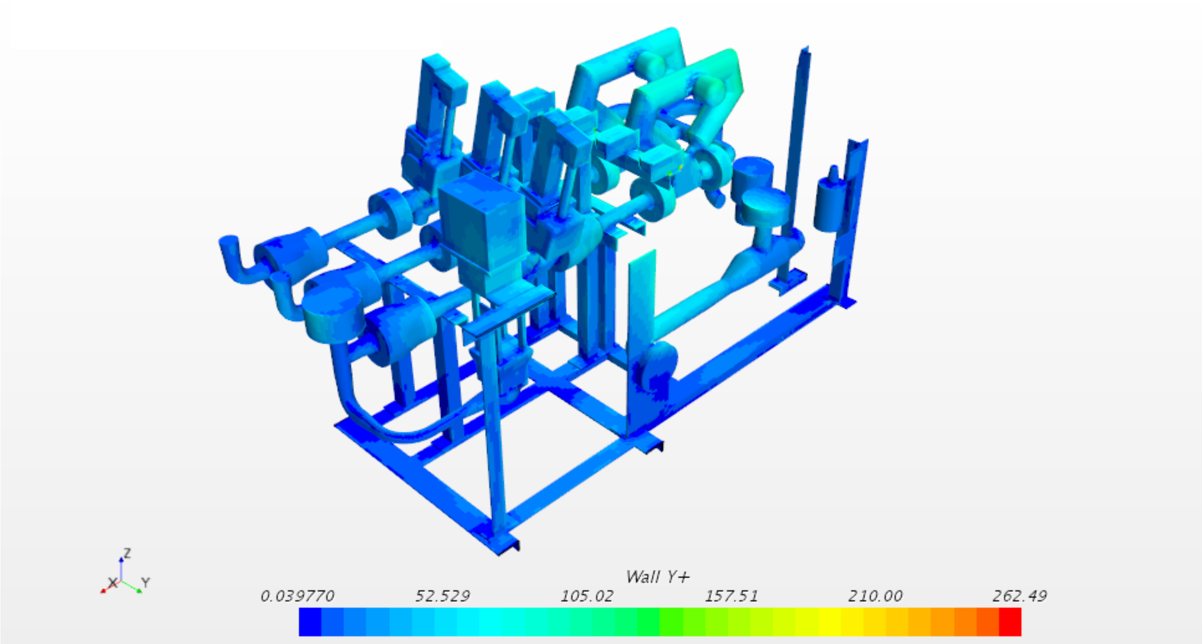

Figure 4.7: *y^+ values near the fuel box surface.*

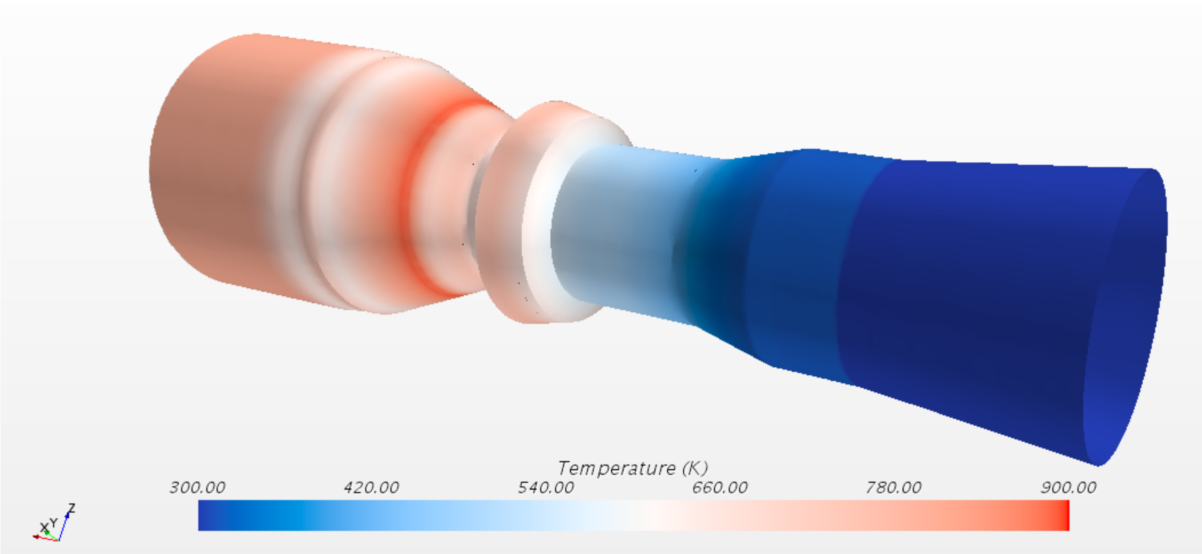

Figure 4.8: *The temperature profile used as a boundary condition for the simplified turbine.*

To initialize the LES, the solution from the URANS simulation was used. In large part the STAR-CCM+ LES guidelines [6] was followed. When the simulations were thought to have reached a state representing fully developed conditions, sampling of quantities of interest was started to find representative mean values. To estimate when sampling of quantities could start, the mean of velocity magnitude and components were monitored at a number of points placed at different locations in the flow domain and sampling was started when these had reached a stable state.

Boundary conditions	
Boundary	Type
Vent inlet	Mass flow inlet
Vent outlet	Pressure outlet
Turbine surface	Temperature profile
Other walls	Adiabatic
Gas fuel system surface	Static temperature
Turbine transition duct	Convective

Table 4.1: *Boundary conditions for GT-simulations.*

Table 4.2 summarizes the model setup for the RANS, URANS and LES simulations.

Model setup			
	RANS	URANS	LES
Wall treatment	All y+ Wall Treatment	All y+ Wall Treatment	All y+ Wall Treatment
Gas model	Ideal	Ideal	Ideal
Turbulence model	$k-\omega-SST$	$k-\omega-SST$	WALE
Solver	Segregated (2nd order)	Segregated(2nd order)	Segregated(Bounded-Central)
Energy model	Seg. Temperature (2nd order)	Seg. Temperature (2nd order)	Seg. Temperature (2nd order)
Gravity	on	on	on
Transient solver	-	Implicit (2nd order)	Implicit (2nd order)
Time step	-	10^{-4} s	$5 * 10^{-5}$ s

Table 4.2: *Model setups for RANS, URANS and LES simulations.*

4.2.1 Gas leak implementation

The gas leak was implemented where low mixing with the ventilation air was expected. This location be could found from analyzing results from simulations without any leak implemented and finding regions with low flow velocity. The region where the jet was implemented is seen in Figure 4.14.

A leaked gas massflow of 0.0292 kg/s was used, this represents a leak area of 3 mm^2 using equation (2.39).

A discharge coefficient of one was used as it represents the conservative approach for accidental gas releases [21].

The notional nozzles chosen to model the hypersonic part of the leak were the Adiabatic expansion approach, as it appears both conservative and to closely represent the real leak, and the Sonic jet model as it is the industry standard. Equivalent nozzle diameters were calculated using equations (3.9) and (3.18).

From the findings discussed in Section 3.1, the leak was modelled as exiting from a circular orifice.

The characteristics of the jet are found in Table 3.1.

To estimate the placement of the equivalent jet, i.e. how far from the hypothetical real leak jet exit it should be implemented, equation (2.40) was used.

4.2.2 Choice of time step

For unsteady simulations, the choice of time step is important. The time step size should ideally be chosen so that all unsteady processes possible to resolve with a given method (e.g. RANS or LES) are properly captured. A challenge in industrial problems is that one often have to balance capturing the important physics for the problem at hand and keeping simulation time a acceptable level.

The time-step control in STAR-CCM+ can be useful to find a suitable timestep. It automatically adjusted the time step to keep the CFL number within acceptable range . Optimally, this would mean $Co \leq 1$ in the entire region but this was found to not be feasible where the leak was implemented as it would result in a prohibitively small time step. A time step of $5 * 10^{-5}$ s for the LES when using both submodels. For URANS $2 * 10^{-4}$ s was used for simulations involving the Sonic jet submodel and $1 * 10^{-4}$ s for simulations involving the Adiabatic expansion submodel. The resulting Courant number distributions are shown in Figure 4.10 . As the flow near the leak is rather uniform, it was deemed acceptable to have slightly larger Courant number there.

In unsteady simulations, there is often an inner iteration loop occurring for each time step. The number of inner iterations used in both the URANS and LES simulations were selected to five, this seemed to provide a good balance between computational time needed and accuracy for each time step.

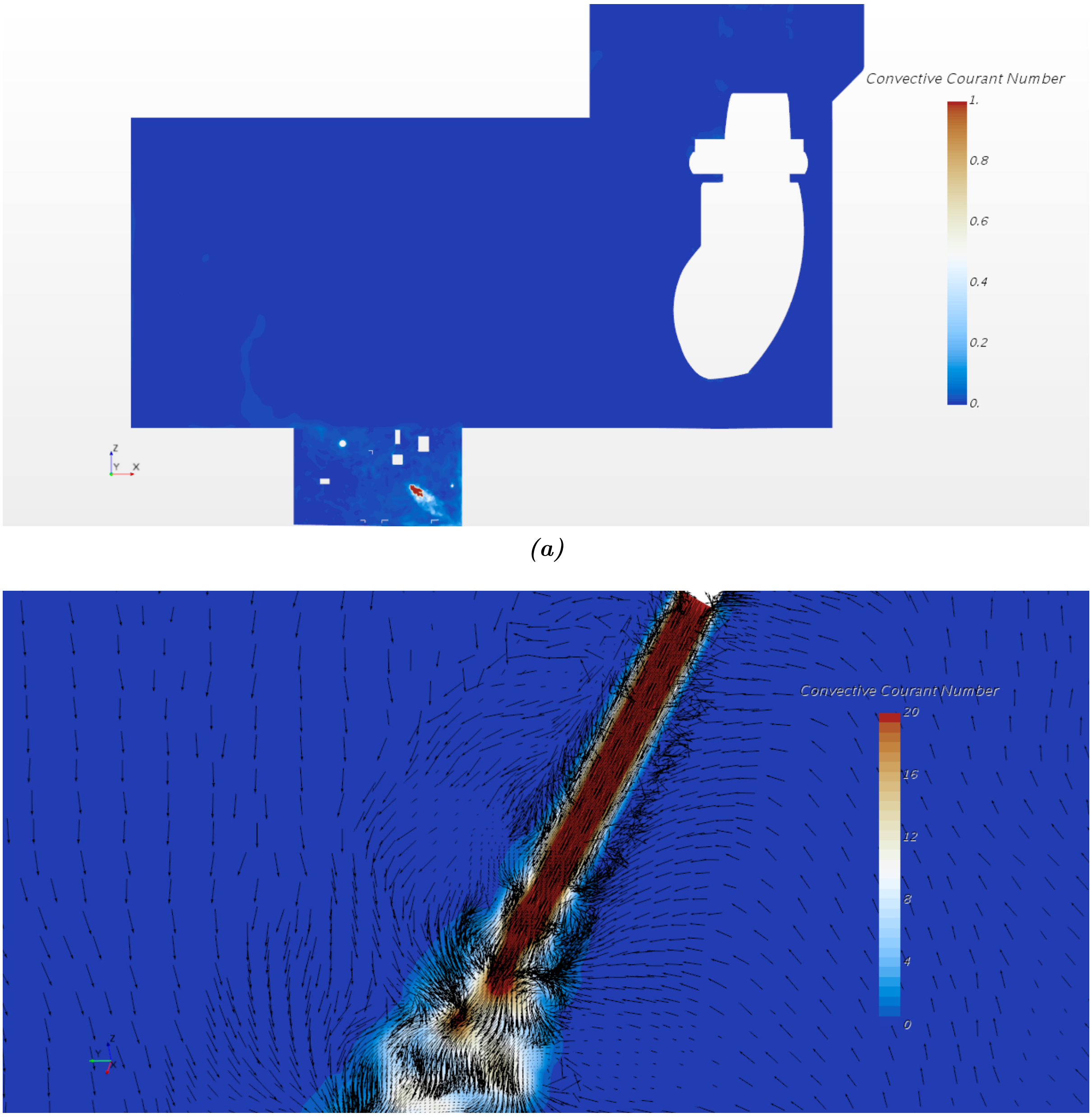

(a)

(b)

Figure 4.9: *Convective Courant number for the simulation using LES and the Sonic jet model. Near the leak velocity vectors are also shown to highlight the flow direction close to the leak.*

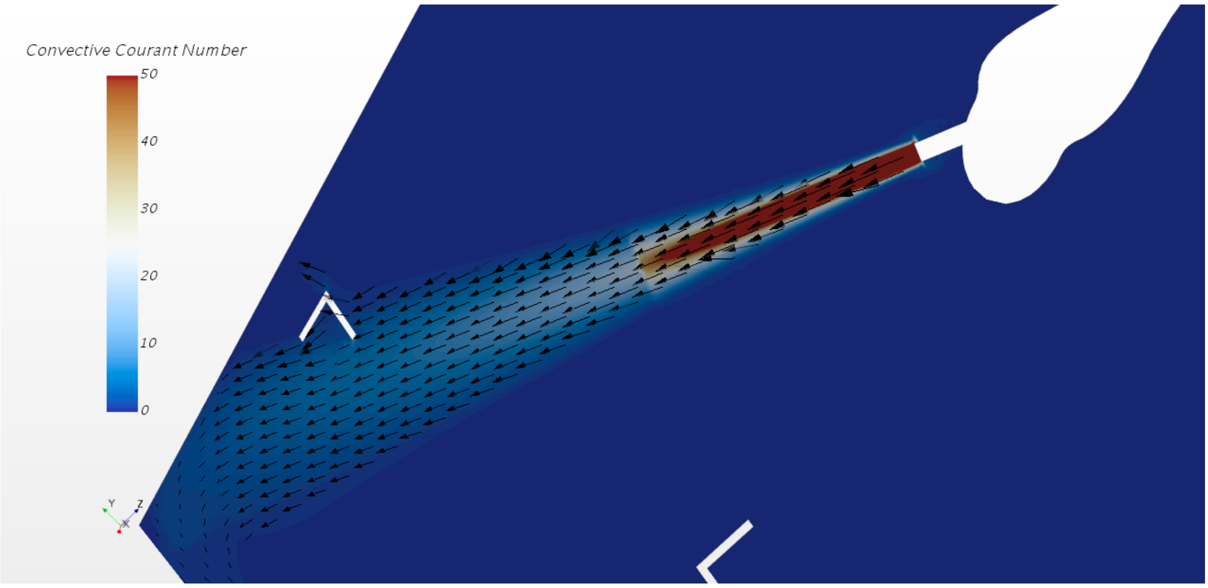

(a)

(b)

Figure 4.10: *Convective Courant number for the simulation using URANS and the Sonic jet model. Near the leak velocity vectors are also shown to highlight the flow direction close to the leak.*

4.2.3 Mesh study

To ensure that the result from the simulations do not change significantly depending on mesh size a mesh study was conducted. As seen in table 4.3. The initial mesh had around 3.5 million cells, this mesh was refined with refinement being focused in the fuel box region where the leak was implemented as this is the area of main interest and high flow gradients occur there. The entire fuel box area cell spacing was reduced from 25 mm to 15 mm and further refinement was added to the area were the leak occurs with spacing from 10 to 5 mm resulting in a refined mesh with a cell count of approximately 4.6 million cells.

Mesh study				
	Base URANS	Fine URANS	Base LES	Fine LES
100 % LEL [m^3]	0.069	0.044	0.047	0.043

Table 4.3: *Mesh study.*

The difference in results for LES is less than 10 % and was deemed acceptable. Further mesh refinement would have been be too time consuming and for LES finding a steady value that does not change with mesh refinement can be difficult as each refinement results in more turbulence being resolved until the simulation approximates a DNS. It is noteworthy how similar the mean gas cloud volume above 100% LEL is for when LES and URANS when the fine mesh is used. The Sonic jet approach was used to model the near field of the jet. It should be noted that the mesh used might be too coarse for a pure LES, likely some of the larger anisotropic turbulent scales are modelled.

4.2.4 Modelled vs. resolved turbulence in LES

To estimate how much of the turbulence is resolved in a LES simulation, the ratio of modelled to total turbulent kinetic can be used [6].

The modelled turbulent kinetic energy can be calculated from

$$k_{SGS} = C_t \frac{\mu_t}{\rho} S_{ij} \tag{4.1}$$

where C_t is a model coefficient with the value of 3.5 in STAR-CCM+ and S_{ij} is the tensor for mean strain rate.

Resolved kinetic energy, k_{RES} can be calculated as [8]

$$k_{RES} = \frac{1}{2}(\langle v_1'^2 \rangle + \langle v_2'^2 \rangle + \langle v_3'^2 \rangle) \tag{4.2}$$

Figure 4.11 shows the ratio $\frac{k_{SGS}}{k_{tot}}$ where $k_{tot} = k_{SGS} + k_{RES}$. It seems like a large portion of the turbulence was successfully resolved instead of modelled as the modelled k_{sgs} seem to consist of around 5-25% of the total turbulent kinetic energy.

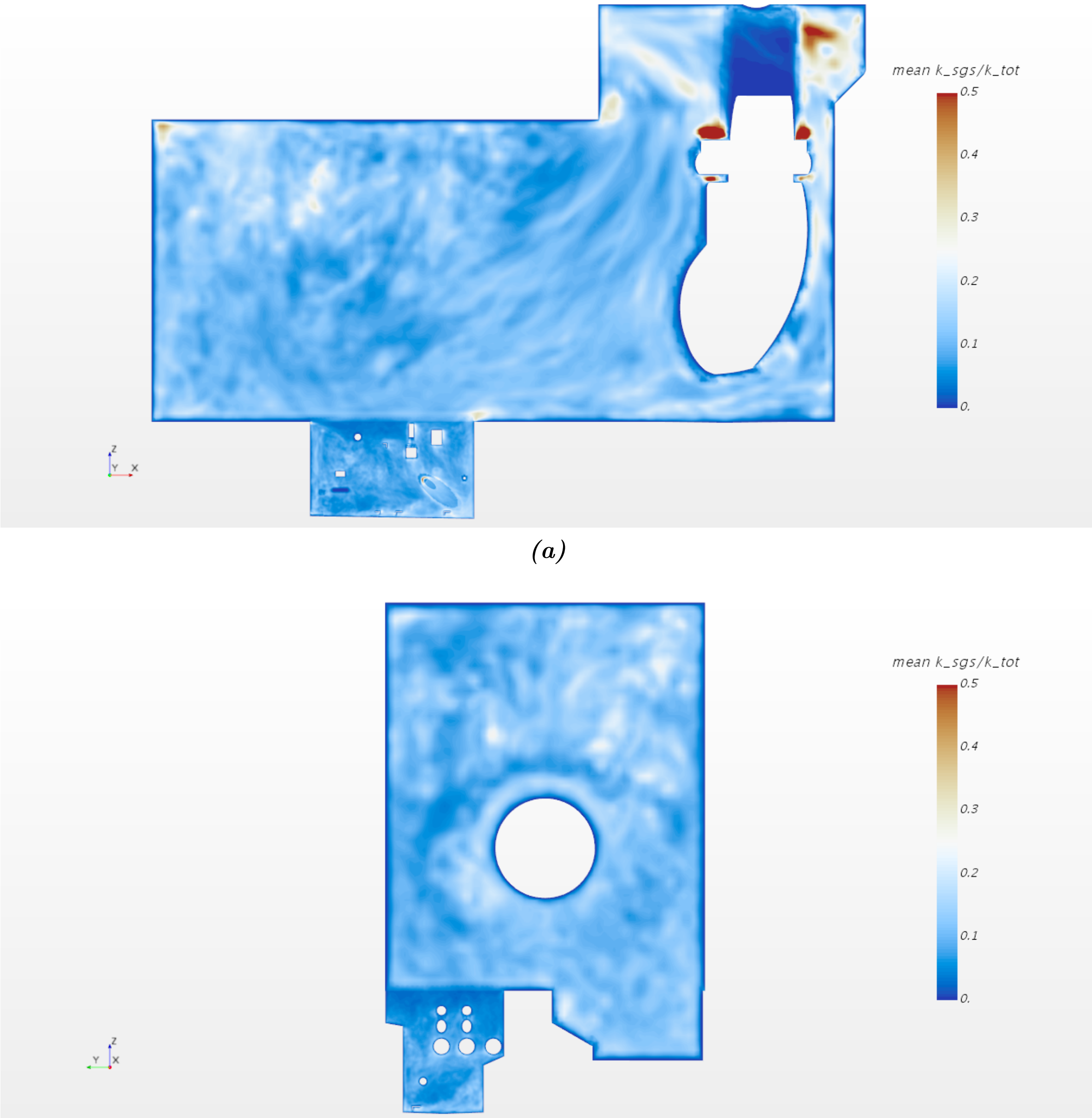

(a)

(b)

Figure 4.11: *Ratio of modelled and total turbulent kinetic energy at two different planes for the simulation using LES and Sonic jet model. Note that the areas where walls exist also appear as white.*

4.2.5 Comparison of computational resources needed

Table 4.4 shows time step, sampling time and CPU (h)/physical second. It seems that LES simulations are more demanding and also that using the Adiabatic expansion submodel increases CPU simulation time per physical second compared to using the Sonic jet submodel.

		Simulation time		
		Time step (s)	Sampling Time (s)	CPU (h)/phys. second
URANS	Sonic jet	$2 * 10^{-4}$	50	460
URANS	Adiabatic expansion	$1 * 10^{-4}$	37	1500
LES	Sonic jet	$5 * 10^{-5}$	10	2360
LES	Adiabatic expansion	$5 * 10^{-5}$	15	3700

Table 4.4: *Computational requirements when using different nozzle submodels and methods to simulate turbulence.*

4.3 Results from GT-enclosure simulations without leak

Figure 4.12 shows the velocity magnitude at a $x - z$ plane and Figure 4.13 a $y - z$ plane below the ventilation inlet. The simulation does not reach a convergent solution when using steady RANS as the flow field changed significantly with increased iterations and the residuals would not decrease to a low value.

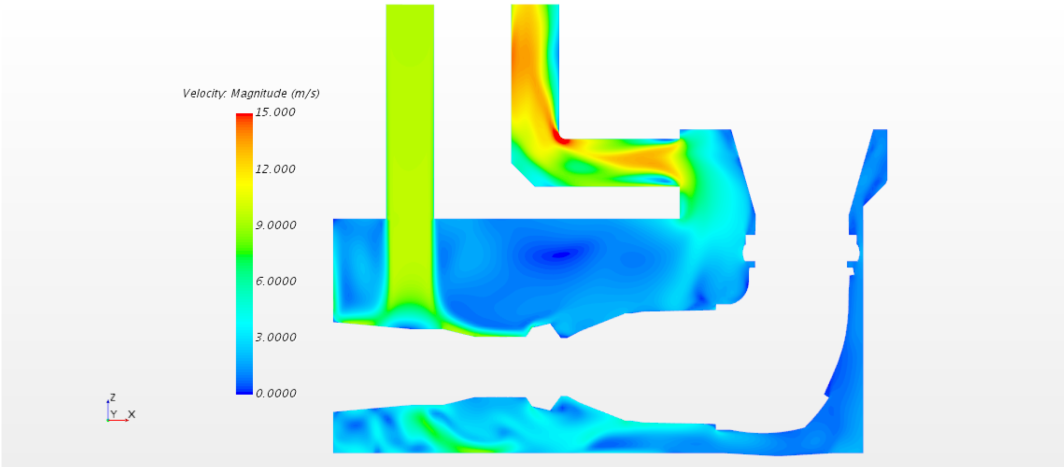

(a)

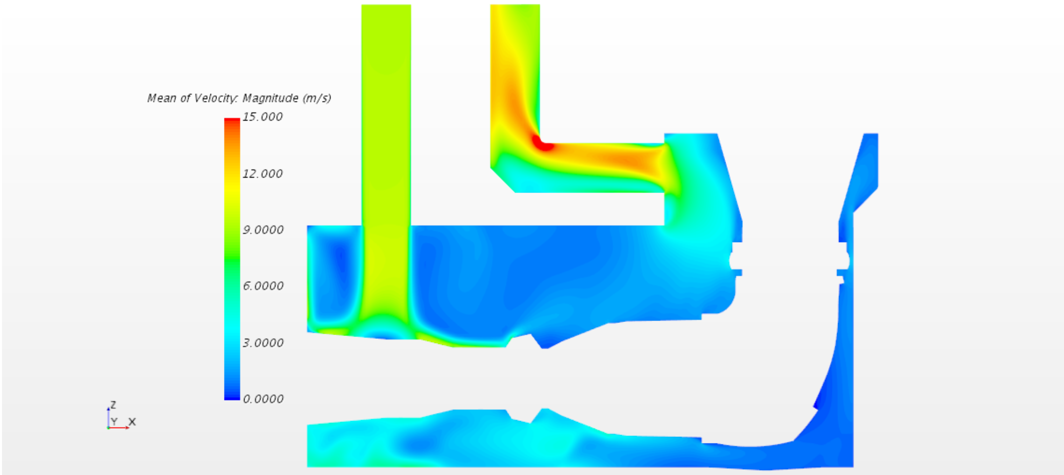

(b)

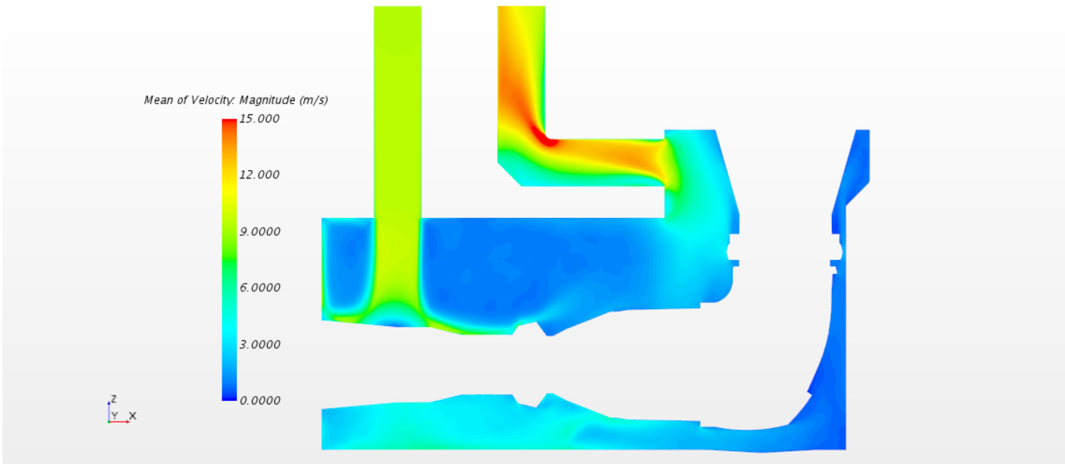

(c)

Figure 4.12: *Mean velocity magnitude distribution with cut-off at 15 m/s. Results are with a) RANS, b) URANS and c) LES models used.*

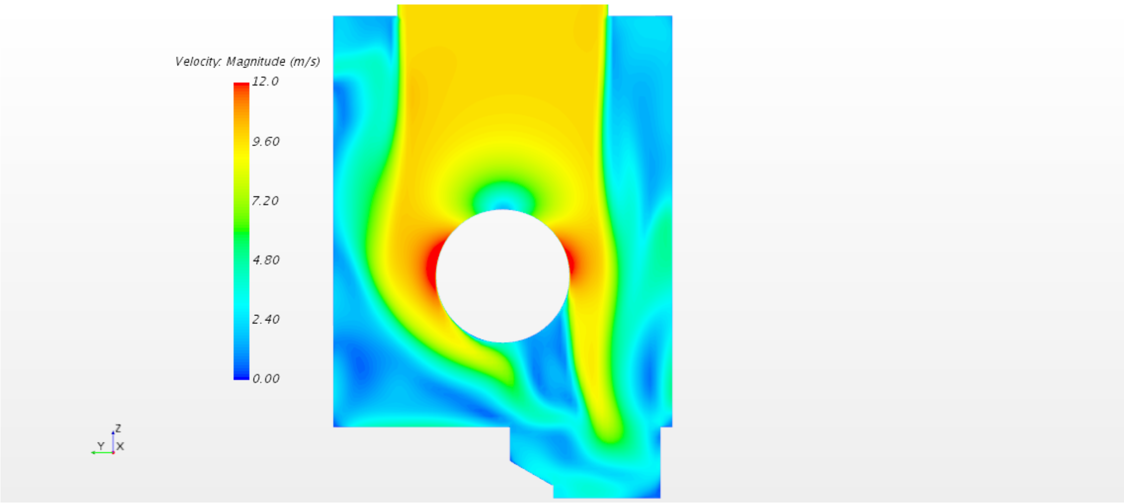

(a)

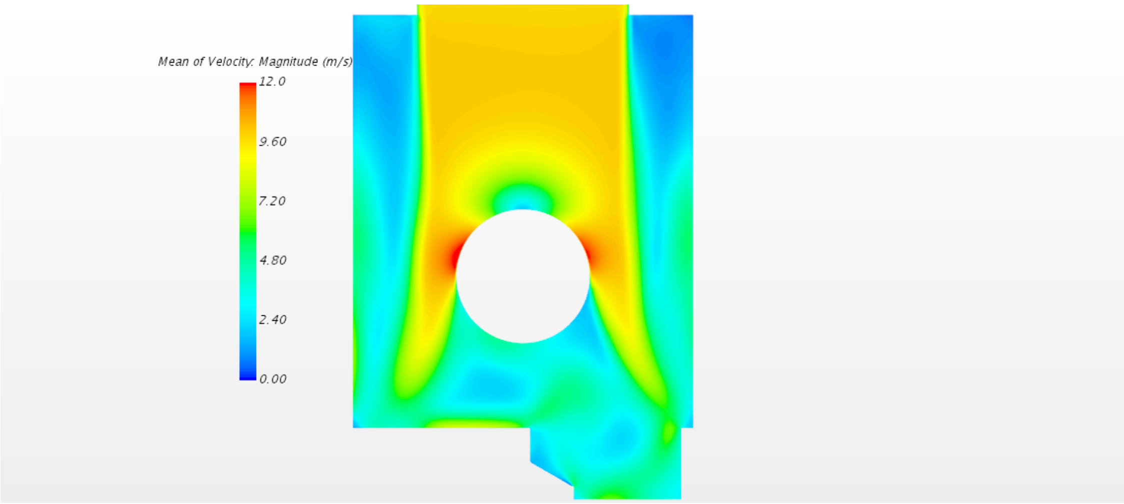

(b)

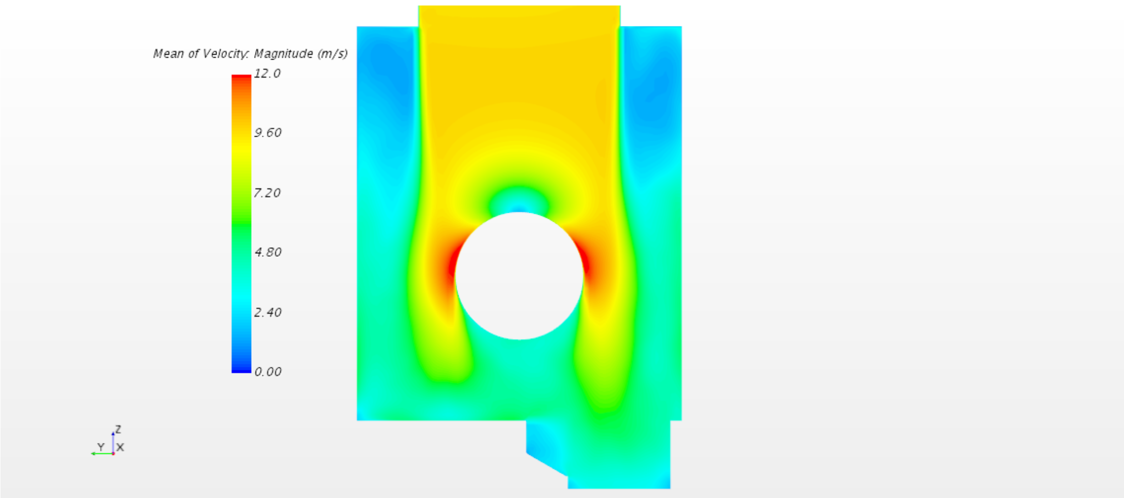

(c)

Figure 4.13: *Mean velocity magnitude distribution with cut-off at 12 m/s. Results are with a) RANS, b) URANS and c) LES models used.*

Figure 4.14 shows the velocity magnitude distribution in the fuel box. It can be seen that the flow there is rather stagnant.

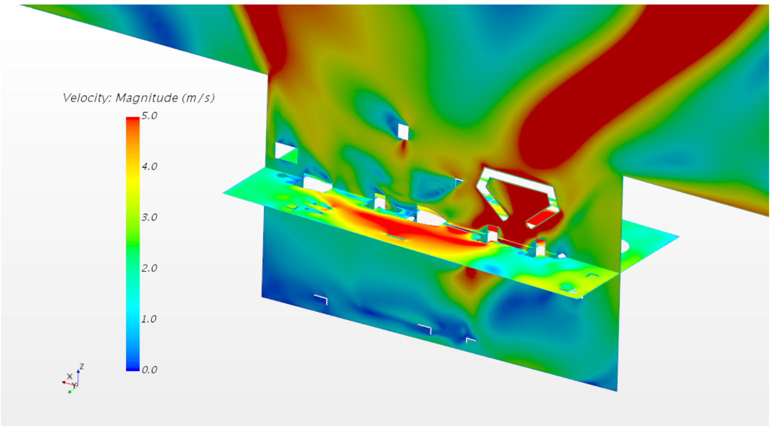

(a)

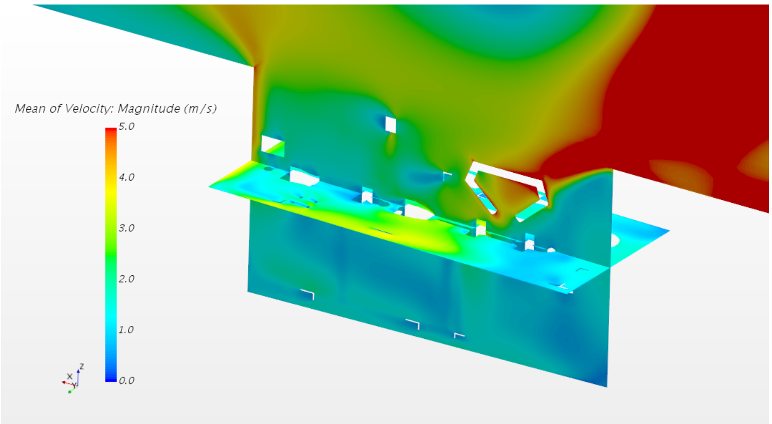

(b)

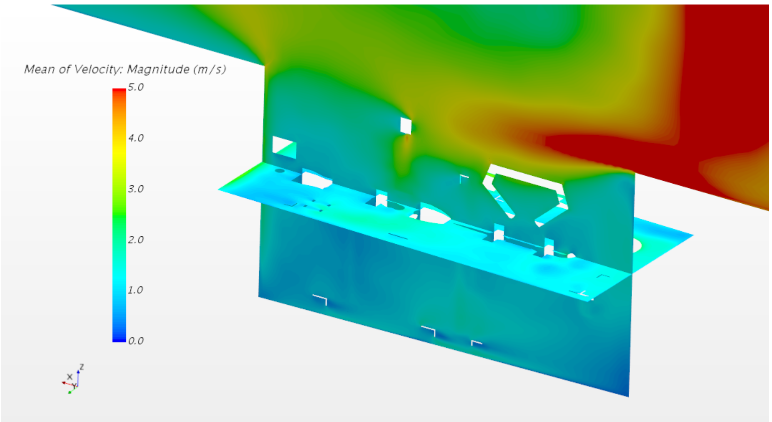

(c)

Figure 4.14: *Mean velocity magnitude distribution with cut-off at 5 m/s. Results are with a) RANS, b) URANS and c) LES models used.*

4.4 Results for GT-enclosure simulations with a leak implemented

As RANS showed poor results when simulating the flow without any leak implemented, only URANS and LES are considered for simulations where the leak is implemented.

Table 4.5 shows the results for the explosive gas cloud volume with a LEL $\geq 100\%$. Some results are given in a range of values due to the inability to find a steady mean value. That steady values were easier found using LES and the Adiabatic expansion model can maybe be understood by looking at figures for the instantaneous and mean explosive gas clouds in figures 4.16 and 4.17 respectively. The explosive gas cloud distribution when the Sonic jet submodel is used presents a much more unstable flow situation.

The resulting explosive gas cloud size differs depending on which submodel is used, this result is consistent with the results from only modelling the leak jet on its own. Using LES has a large impact on the size of the cloud when the Adiabatic expansion submodel is used, as also seen in Figure 4.17, but not when the Sonic jet submodel is used as seen in Figure 4.18. This could be due to that the jet produced using the Adiabatic expansion submodel is of higher velocity magnitude which can be seen in Figure 4.15 and Figure 4.17. The higher jet velocity magnitude could improve mixing by increased shear stress between the jet and surrounding fluid which in turn increases the corresponding interfacial area and this promotes mixing [24]. The lower velocity leak from when the Sonic jet submodel is used results in a large region of almost stagnant gas along the sides and bottom of the gas fuel box and for this low speed gas, perhaps the effect of using LES to better capture the turbulent mixing is less significant.

Explosive gas cloud size from GT-enclosure simulations $[m^3]$		
	Sonic jet model	Adiabatic expansion model
URANS	0.037-0.049	0.010-0.023
LES	0.041-0.052	0.004

Table 4.5: *Comparisons of gas cloud size results using URANS and LES methods.The results are time-averaged mean quantities.*

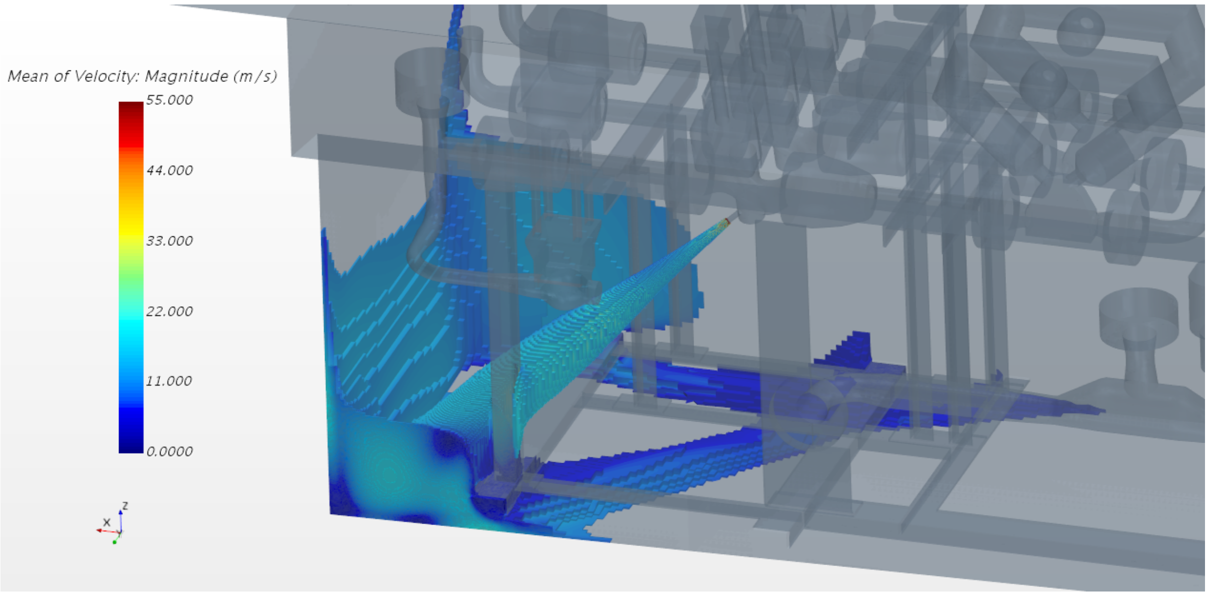

(a)

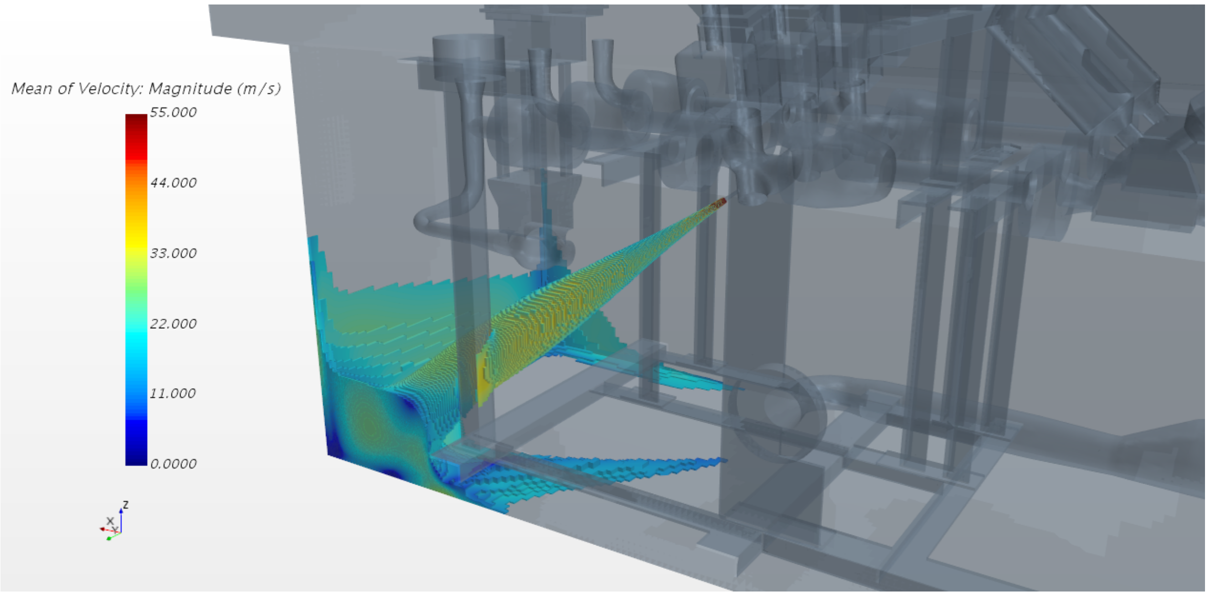

(b)

Figure 4.15: *Cells with higher than 100% LEL highlighted and corresponding mean velocity magnitude when using URANS and a) the Sonic jet submodel and b) the Adiabatic expansion submodel to model the leak.*

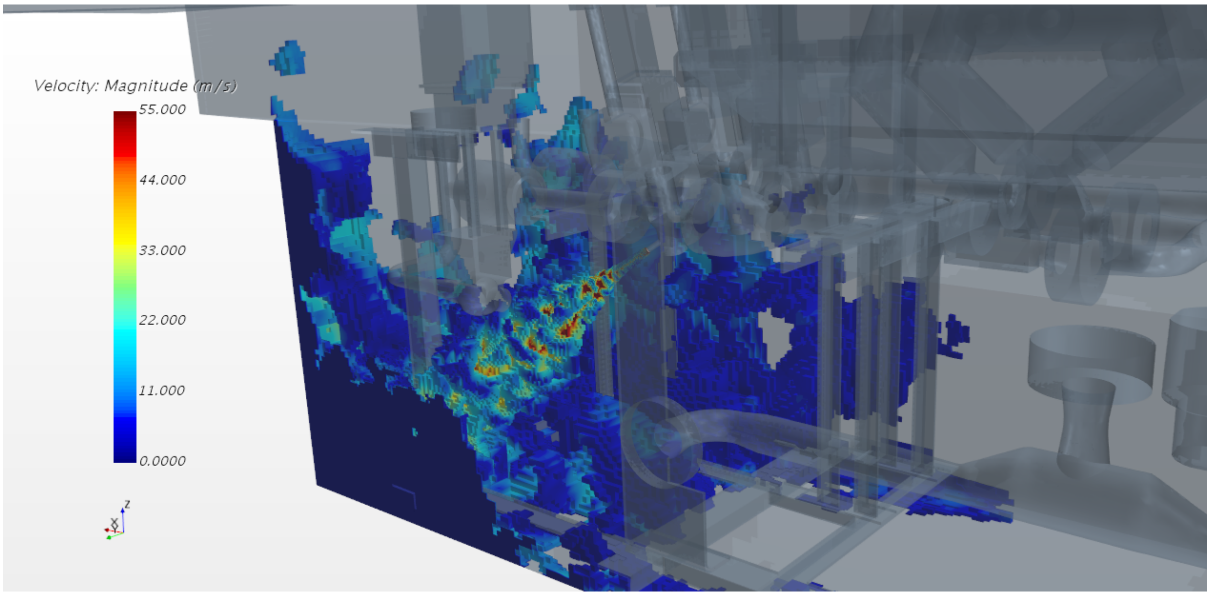

(a)

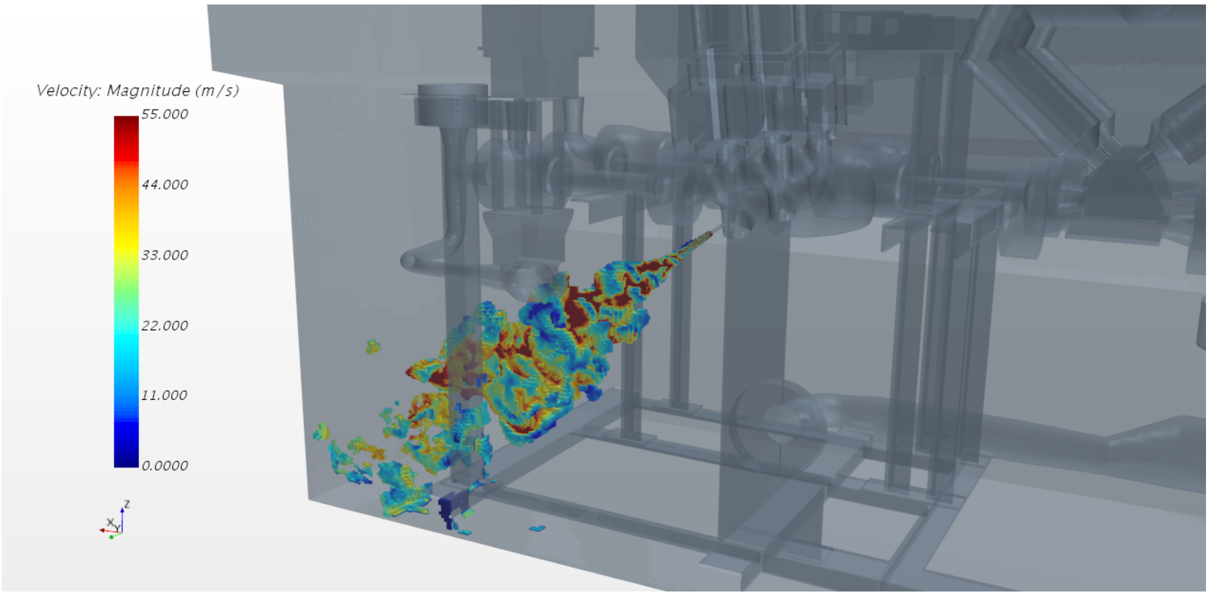

(b)

Figure 4.16: *Cells with higher than 100% LEL highlighted and corresponding instantaneous velocity magnitude when using LES and a) the Sonic jet submodel and b) the Adiabatic expansion submodel to model the leak.*

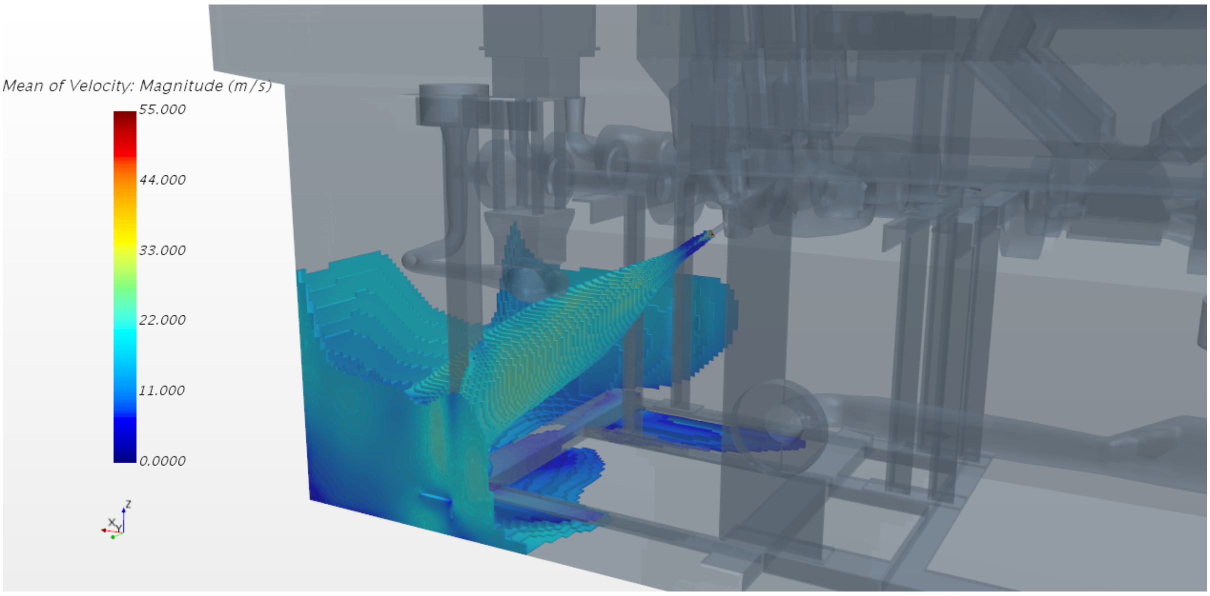

(a)

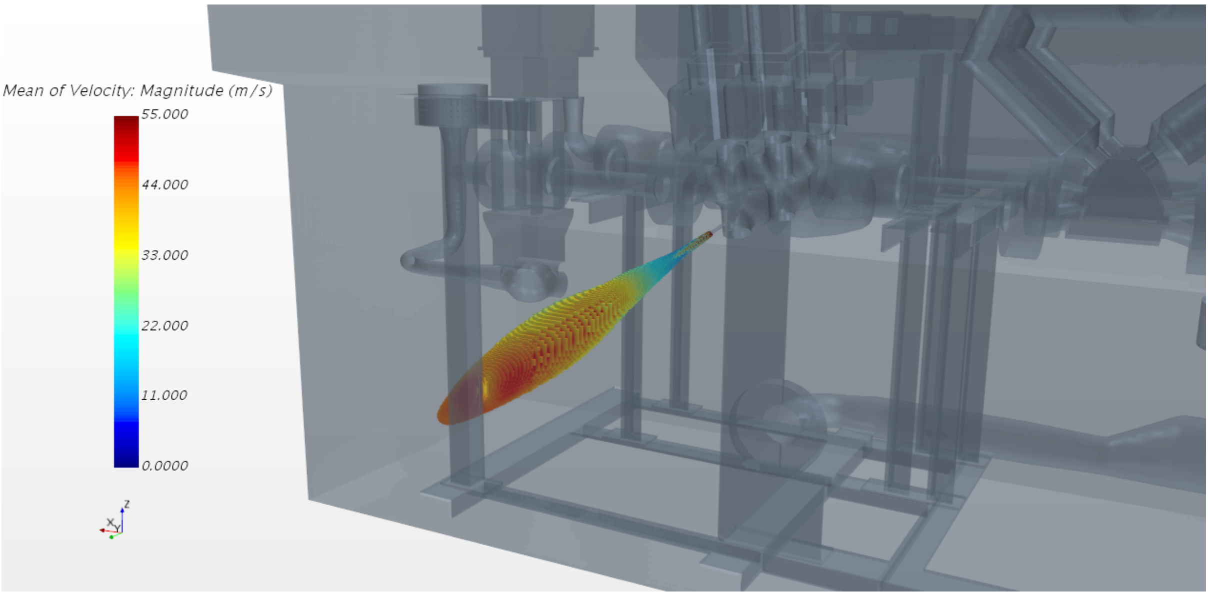

(b)

Figure 4.17: *Cells with higher mean values than 100% LEL highlighted and corresponding mean velocity magnitude when using LES and a) the Sonic jet submodel and b) the Adiabatic expansion submodel to model the leak.*

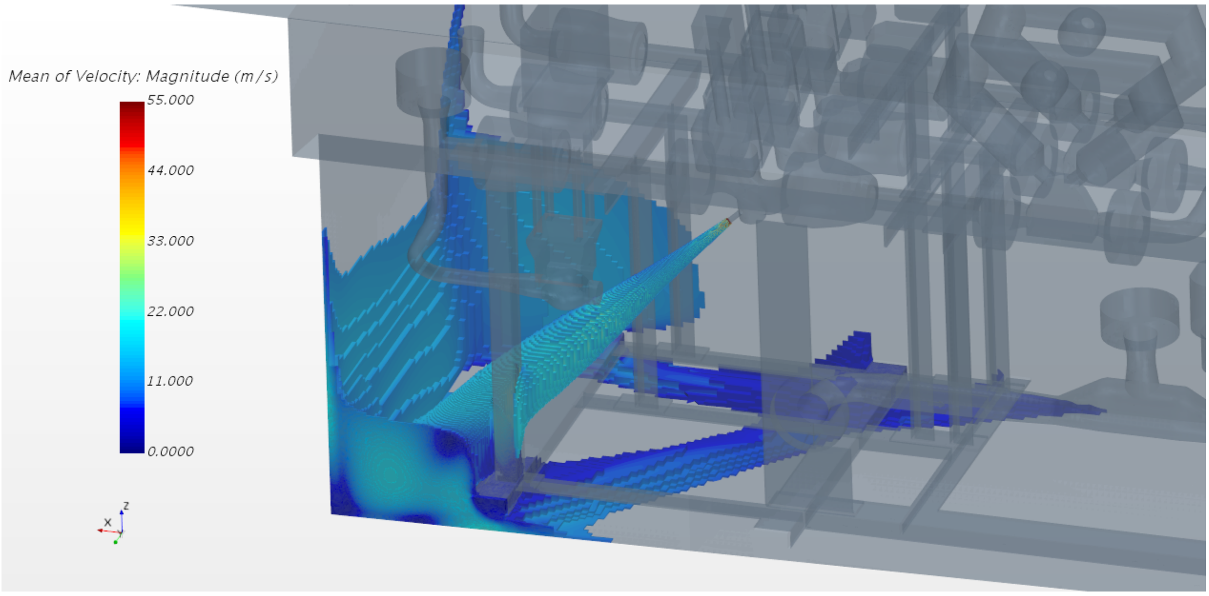

(a)

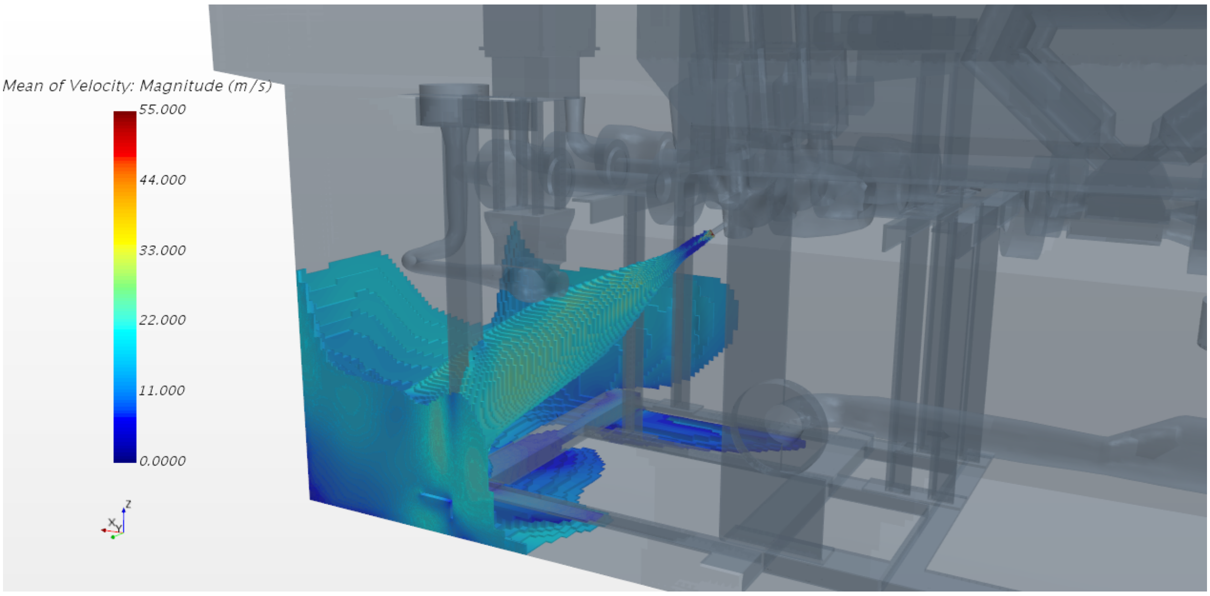

(b)

Figure 4.18: *Cells with higher mean values than 100% LEL highlighted and corresponding mean velocity magnitude when using the Sonic jet submodel with a) URANS and b) LES.*

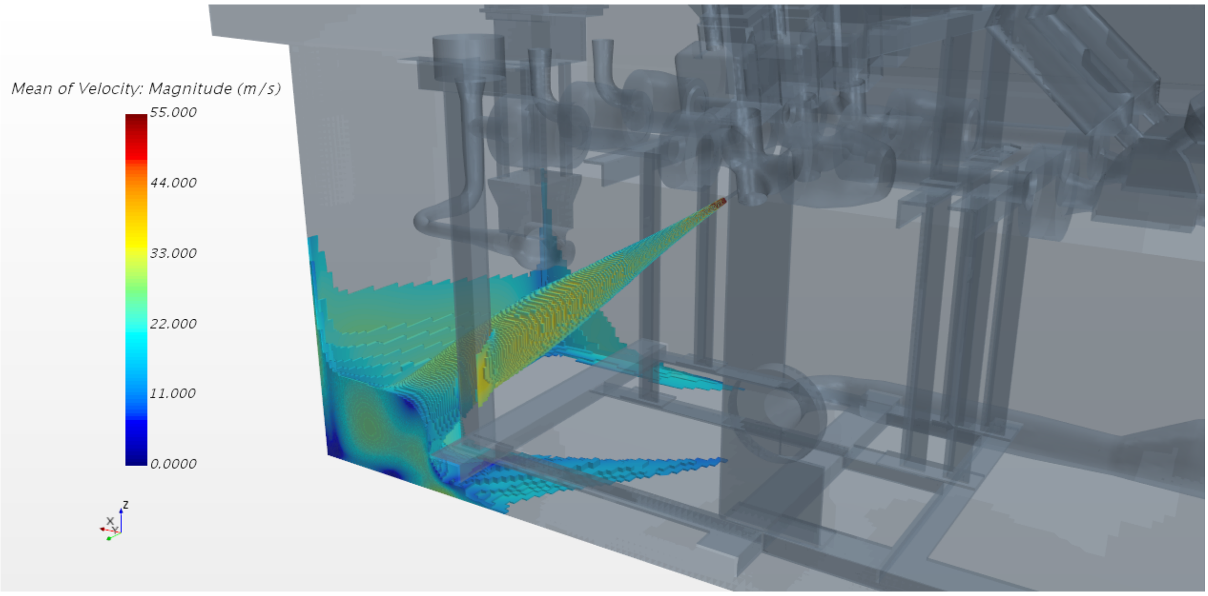

(a)

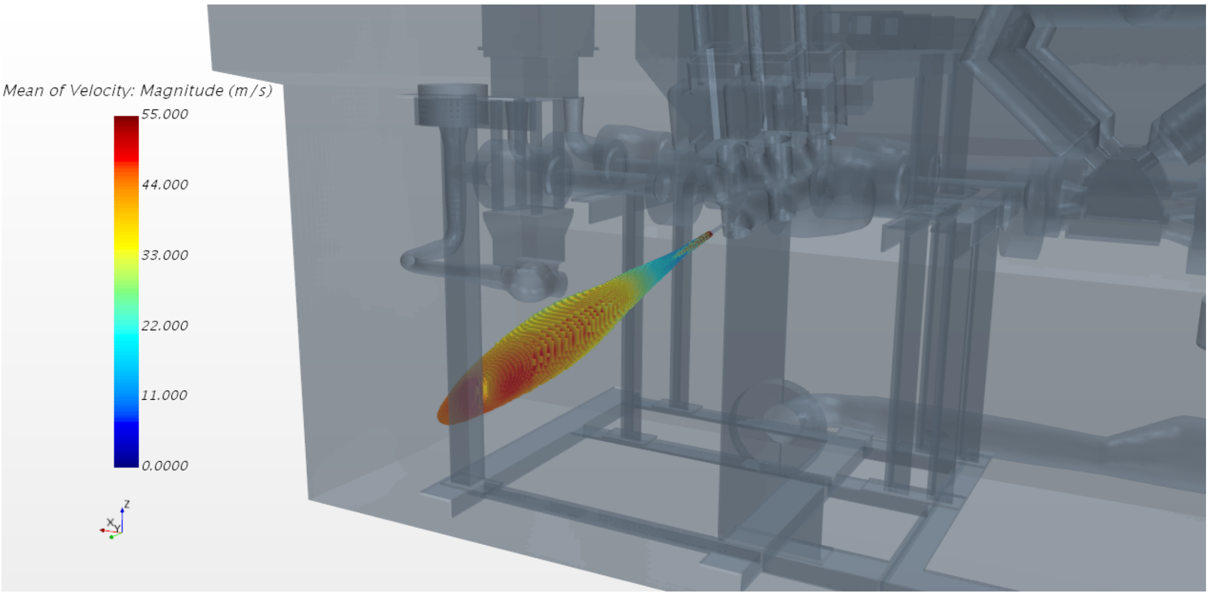

(b)

Figure 4.19: *Cells with higher mean values than 100% LEL highlighted and corresponding mean velocity magnitude when using the Adiabatic expansion submodel with a) URANS and b) LES.*

5

Conclusions and future work

This work can be divided in two main parts. One concerned with modelling the leak itself and one concerned with comparing the build-up of a explosive gas cloud using URANS and LES turbulence modelling.

Regarding the shape of the leak orifice, it appears that a round hole is a conservative choice as it produces the largest 100 % LEL gas cloud volume. This is consistent with similar results that other authors have found as discussed in Section 1.1.

It appears that all submodels tested except for the Adiabatic expansion approach overestimates the 100 % LEL gas cloud volume with more than a factor 2. The cause is for the Sonic jet and the Improved pseudo-diameter models suspected to be a result of the assumption of no prior air entrainment. The air entrainment in the real jet before the placement of the equivalent jet for these models appears to have diluted the leaked gas concentration to a non-negligible extent.

The effect of this assumption is less pronounced when using the Adiabatic expansion approach, which could be because it results in a jet cross sectional area which more closely represents a stage where the real jet has not yet undergone considerable mixing with the ambient air.

The Mach disk approach is designed to produce a jet equivalent to that of one just after a Mach disk but when comparing with results from the simulation of the real jet, it is seen that this is likely not the case.

An empirical adjustment to the Sonic jet model which takes into consideration prior air mixing and non-constant mass flux has been proposed using Gaussian curve fitting and the results are closer in agreement with the results from the simulation of the real jet. It should be stressed that this adjusted model is strictly empirical and needs to be validated before use for cases with other flow conditions. Future work could perhaps result in a more general submodel that takes the pre-mixing with air into account.

The second main part of this thesis focused on simulating a gas leak in a simplified GT-enclosure geometry. Two submodels for the leak were used, the Sonic jet model and the Adiabatic expansion model. URANS and LES were used to be compare how the choice of method to simulate turbulence effects the mixing and resulting explosive gas cloud.

It appears that steady RANS is not a well suited approach as a convergent, steady solution could not be reached even for the case of no leak implemented.

Comparing submodels, the difference with respect to size and distribution of the explosive gas cloud is consistent with the result of simulating only the leak jet itself. A smaller explosive gas cloud size is seen when using the Adiabatic expansion model compared to the Sonic jet model.

Comparing LES and URANS, it seems as LES, especially when using the Adiabatic expansion submodel for the leak, results in a smaller explosive gas cloud size. This result is interesting as LES is known to in a more realistic way capture the turbulent effects compared to RANS methods. This could point to RANS methods overestimating the explosive gas cloud size in this case. Why LES and URANS gave similar results when using the Sonic jet model could be because with this model a lower velocity jet is produced causing less shearing between the jet and the surrounding fluid, resulting in less effect between using RANS or LES.

As a final note it should be pointed out that this report has focused on comparing mean values. In a real gas leak situation it is of course also the instantaneous quantities that matter and so some additional level of conservatism could be needed to cover the variation in gas leak concentration. Either by using a modelling method that is known to be conservative enough, taking into account instantaneous values if using a method such as LES, or using a lower threshold than 100% LEL.

Bibliography

[1] The Hon Lord Cullen, The Public Enquiry into the Piper Alpha Disaster, Vols. 1 and 2, HMSO (CM 1310), London, 1990.

[2] K. B. M. Q. Zaman, Spreading characteristics of compressible jets from nozzles of various geometries, J. Fluid Mech, Volume 383, pages 197-228, 1999.

[3] Shishehgaran N, Paraschivoiu M, CFD based simulation of hydrogen release through elliptical orifices, International Journal of Hydrogen Energy, 2014.

[4] Plane hydrogen jets D. Makarov*, V. Molkov International Journal of Hydrogen Energy Volume 38, Issue 19, Pages 8068-8083, 2013.

[5] M. Ivings,C. Lea, H.S. Ledin, D. Pritchard, R. Santon and J. Saunders, Outstanding safety questions concerning the use of gas turbines for power generation – Summary report CM/04/09, Health Safety Laboratory, Buxton, 2004.

[6] Siemens, Simcenter STAR-CCM+ User Guide

[7] H. K. Versteeg and W. Malalasekera, An Introduction to Computational Fluid Dynamics : The Finite Volume Methods, Second edition, Pearson Education (US), Upper Saddle River, United States, 2007.

[8] L. Davidsson, Fluid mechanics, turbulent flow and turbulence modeling, Division of Fluid Dynamics Department of Applied Mechanics, Chalmers University of Technology, Göteborg 2019.

[9] B. Andersson, R. Andersson, L. Håkansson, M. Mortensen, R. Sudiyo and B. van Wachen, Computational Fluid Dynamics for Engineers, 12th edition, Cambridge University Press, Gothenburg 2016.

[10] F. P. Incropera, D. P. Dewitt, T.L. Bergman and A.S. Lavine, Principles of heat and mass transfer, Global edition, John Wiley Sons Inc, New York, United States, 2017.

[11] J. D. Anderson, Modern compressible flow, Third Edition, McGraw-Hill Education, 2002.

[12] W.J. Beek, J.W.Van Heuven, K.M.K. Muttzall, Transport Phenomena, Second Edition, John Wiley Sons and Sons LTD, United Kingdom, 1999.

[13] R. W. Miller, Flow Measurement Engineering Handbook, Third Edition, McGraw-Hill Education, 1996

[14] C.J.H. van den Bosch, R.A.P.M. Weterings,Methods for the calculation of physical effects –due to releases of hazardous materials (liquids and gases), 3rd edition, 2005.

[15] E. Franquet, Free underexpanded jets in a quiescent medium: A review, Progress in Aerospace Sciences Volume 77, pages 25-53, 2015.

[16] Mohanta, Prasanta Sridhar, B.T.N. (2016). Study of decay characteristics of rectangular and elliptical supersonic jets. Thermal Science, page 214, 2016.

[17] M. J. Assael, K. E. Kakosimos, Fires, explosions and toxic gas dispersions: Effects calculations and risk analysis, First edition, CRC Press, 2010.

[18] S.E. Gant, M.J. Ivings, CFD Modelling of Low Pressure Jets for Area Classification, Health Safety Laboratory, Buxton (UK), 2005.

[19] A. Velikorodny, Numerical study of the near-field of highly underexpanded turbulent gas jets, International Journal of Hydrogen Energy Volume 37, Issue 22, November 2012, Pages 17390-17399, 2012.

[20] F. Hempert et al., Simulation of real gas effects in supersonic methane jets using a tabulated equation of state with a discontinuous Galerkin spectral elementmethod, Computer Fluids, Volume 145, pages 167-179, 2017.

[21] J. Xiao, J.R. Travis, W. Breitung, Hydrogen release from a high pressure gaseous hydrogen reservoir in case if a small leak, International Journal of Hydrogen Energy, Volume 36, pages 2545-2554, 2011.

[22] Nicoud, F. and Ducros, F., 1999. "Subgrid-Scale Stress Modelling Based on the Square of the Velocity Gradient Tensor," Flow, Turbulence and Combustion, 62, pp. 183-200

[23] J. D. Anderson, Computational Fluid Dynamics: The Basics with Applications ,International Edition, McGraw-Hill Education, 1995.

[24] Mixing: Chaos and Turbulence, H. Chaté, E. Villermaux, J.-M. Chomaz, Springer Science Business Media, 2012

A

Appendix

A.1 Choked mass flow through orifice

Continuity between a upstream station 1 and throat section t gives

$$\dot{m}_1 = A_t \rho_t \overline{V}_t \tag{A.1}$$

Because of choked flow at the throat, sonic conditions exists there and the velocity can be related to the sonic velocity a

$$\overline{V}_t = a. \tag{A.2}$$

and from (2.35)

$$a = \sqrt{\left(\frac{\gamma p}{\rho}\right)_s}. \tag{A.3}$$

Using (A.3) in (A.1) and introducing the coefficient of discharge C gives

$$\dot{m} = C A_t \sqrt{\gamma P_t \rho_t} \tag{A.4}$$

Isentropic relations at stagnation conditions

$$\left(\frac{p_t}{p1}\right)_0 = \left(\frac{2}{\gamma+1}\right)^{\gamma/(\gamma-1)} \tag{A.5}$$

and

$$\left(\frac{\rho_t}{\rho_1}\right)_0 = \left(\frac{2}{\gamma+1}\right)^{1/(\gamma-1)} \tag{A.6}$$

are substituted into (A.4) resulting in

$$\dot{m} = C A_t \left[\gamma \left(\frac{2}{\gamma+1}\right)^{\frac{\gamma+1}{\gamma-1}}\right]^{1/2} \sqrt{(P_0 \rho_0)_1} \tag{A.7}$$

A.2 Radial velocity for different orifice shapes using the Sonic jet model

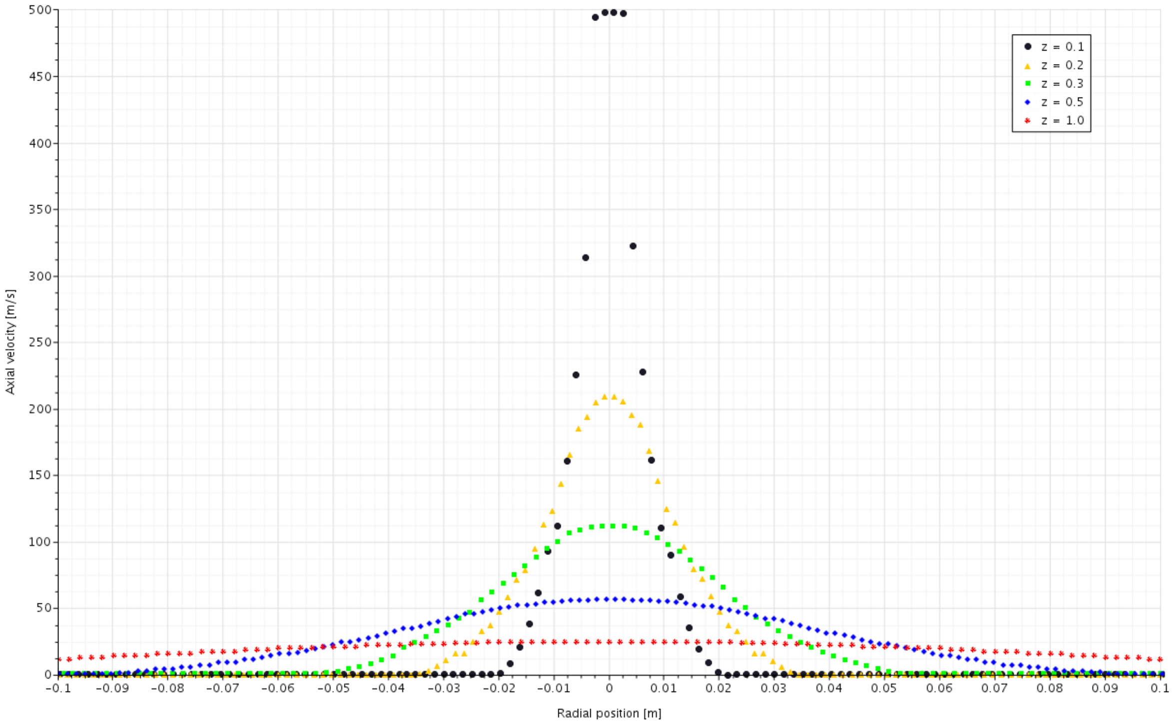
Axial velocity [m/s]
Radial position [m]
z = 0.1
z = 0.2
z = 0.3
z = 0.5
z = 1.0

(a)

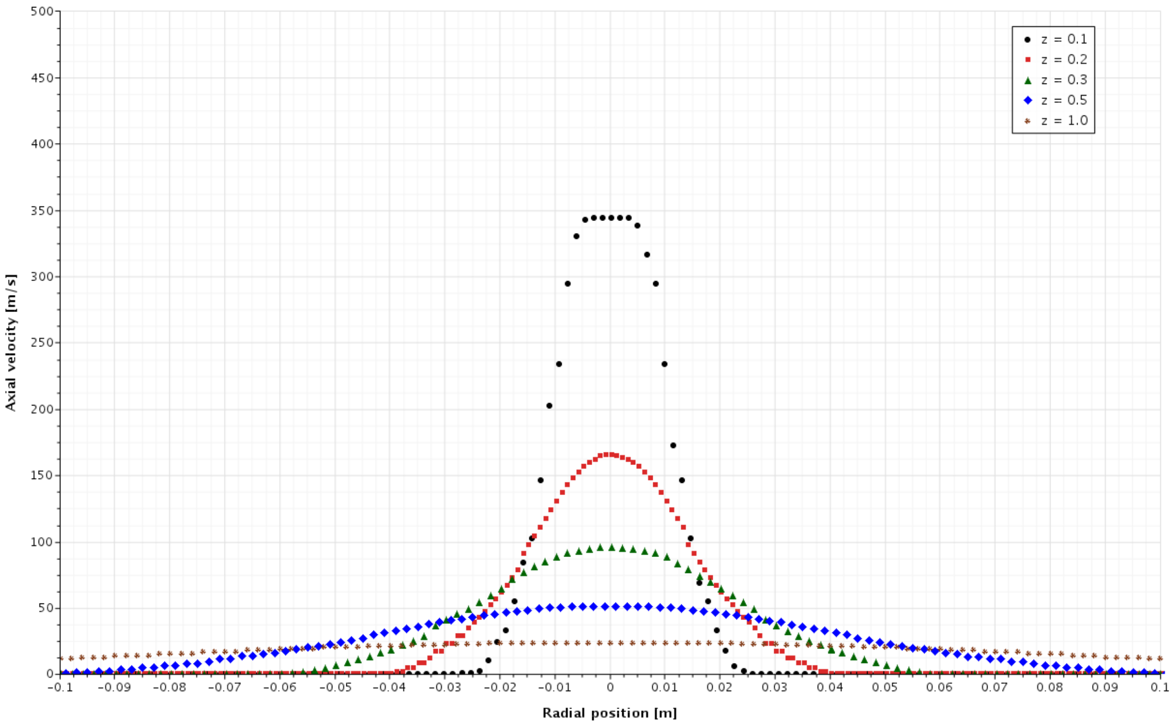
Axial velocity [m/s]
Radial position [m]
z = 0.1
z = 0.2
z = 0.3
z = 0.5
z = 1.0

(b)

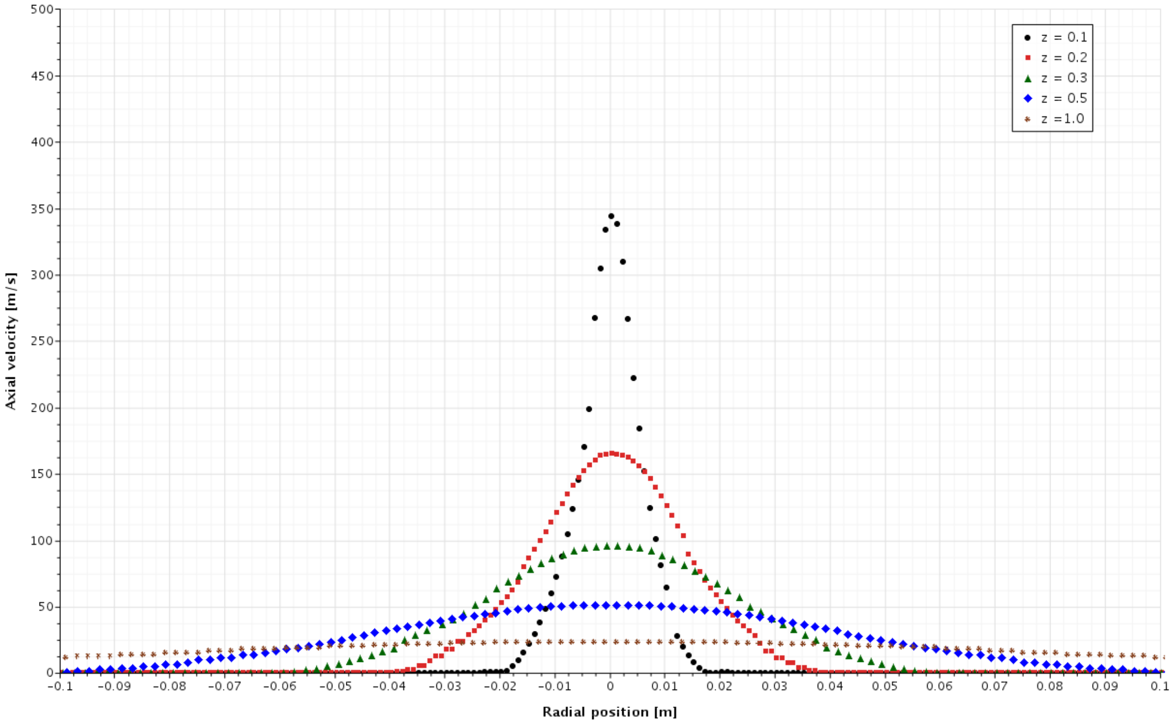
z = 0.1
z = 0.2
z = 0.3
z = 0.5
z =1.0
Axial velocity [m/s]
Radial position [m]

(c)

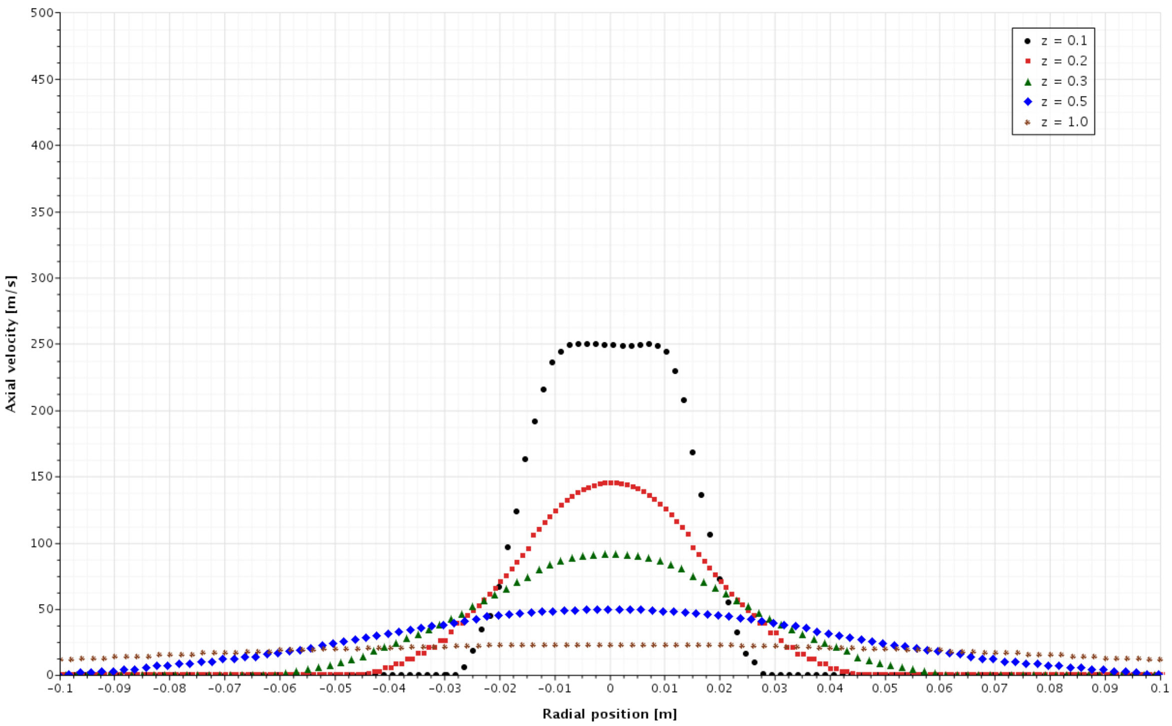
z = 0.1
z = 0.2
z = 0.3
z = 0.5
z = 1.0
Axial velocity [m/s]
Radial position [m]

(d)

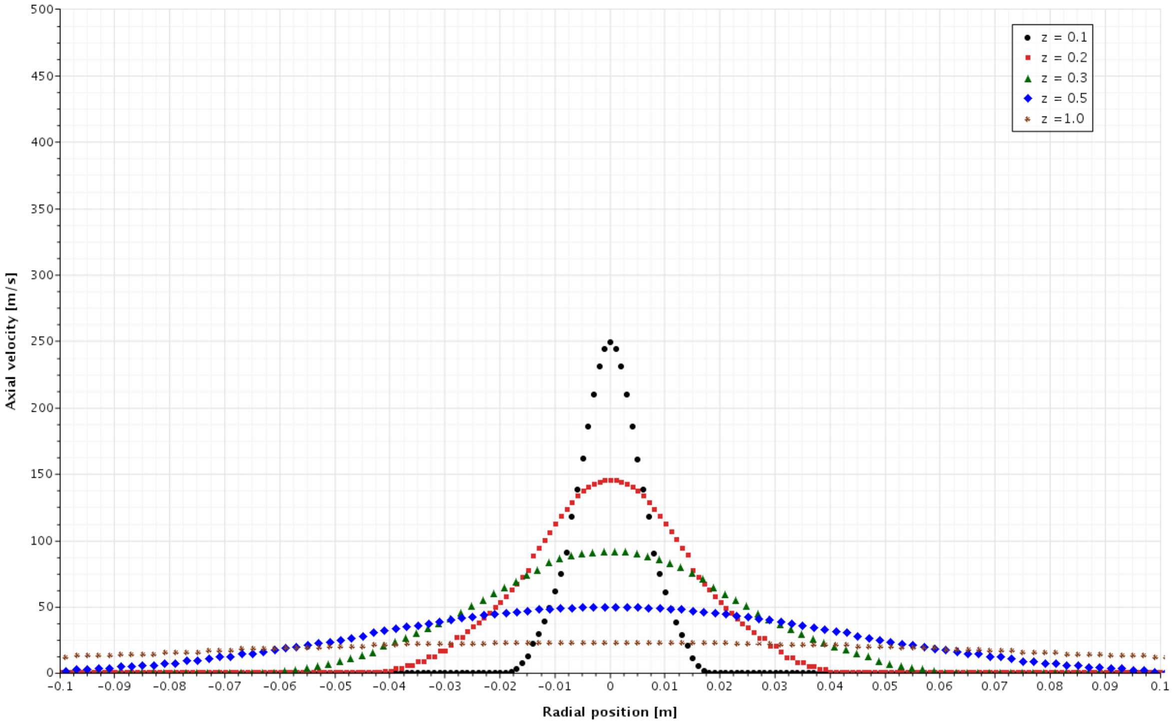

Axial velocity [m/s]
Radial position [m]
z = 0.1
z = 0.2
z = 0.3
z = 0.5
z =1.0

(e)

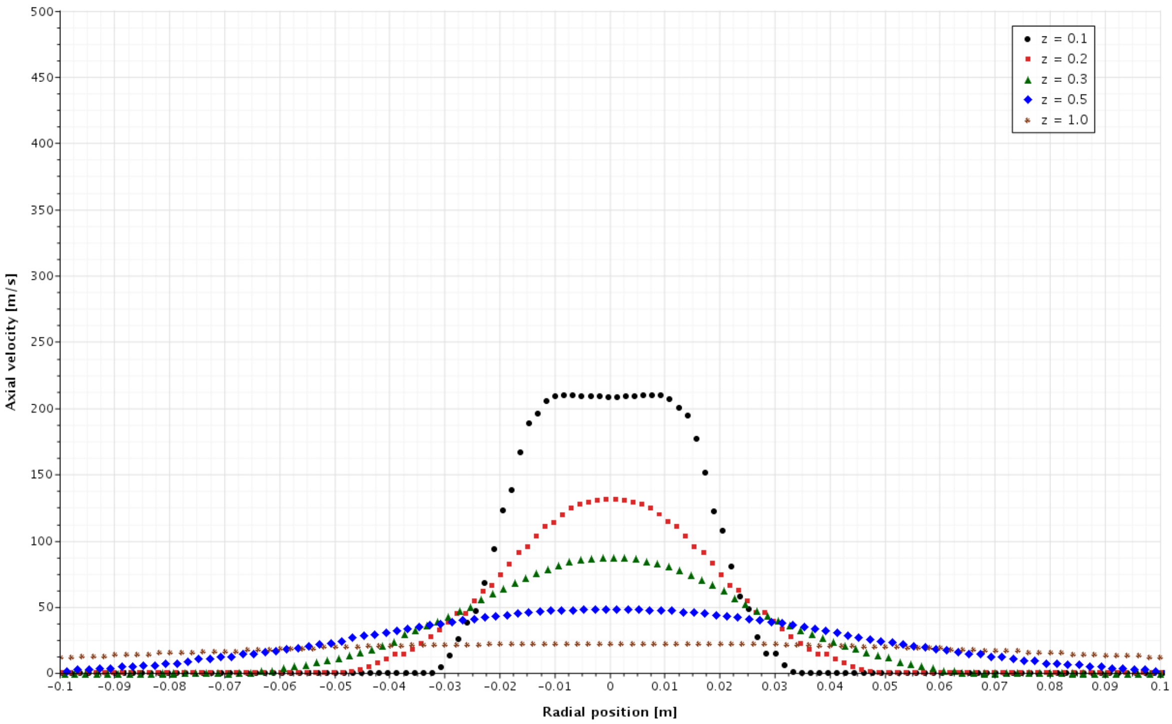

Axial velocity [m/s]
Radial position [m]
z = 0.1
z = 0.2
z = 0.3
z = 0.5
z = 1.0

(f)

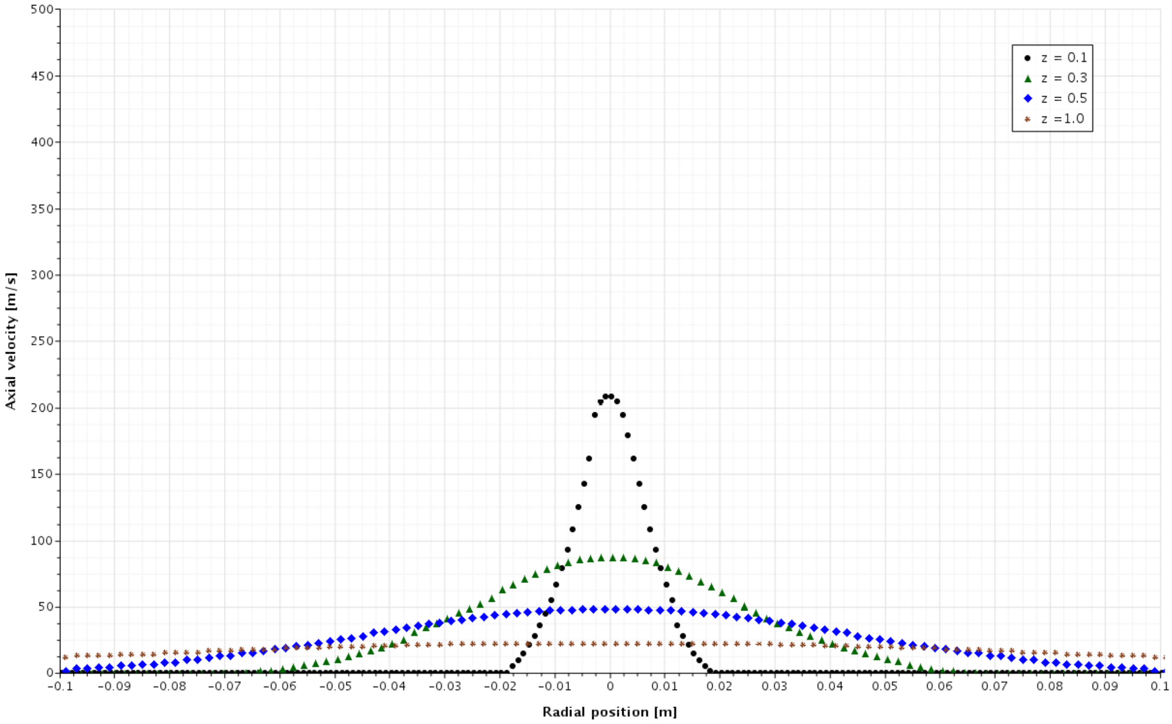

Axial velocity [m/s]
Radial position [m]
z = 0.1
z = 0.3
z = 0.5
z =1.0

(g)

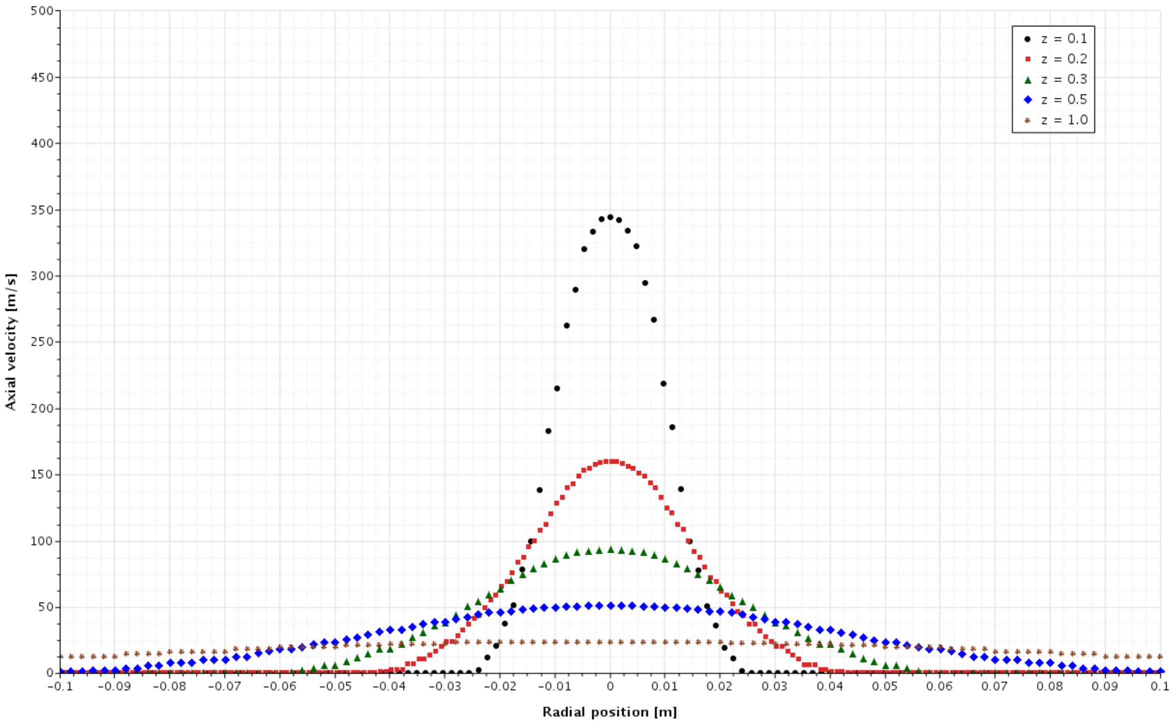

Axial velocity [m/s]
Radial position [m]
z = 0.1
z = 0.2
z = 0.3
z = 0.5
z = 1.0

(h)

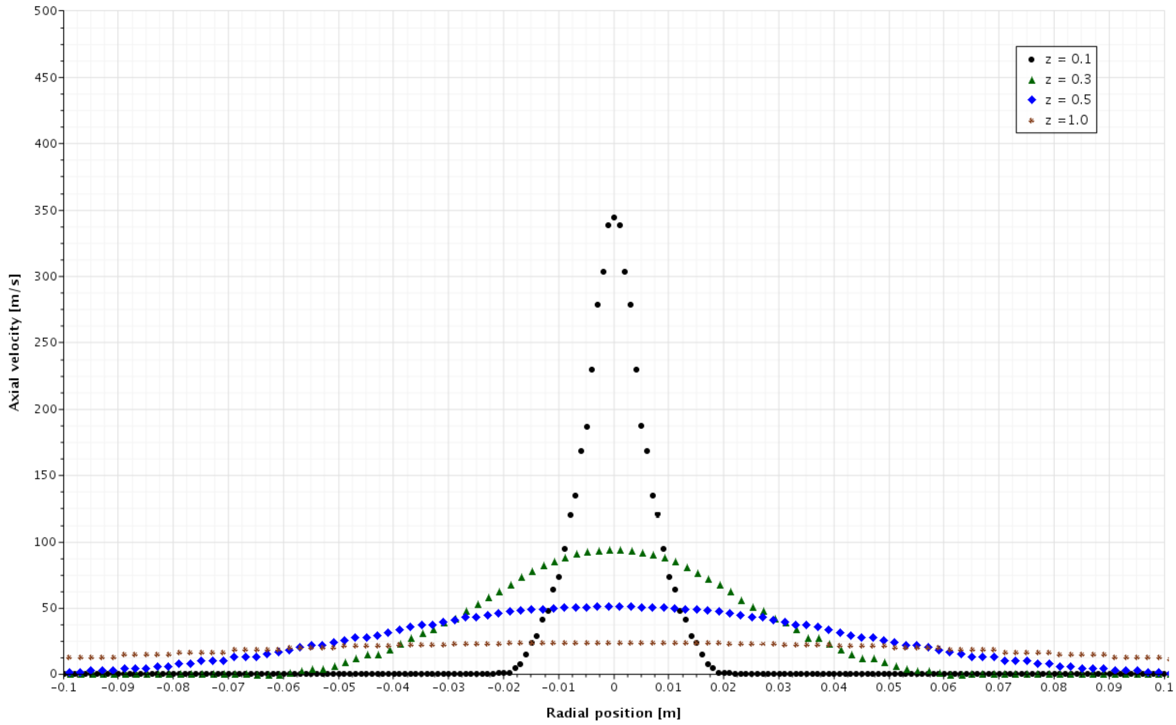

z = 0.1
z = 0.3
z = 0.5
z =1.0
Axial velocity [m/s]
Radial position [m]

(i)

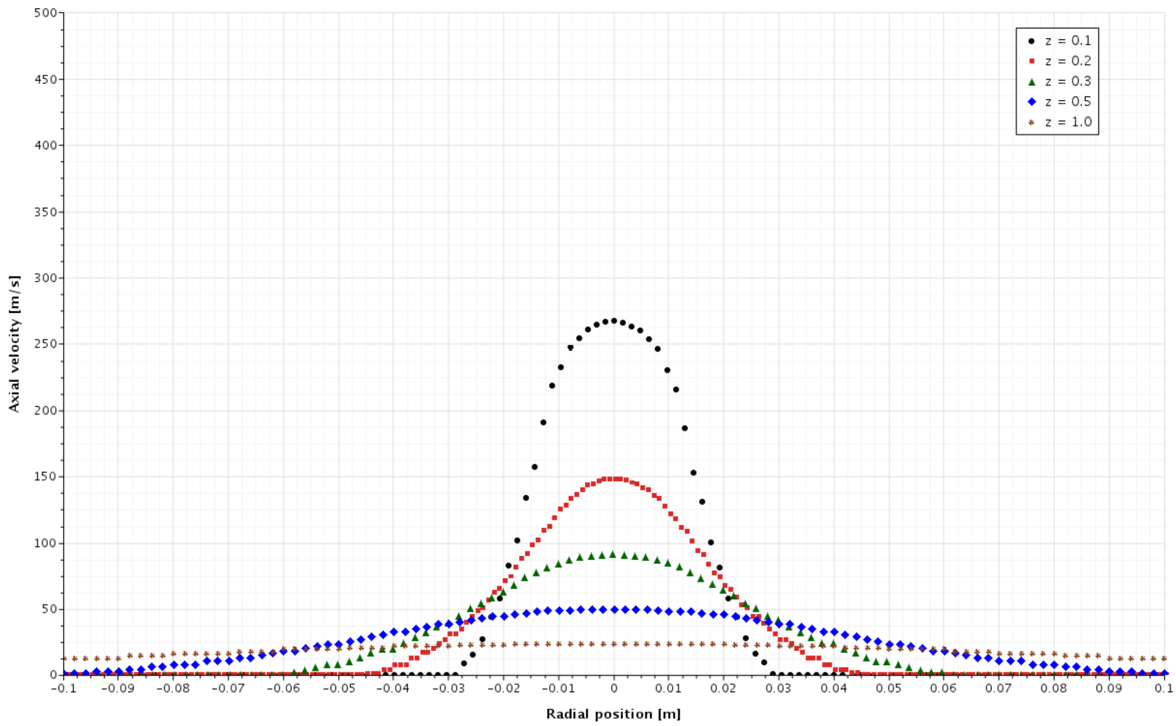

z = 0.1
z = 0.2
z = 0.3
z = 0.5
z = 1.0
Axial velocity [m/s]
Radial position [m]

(j)

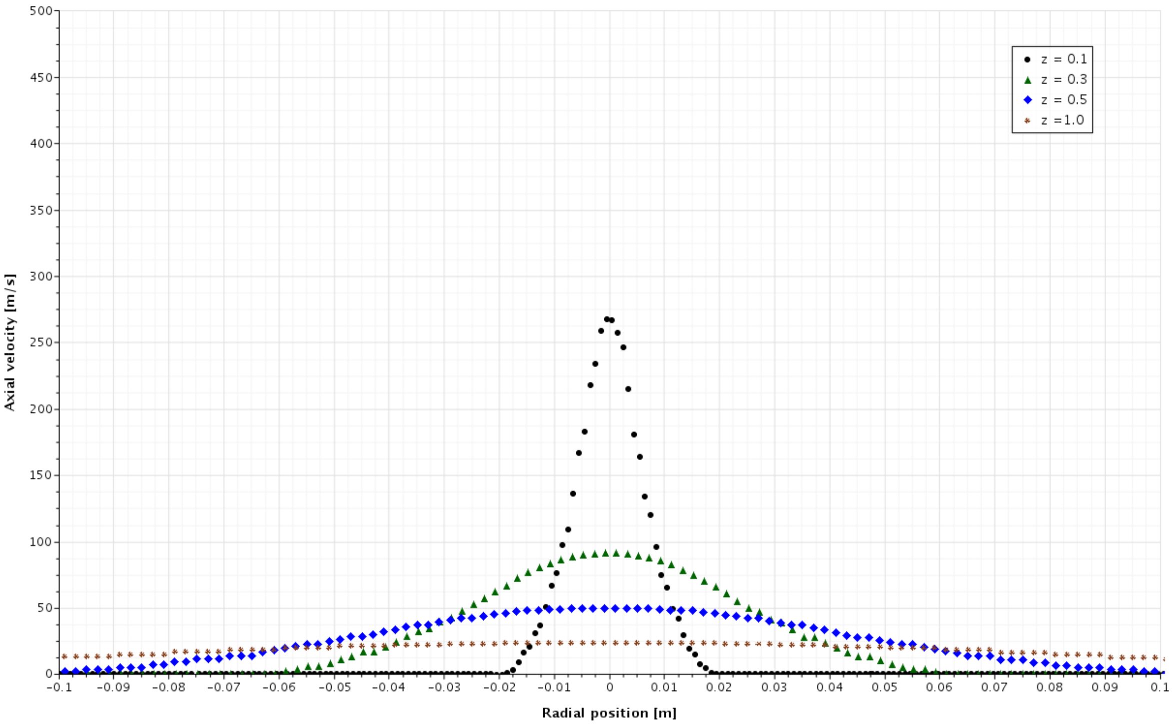
z = 0.1
z = 0.3
z = 0.5
z =1.0
Axial velocity [m/s]
Radial position [m]
500
450
400
350
300
250
200
150
100
50
0
−0.1
−0.09
−0.08
−0.07
−0.06
−0.05
−0.04
−0.03
−0.02
−0.01
0
0.01
0.02
0.03
0.04
0.05
0.06
0.07
0.08
0.09
0.1

(k)

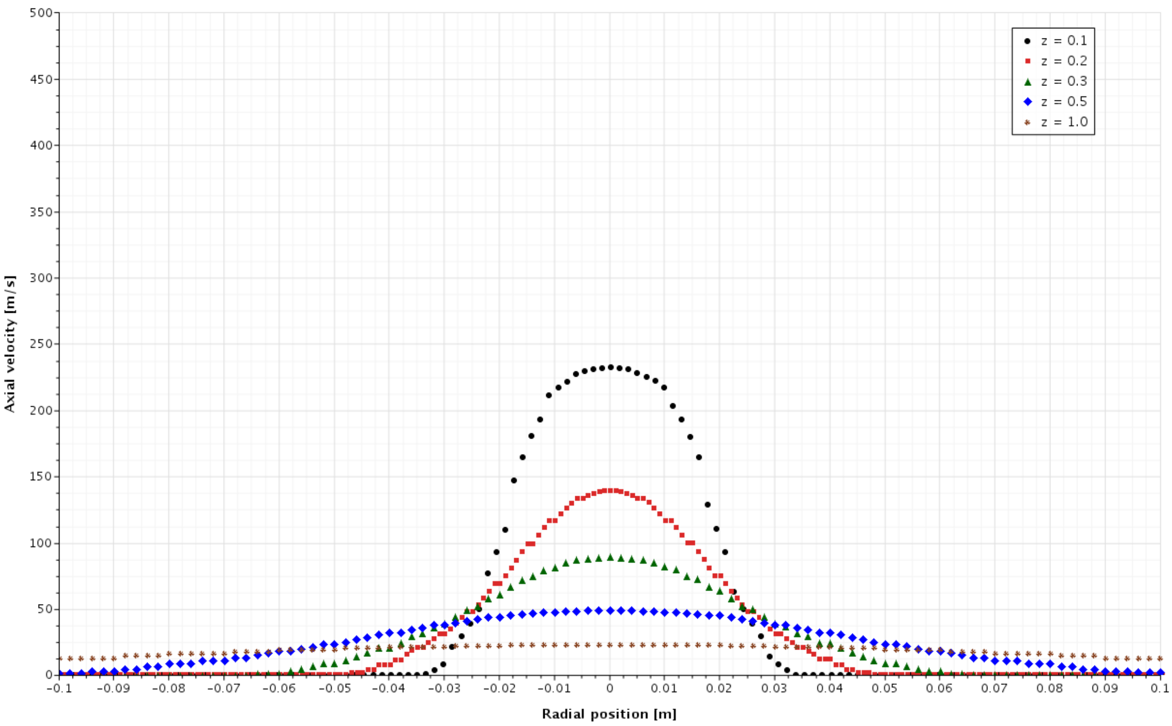
z = 0.1
z = 0.2
z = 0.3
z = 0.5
z = 1.0
Axial velocity [m/s]
Radial position [m]
500
450
400
350
300
250
200
150
100
50
0
−0.1
−0.09
−0.08
−0.07
−0.06
−0.05
−0.04
−0.03
−0.02
−0.01
0
0.01
0.02
0.03
0.04
0.05
0.06
0.07
0.08
0.09
0.1

(l)

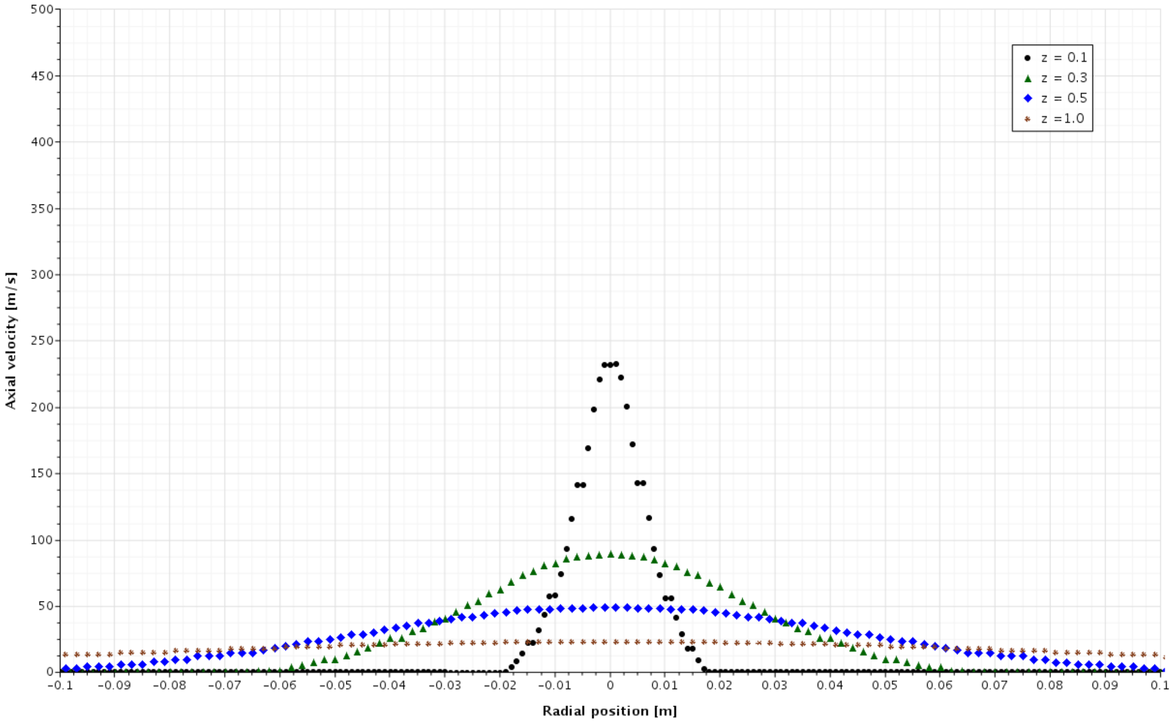

(m)

Figure A.-5: *Plots showing radial profiles of axial velocity for jets from a) a circular orifice and rectangular orifices with b) AR = 5 (major axis), c) AR = 5 (minor axis), d) AR = 10 (major axis) e) AR = 10 (minor axis), f) AR = 15: (major axis), g) AR = 15 (minor axis) in addition to from elliptical orifices with h) AR = 5 (major axis), i) AR = 5 (minor axis), j) AR = 10 (major axis), k) AR = 10 (minor axis), l) AR = 15 (major axis) and m) AR = 15 (minor axis).*